64 /2/ 2026

JOURNAL OF THEORETICAL AND APPLIED MECHANICS

WARSAW 2026, QUARTERLY, VOLUME 64, ISSN 1429-2955 eISSN 2543-6309

POLISH SOCIETY OF THEORETICAL AND APPLIED MECHANICS

ptmts

POLISH SOCIETY OF THEORETICAL AND APPLIED MECHANICS

JOURNAL OF THEORETICAL AND APPLIED MECHANICS

Vol. 64 • No. 2
Quarterly

WARSAW 2026

JOURNAL OF THEORETICAL AND APPLIED MECHANICS
(until 1997 Mechanika Teoretyczna i Stosowana, ISSN 0079-3701)

Beginning with Vol. 45, No. 1, 2007, *Journal of Theoretical and Applied Mechanics* (JTAM) has been selected for coverage in Thomson Reuters products and custom information services. Now it is indexed and abstracted in the following:

- **Science Citation Index Expanded** (also known as SciSearch®)
- **Journal Citation Reports/Science Edition**

Advisory Board

Editorial Board

Editorial Office

Al. Armii Ludowej 16, room 650; 00-637 Warsaw, Poland
e-mail: jtam@ptmts.org.pl
www.jtam.pl

JOURNAL OF THEORETICAL
AND APPLIED MECHANICS
64, 2, pp. 101–114, Warsaw 2026
https://doi.org/10.15632/jtam-pl/218270

RESEARCH ON THE PENETRATION RESISTANCE PERFORMANCE OF A CERAMIC BALL/NYLON ELASTOMER COMPOSITE STRUCTURE

Chaoming SHEN[1*], Shuming ZHAO[1], Kun TAN[2], Longqiang LI[1],
Fushan LI[3], Tingwei WANG[3]

[1] *School of Naval Architecture and Ocean Engineering, Jiangsu University of Science and Technology, Zhenjiang, China*
[2] *Nanjing Traffic Comprehensive Administrative Law Enforcement Corps, Nanjing, China*
[3] *China Special Equipment Inspection and Research Institute, Jiaxing, China*
*corresponding author, *shencm@just.edu.cn*

This paper proposes a ceramic ball/nylon elastomer composite structure. Experimental testing and finite element analysis were conducted to investigate the influence of key factors on the penetration resistance of the composite structures with constant total thickness. These factors include ceramic ball diameter, arrangement pattern, projectile head configuration, and the ratio of projectile diameter to ceramic ball diameter. The results indicate that the composite structures with three configurations exhibit higher resistance to round-nose projectiles compared to flat-nose projectiles. For projectiles with a diameter of 8.08 mm (both round-nose and flat-nose), the composite structures with two-different-diameters ceramic balls exhibit better penetration resistance compared to those with single-diameter or triple-different-diameters ceramic balls. Furthermore, when the diameter ratio of the projectile to the front-layer ceramic balls falls within 0.73–1.01, the penetration resistance performance of the composite structure is relatively better, and optimal penetration resistance is achieved when the diameter ratio between the front-layer ceramic balls and other back-layer ceramic balls is 1.7–2.0. These findings provide valuable references for designing penetration-resistant protective structures for ships and other marine constructions.

Keywords: ceramic ball; composite structure; penetration resistance performance; residual velocity.

1. Introduction

In recent decades, maritime transportation has become one of the most important modes of global trade and energy supply. Naval and commercial vessels operating in high-risk environments may be exposed to ballistic impacts and explosive fragmentation, posing significant threats to personnel and onboard high-value equipment. Therefore, improving the penetration resistance of ship structures is essential for enhancing operational safety and survivability. Ceramic materials have been widely investigated for protective applications due to their high strength, high hardness, and light weight.

Research on ceramic composite protective structures dates back to the late 20th century. Early studies of Woodward (1990) revealed that upon projectile impact, a protective ceramic cone forms, which helps reduce the shock on the backing plate. Subsequently, Zaera *et al.* (2000) further clarified this mechanism, finding that thicker ceramic plates result in smaller cones and lower stress on the backing plate. Lee and Yoo (2001) discovered that for a fixed areal density, an optimal ceramic-to-metal thickness ratio existed that maximized penetration resistance. More recently, Cao *et al.* (2020) highlighted the significant influence of boundary constraints on ceramic performance, considering crack initiation and wear. In addition, Tan *et al.* (2021) found that protective performance was optimized when the ceramic ball to projectile diameter ratio fell within a specific range. Feng and Zhu (2024) proposed a novel bionic composite with a rigid-flexible coupling structure, where soft and hard layers worked synergistically to dissipate impact energy through a progressive damage process.

In numerical analysis of penetration processes, Schwer and Day (1991) enhanced simulation accuracy by improving constitutive equations and optimizing meshes for armor-piercing projectiles and earth penetrators. Beissel and Johnson (2000) introduced the concept of an attrition surface to analyze real-time projectile damage and adjusted parameters to better simulate the penetration process. Fawaz *et al.* (2004) investigated the effect of incidence angles on ceramic–metal structures, finding that while kinetic energy remained similar, interlayer forces increased during full penetration. Feli and Asgari (2011) observed that ceramic cone angles increased with projectile velocity. Andraskar *et al.* (2023) concluded that the B4C ceramic plate had the best penetration resistance at a thickness of 7.5 mm. Aktaş and Çevik (2025) designed novel geometries of alumina ceramics, overcoming brittleness through spherical and triangular prism geometries. Additionally, Tan *et al.* (2023) developed a three-layer ceramic armor model, showing that layer sequence had little effect on ceramic damage compared to thickness. Existing research results show that the protective properties of ceramic composite structures are determined by the combination of material compatibility, geometric configuration and impact parameters: when impacted, the ceramic layer dissipates the kinetic energy of the projectile through crushing, while the backplate absorbs the remaining kinetic energy through deformation. Despite these advances, the multi-field coupling mechanisms governing energy transfer and failure evolution in complex protective structures remain insufficiently understood.

On the basis of the existing research, this paper proposes a ceramic ball/nylon elastomer composite protective structure, and through experiments and numerical simulations reveals the influence of structural parameters on its anti-elasticity performance, which can provide new ideas and references for the design of anti-penetration structures of marine vessels.

2. Numerical simulation methods

2.1. Establishment of numerical model

To investigate the influence of ceramic ball diameter and configuration on the penetration resistance of ceramic ball/nylon elastomer composite structures, numerical models of single-diameter, double-diameter and triple-diameter ceramic ball combination protection structures were developed, as shown in Fig. 1 and Fig. 2. The target plate has overall dimensions of 200 mm × 200 mm × 50 mm, with a 0.5 mm-thick steel plate on both its front and rear surfaces to form a sandwich structure. All target plates maintain a thickness of 50 mm, with internal ceramic balls arranged alternately in rows and columns, as shown in Fig. 1. In the triple-diameter configuration, the layers of large, medium, and small balls each constitute $1/3$ of the total thickness. In the double-diameter configuration, the large-diameter ceramic ball layer constitutes $3/5$ of the total thickness, while the small-diameter layer constitutes $2/5$, as shown in Fig. 2. The ceramic balls were homogeneously distributed in the single-diameter ceramic ball combination structure (Fig. 2). The three configurations were categorized into three major types based on ceramic ball diameter combinations. Specific dimensions of the protective structures and ceramic ball diameters are summarized in Table 1.

Owing to the geometric symmetry of the target plate of the ceramic ball/nylon elastomer composite, a $1/2$ model was adopted to better observe the response of the projectile penetrating through the protective structure and to improve the computational efficiency. In the ANSYS/LS-DYNA finite element software, SOLID168 solid elements were used for modeling, and the model was meshed with hexahedral elements. The interlayer interfaces (steel-nylon, ceramic-nylon) were simulated using the *CONTACT_AUTOMATIC_SURFACE_TO_ SURFACE_TIEBREAK

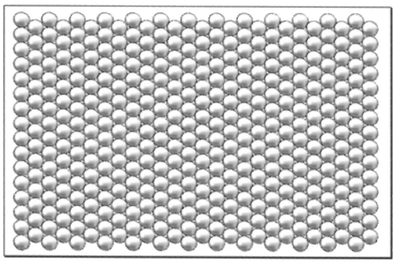

Fig. 1. Ceramic ball single-layer layout.

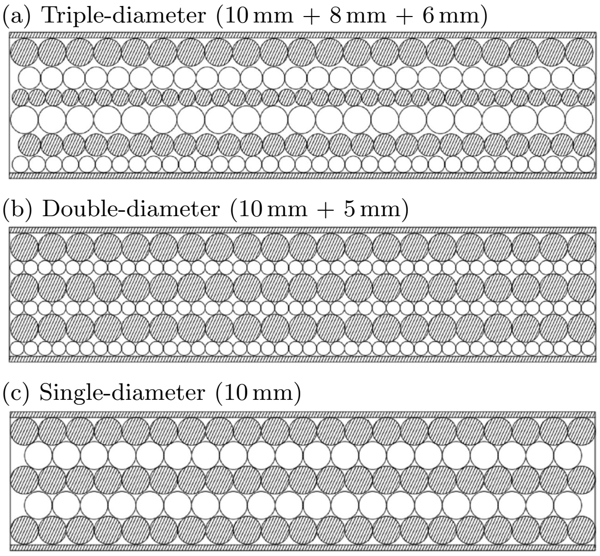

(a) Triple-diameter (10 mm + 8 mm + 6 mm)

(b) Double-diameter (10 mm + 5 mm)

(c) Single-diameter (10 mm)

Fig. 2. Sectional view of ceramic ball/nylon elastomer composite structure.

Table 1. Ceramic ball diameter and arrangement in protective panels.

Target number	Single-diameter	Target number	Double-diameter		Target number	Triple-diameter		
	Ball diameter [mm]		Ball 1 diameter [mm]	Ball 2 diameter [mm]		Ball 1 diameter [mm]	Ball 2 diameter [mm]	Ball 3 diameter [mm]
S1	5	D1	5	2.5	T1	8	6	4
S2	6	D2	6	3	T2	9	7	5
S3	7	D3	7	3.5	T3	10	8	6
S4	8	D4	8	4	T4	11	9	7
S5	9	D5	9	4.5	T5	12	10	8
S6	10	D6	10	5	T6	13	11	9
S7	11	D7	11	5.5	T7	14	12	10
S8	12	D8	12	6	T8	15	13	11
S9	13	D9	13	6.5	T9	16	14	12
S10	14	D10	14	7				
S11	15	D11	15	7.5				
S12	16	D12	16	8				

contact algorithm to characterize the interfacial bond failure behavior. In the penetration simulations, both round-nose and flat-nose projectiles were used (diameter: 8.08 mm, mass: 8 g). The round-nose projectiles had a length of 21.34 mm, while the flat-nose projectiles had a length of 20 mm. The projectile model is shown in Fig. 3, and the target plate model is shown in Fig. 4.

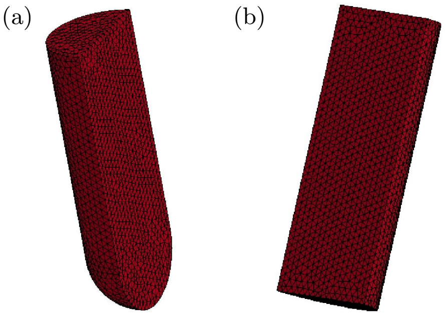

Fig. 3. Numerical model of a half-projectile: (a) round-nose bullet; (b) flat-nose bullet.

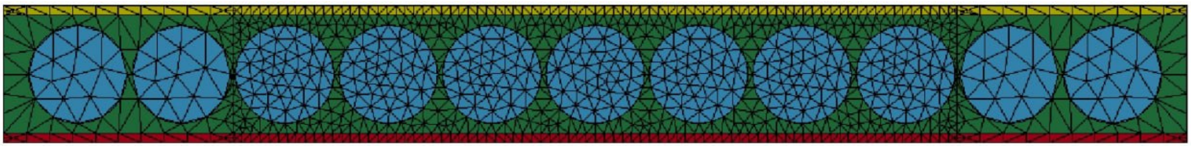

Fig. 4. Example of the target plate model for protective structure (single-layer structure).

2.2. Material constitutive model and parameters

The material of the projectile body (round-nose and flat-nose) is tool steel; Q235 steel is used for the front and back steel plates of the protective structure, and the Johnson–Cook constitutive model was adopted for the numerical simulations of these two materials, as shown:

$$\sigma_y = \left(A + B\bar{\varepsilon}_p^n\right)\left(1 + c\ln\bar{\varepsilon}^*\right)\left[1 - \left(\frac{T - T_r}{T_m - T_r}\right)^m\right]. \tag{2.1}$$

The model can describe the large deformation and high strain rate characteristics of metal materials, with the relevant parameters listed in Table 2 and Table 3.

Table 2. Johnson–Cook constitutive model parameters of the projectile body.

ρ [kg · m^{-3}]	G [MPa]	T_r [K]	T_m [K]	A [MPa]	B [MPa]	n	C	m	$\dot{\varepsilon}_0$	d_1	d_2
7830	770	293	1795	792.0	510.0	0.26	0.0640	1.03	0.1×10^{-5}	0	0.4

Table 3. Johnson–Cook constitutive model parameters for Q235 steel.

ρ [kg · m^{-3}]	G [MPa]	T_r [K]	T_m [K]	A [MPa]	B [MPa]	n	C	m	$\dot{\varepsilon}_0$	d_1	d_2
7800	798	293	1795	240.0	230.2	0.578	0.0652	0.706	2.1×10^{-3}	−0.0193	3.811

The material grade of the nylon elastomer is polyamide-6, and its constitutive relationship is described by the Cowper–Symonds model with the equation:

$$\sigma_Y = \left[1 + \left(\frac{\dot{\varepsilon}}{C}\right)^{1/P}\right]\left(\sigma_0 + \beta E_p \varepsilon_p^{\mathrm{eff}}\right), \tag{2.2}$$

where σ_0 is the initial yield stress, $\dot{\varepsilon}$ is the strain rate, C and P are the strain rate parameters, $\varepsilon_p^{\mathrm{eff}}$ is the effective plastic strain, and E_p is the plastic hardening modulus. The relevant material parameters of the nylon elastomer are shown in Table 4.

The ceramic ball is made of Al_2O_3, and the JOHNSON_HOLMQUIST_CERAMICS model, also known as the JH model, is selected for numerical simulation. The damage model consisting of strength and cumulative damage failure is particularly suitable for describing the damage mode of brittle materials such as ceramics and glass.

Table 4. Parameters of the Cowper–Symonds constitutive model for nylon elastomer.

Material	ρ $[\mathrm{kg}^{-3}]$	Elastic modulus [GPa]	P	C	Poisson's ratio	$R_{P0.2}$ [Mpa]	Shear modulus [GPa]	Fracture strain
PA6	1140	3.3	0.574	1285.3	0.41	60	1.275	0.6

The equivalent stress for ceramic materials is expressed as:

$$\sigma^* = \sigma_i^* - D\left(\sigma_i^* - \sigma_f^*\right), \tag{2.3}$$

$$\sigma_i^* = a\left(p^* + t^*\right)^n\left(1 + c\ln\dot{\varepsilon}^*\right), \tag{2.4}$$

$$\sigma_f^* = b\left(p^*\right)^m\left(1 + c\ln\dot{\varepsilon}^*\right) \leq \mathrm{SFMAX}, \tag{2.5}$$

where "*" indicates that the parameter is a dimensionless parameter, the stress is normalized by the Hugoniot elastic limit (HEL) stress. σ_i^* represents the dimensionless equivalent stress when the material is intact, σ_f^* represents the dimensionless equivalent stress when the material is damaged. D represents the damage factor of ceramic, which ranges from 0 to 1; $D = 0$ corresponds to the intact state, and $D = 1$ represents complete material failure. The pressure is normalized by the hydrostatic pressure p_{HEL} at the HEL, $p^* = p/p_{\mathrm{HEL}}$ denotes the dimensionless pressure, t^* denotes the maximum tensile hydrostatic pressure that the material can withstand, $\dot{\varepsilon}^*$ represents the dimensionless strain rate; a, c, n, b, m denote material constants. The specific material parameters are shown in Table 5.

Table 5. JH constitutive model parameters of ceramic balls.

G [GPa]	ρ $[\mathrm{g\cdot cm^{-3}}]$	σ_{HEL} [GPa]	a	n	c	b	m	$\dot{\varepsilon}_0$
90.16	3.7	6.7	0.88	0.64	0.003	0.28	0.6	1×10^{-6}
PHEL [GPa]	BULK	k_1	k_2	k_3	d_1	d_2	SFMAX	
3.63	1	130.95	0	0	0.005	0.7	1.6	

Equation (2.6) defines the damage as the accumulated ratio of incremental plastic strain to the corresponding critical fracture strain at each step, which can reflect the evolution process of the initiation and gradual propagation of microcracks and microdefects inside the material with plastic deformation. The ceramic damage factor is expressed by:

$$D = \sum\frac{\Delta\varepsilon^p}{\varepsilon_f^p} = \sum\frac{\Delta\varepsilon^p}{d_1\left(p^* + f_t^*\right)^{d_2}}, \tag{2.6}$$

where $\Delta\varepsilon^p$ is the increase in plastic strain at each incremental step, ε_f^p is the plastic fracture strain, and d_1, d_2 are damage constants.

The ceramic ball is not fully damaged; its material equation of state is expressed by:

$$p = k_1\mu + k_2\mu^2 + k_3\mu^3, \tag{2.7}$$

where k_1, k_2, k_3 are constants, $u = \frac{p}{p_0} - 1$, ρ_0 is the initial density, and ρ is the present density.

2.3. Experimental validation of the numerical simulation method for penetration

To validate the numerical simulation methodology, an experiment consistent with the numerical simulation model was conducted, and the numerical simulation results were compared with real ballistic test data. Specifically, the experiment was performed using a standard single-stage light gas gun. First, 8.08 mm-diameter round-nose or flat-nose projectiles were mounted in a sabot, and loaded into the gun barrel. High-pressure gas accelerates the sabot and embedded projectile, which then penetrates the target plate after passing through the sabot separator, as shown in Fig. 5.

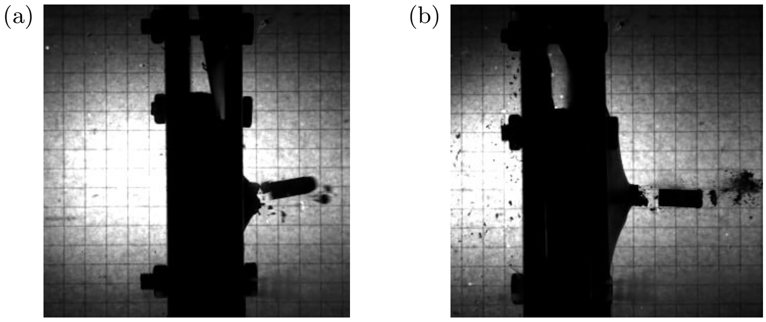

Fig. 5. Penetration of the projectile into the ceramic composite target plate: (a) round-nose bullet; (b) flat-nose bullet.

The protective structure was bolted to the target chamber, with front and rear steel plates each having dimensions of 200 mm × 200 mm × 0.5 mm. The central nylon-ceramic ball composite layer had a cross-sectional size of 130 mm × 130 mm. Three sets of test specimens were prepared for the target plate: a single layer of 5 mm diameter ceramic balls, a single layer of 10 mm diameter ceramic balls, and a double layer (5 mm + 10 mm diameter ceramic balls), as shown in Fig. 6. Detailed parameters of the target plate are provided in Table 6.

(a) A layer of 5 mm diameter ceramic ball protective structure

(b) A layer of 10 mm diameter ceramic ball protective structure

(c) Two layers (10 mm + 5 mm) diameter ceramic ball protective structure

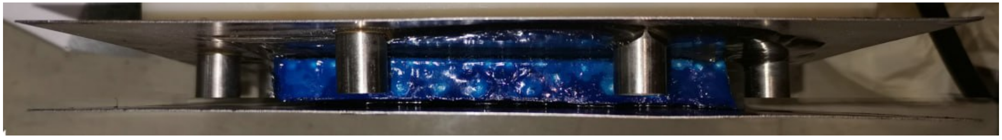

Fig. 6. Three prepared ceramic ball/nylon elastomer composite protective structures.

Table 6. Parameters of ceramic ball/nylon elastic composite structure target plate.

Bullet category	Target plate number	Target board size [mm]	Ceramic ball layers	Ceramic ball diameter [mm]
Round-nose bullet	SDY	200 × 200	1	5
	DDY		1	10
	SY		2	First floor: 5, second floor: 10
Flat-nose bullet	SDP	200 × 200	1	5
	DDP		1	10
	SP		2	First floor: 5, second floor: 10

As shown in Table 7, the relative errors between the experimental and numerical simulation data are generally within 10 % in the residual velocity under identical test conditions, with a few outliers (e.g., DDP-1, DDP-2), indicating that the numerical simulation has good reliability. The relative errors between the numerical simulation data and the experimental data are in the range of 12 % to 18 %, which is within acceptable limits.

Table 7. Comparison of experimental and simulation data for the ceramic ball protection structure.

Target number	Experimental data			Simulation data		Residual velocity error [%]	Deviation angle error [%]
	Initial speed [m/s]	Residual velocity [m/s]	Bullet deflection [°]	Residual velocity [m/s]	Bullet deflection [°]		
SDY-1	306.37	104.91	14.69	115.16	17.41	9.77	18.52
SDY-2	299.15	123.16	8.8	110.05	10.10	10.64	14.77
SDP-1	289.35	158.73	2.3	176.54	2.69	11.22	16.96
SDP-2	287.46	162.46	4.96	175.31	5.57	7.91	12.30
DDY-1	291.35	5.91	11.45	6.51	13.51	10.15	17.99
DDY-2	295.03	21.08	11.84	7.64	13.72	63.76	15.88
DDP-1	273.14	No breakdown	/	16.55	10.14	/	/
DDP-2	278.81	No breakdown	/	18.03	9.35	/	/
SY-1	288.27	No breakdown	/	No breakdown	/	/	/
SY-2	293.14	No breakdown	/	No breakdown	/	/	/
SP-1	304.48	No breakdown	/	No breakdown	/	/	/
SP-2	295.03	No breakdown	/	No breakdown	/	/	/

Good agreement between experimental and numerical results was observed for most specimen groups, except for DDP-1 and DDP-2. In these cases, the numerical simulation predicted complete penetration (residual velocity $> 0\,\mathrm{m/s}$), whereas no penetration was observed in the experiment (residual velocity $= 0\,\mathrm{m/s}$). This discrepancy can be attributed to the uncertainties in the experiments, including differences in homogeneity and compactness of the ceramic spheres encapsulated in the nylon matrix, as well as the deviation in the actual position of the projectile's impact point. These factors lead to the fluctuation of the experimental results. However, the overall numerical simulation errors for the residual velocity and the projectile's deflection angle remain within a reasonable range.

Figure 7 shows the rupture morphology of round-nose and flat-nose projectiles following penetration of the ceramic composite protective structure, under both numerical simulation and experimental conditions. Moreover, the breach morphologies from the simulation and the experiment are in close agreement. Regardless of the projectile shape, the breach exhibits a petal-like shape; notably, the breach formed by the flat-nose projectile is larger than that formed by the round-nose projectile.

For the SY-1, SY-2, SP-1, and SP-2 ceramic composite protective structures – which remained unpenetrated in experiments – the numerical simulations also consistently showed no penetration. As shown in Fig. 8, both simulation and experimental results exhibit pronounced bulging deformation on the rear surface of the protective structure. The deformation modes and bulge dimensions are in close agreement, with a bulge deformation of approximately 8 mm observed in both cases.

In summary, the validity of the material model parameters and ANSYS/LS-DYNA finite element model setup was verified by comparing the numerical simulation results of the penetration process with the experimental results, demonstrating the accuracy of the established numerical simulation method.

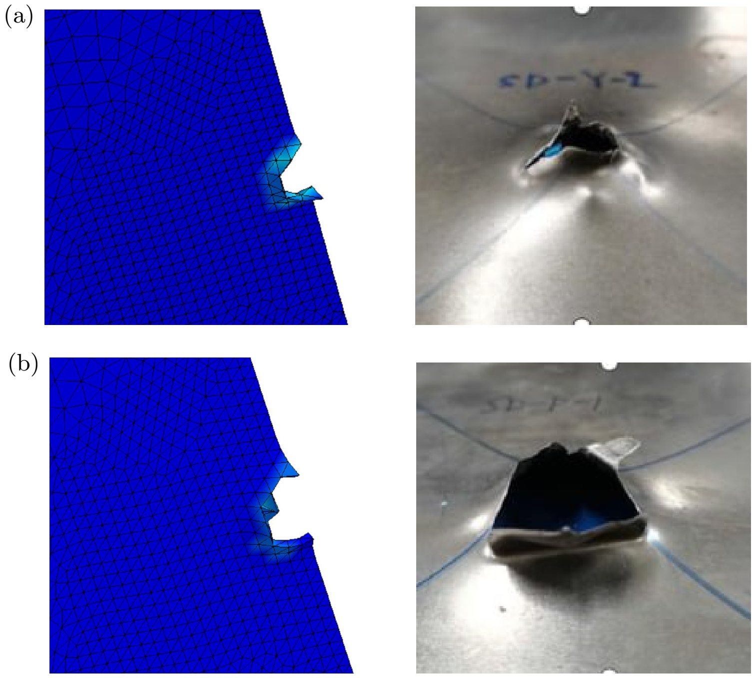

Fig. 7. Comparison between simulated and experimental results for the breach of the protective structure: (a) round-nose bullet; (b) flat-nose bullet.

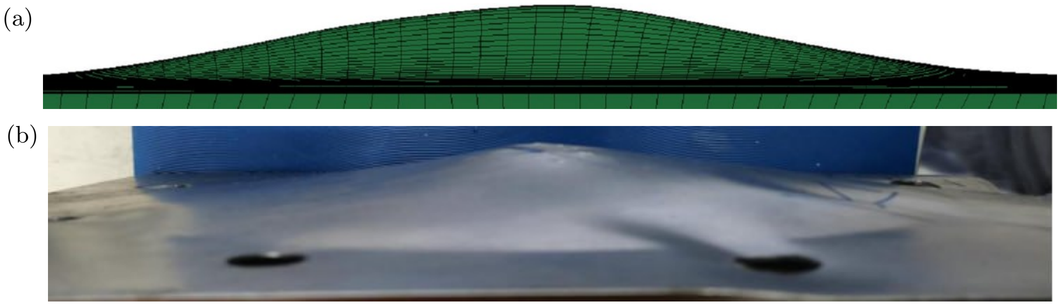

Fig. 8. Comparison between simulated and experimental results for the protrusion of the structure: (a) simulation diagram; (b) experimental diagram.

3. Influence of ceramic ball diameter combinations on the penetration resistance of protective structures

3.1. Comparison and analysis of the penetration resistance of ceramic ball protective structures with different ceramic ball diameter combinations

To more directly and clearly understand the residual velocities of various ceramic composite protective structures under projectile penetration, the residual velocities of round-nose and flat-nose projectiles at an impact velocity of 600 m/s are plotted in line charts. For simplicity and clarity of the charts, the x-axis is labeled with the diameter of the first row of ceramic balls behind the impact face of the protective structure, as shown in Fig. 9 and Fig. 10.

As shown in the figures, the residual velocities of all protective structures against both bullets exhibit a V-shaped pattern of decreasing and then increasing under an initial impact velocity of 600 m/s. However, the bottom of the V-shaped curve for the double-diameter ceramic ball protective structure is flatter and the velocity change is more gradual. Furthermore, among the three types of composite protective structures, when the diameter of the first layer of ceramic balls is the same, the residual velocity of the projectile for the double-diameter composite protective structure is lower.

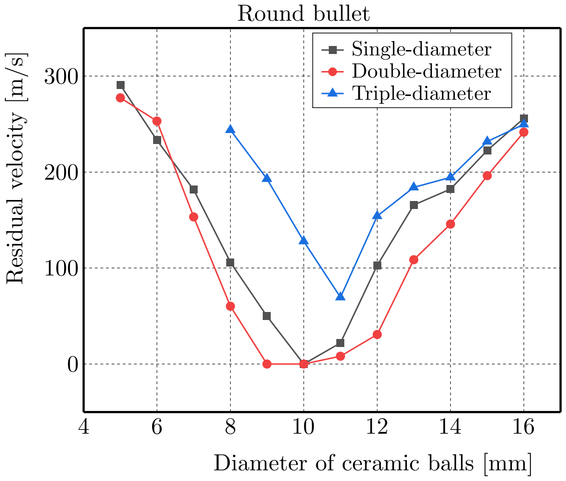

Fig. 9. Residual velocity of protective structure under the impact of round-nose projectile.

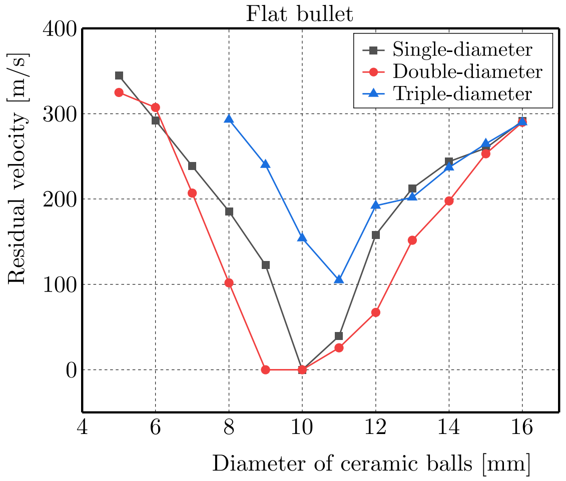

Fig. 10. Residual velocity of the protective structure under the impact of a flat-nose projectile.

Among them, two sets of zero residual velocities were observed for the double-diameter ceramic ball protective structure for both projectile shapes, one set was observed for the single-diameter structure, and none of the zero values were observed for the triple-diameter structure. Overall, the average residual velocity of the double-diameter structure is 33.4 m/s lower than that of the single-diameter structure, while the residual velocity of the triple-diameter structure is 97.1 m/s higher than that of the double-diameter structure. These results indicate that the three structures are ranked by penetration resistance as follows: double-diameter ceramic ball protective structure > single-diameter ceramic ball protective structure > triple-diameter ceramic ball protective structure.

Under penetration by both round-nose and flat-nose projectiles, the double-diameter ceramic ball composite protective structure exhibits significantly superior penetration resistance compared to the triple-diameter and single-diameter ceramic ball composite structures. This advantage can be attributed to two mechanisms: (1) the relatively larger ceramic balls in the double-diameter structure effectively degrade the projectile's kinetic energy by consuming it, abrading the projectile's surface, and inducing yaw; (2) as the impact force is transmitted from the frontal ceramic balls to the internal structure, the region composed of smaller ceramic balls and the nylon matrix rapidly distributes the load, thereby activating more ceramic balls and the matrix material in a collective resistance against penetration.

In contrast, the single-diameter ceramic ball composite structure engages a relatively limited number of ceramic balls and nylon matrix during impact. For the triple-diameter ceramic ball composite structure, the proportion of nylon matrix dedicated to dissipating the projectile's kinetic energy is insufficient during penetration.

The double-diameter structure, however, achieves an optimal balance between energy dissipation and collaborative protection by rationally matching the proportions of ceramic balls to the nylon matrix, thereby producing the optimal protective effect.

3.2. Effect of ceramic ball diameter on the penetration resistance of the protective structure

A comparison of the data in Fig. 11 to Fig. 13 indicates that, for all three types of composite protective structures, the residual velocity of the round-nose projectile is lower than that of the flat-nose projectile. This indicates that these three types of structures provide better protective effectiveness against round-nose projectiles.

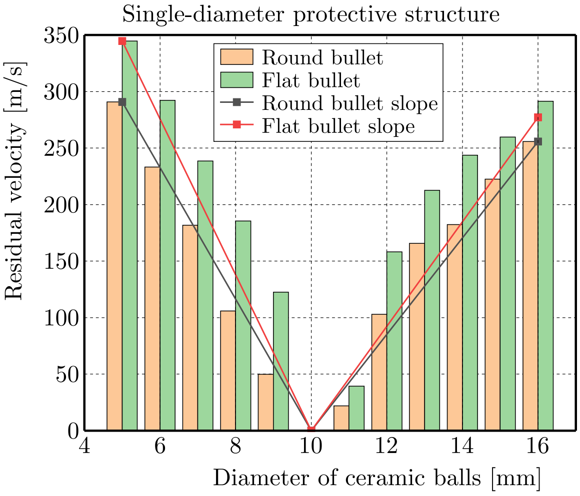

Fig. 11. Projectile residual velocity diagram for single-diameter ceramic ball composite structure.

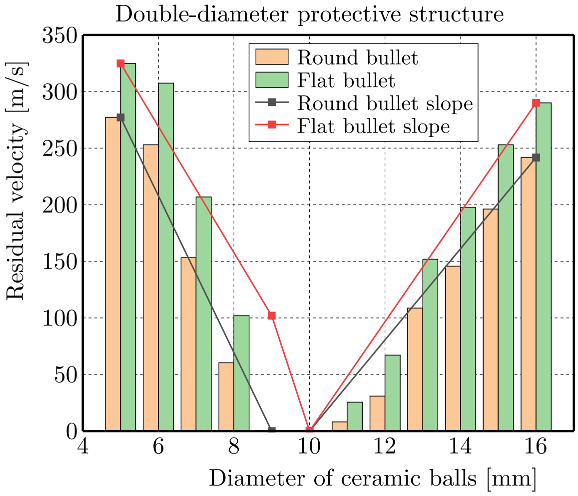

Fig. 12. Projectile residual velocity diagram for double-diameter ceramic ball composite structure.

For the single- and double-diameter ceramic ball structures: when the diameter of the front-row ceramic balls ranges from 8 mm to 11 mm, the structures generally exhibit superior penetration resistance. If the diameter is less than 8 mm or greater than 11 mm, the penetration resistance decreases significantly. Notably, when the maximum diameter of the ceramic balls is approximately 10 mm, the projectile's residual velocity drops to 0 m/s (i.e., the structure is not penetrated), achieving the optimal protective effect. For the triple-diameter ceramic ball

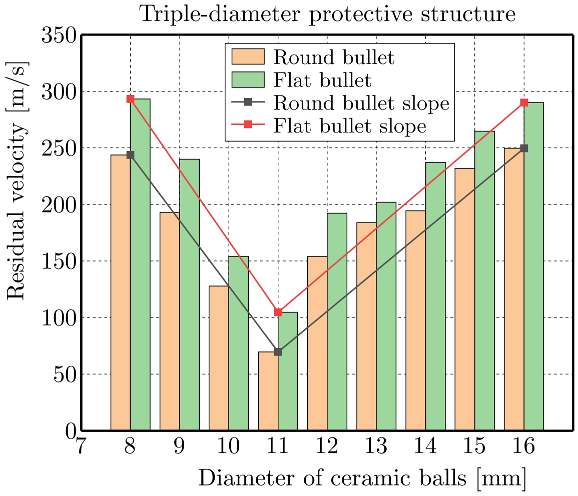

Fig. 13. Projectile residual velocity diagram for triple-diameter ceramic ball composite structure.

composite: the structure remains unpenetrated (residual velocity = 0 m/s) under all tested conditions. When the ceramic ball diameter is 11 mm, the structure exhibits the lowest residual velocity (though still non-zero).

Using the ceramic ball diameter corresponding to the minimum residual velocity (i.e., the critical diameter) as a reference, the slope of the ceramic ball diameter-residual velocity curve indicates that: below the critical diameter, the residual velocity decreases as the ball diameter increases (negative slope). Above the critical diameter, the residual velocity increases as the ball diameter increases (positive slope).

For all three configurations, the absolute value of the curve slope in the region above the critical diameter is smaller than that in the region below it, indicating that increasing ceramic ball diameter has a more gradual effect on residual velocity when the diameter is larger than the critical value.

Further analysis of the double-diameter structure, which exhibits optimal performance, shows that superior penetration resistance is generally achieved when the ceramic ball diameter exceeds that of the projectile. However, if the ceramic ball diameter is much larger than the projectile diameter, the protective performance declines markedly. The optimal performance occurs when the ratio of the projectile diameter to the ceramic ball diameter falls within the range of 0.73 to 1.01 (corresponding to a ceramic ball diameter range of approximately 8 mm to 11 mm).

4. Effect of two ceramic ball diameters and their double-diameter ratio on the penetration resistance of double-diameter ceramic ball composite protective structures

4.1. Selection of ceramic ball proportion and diameter

A double-diameter ceramic ball composite protective structure with superior penetration resistance was selected for in-depth study. Given that this double-diameter ceramic ball composite protective structure exhibits optimal penetration resistance when the diameter of the front-row ceramic balls ranges from 8 mm to 11 mm, the diameters of the front-row ceramic balls in the numerical model of this section are set to 7 mm, 8 mm, 9 mm, 10 mm, 11 mm, and 12 mm. The diameter ratio of the front-row ceramic balls relative to the rear-row ceramic balls ranges from 0.8 to 3.5.

The protective structures are divided into 6 groups based on the diameter of the front-row ceramic balls. Within each group, the diameter of the rear-row ceramic balls is further subdivided based on the diameter ratio (η) relative to that of the front-row ceramic balls. The structures are composed of intact ceramic balls, with the total thickness controlled at approximately 50 mm. Specifically: the thickness of the front-row ceramic ball region makes up about 2/3 of the total thickness, while the rear-row ceramic ball region accounts for about 1/3 of the total thickness. The specific dimensional parameters of the ceramic balls for each group are detailed in Table 8.

Table 8. Parameters of various ceramic ball composite protection structures.

Front row ball	Diameter of the ball at the back										Unit
7 mm diameter	8.8	6.4	5.0	4.1	3.5	3.0	2.7	2.4	2.2	2.0	mm
8 mm diameter	10	7.3	5.7	4.7	4.0	3.5	3.1	2.8	2.5	2.3	mm
9 mm diameter	11.3	8.2	6.4	5.3	4.5	3.9	3.5	3.1	2.8	2.6	mm
10 mm diameter	12.5	9.1	7.1	5.9	5.0	4.3	3.8	3.4	3.1	2.9	mm
11 mm diameter	13.8	10	7.9	6.5	5.5	4.8	4.2	3.8	3.4	3.1	mm
12 mm diameter	15	10.9	8.6	7.1	6.0	5.2	4.6	4.1	3.9	3.4	mm
Ball diameter ratio	0.8	1.1	1.4	1.7	2.0	2.3	2.6	2.9	3.2	3.5	η

4.2. Analysis of the effect of ceramic ball diameter and ceramic ball diameter ratio on the projectile's residual velocity

Round-nose and flat-nose projectiles penetrated the ceramic ball composite protective structures at an impact velocity of 600 m/s. The residual velocities of the projectiles after penetrating the double-diameter ceramic ball structures with different diameter ratios were obtained, as shown in Fig. 14.

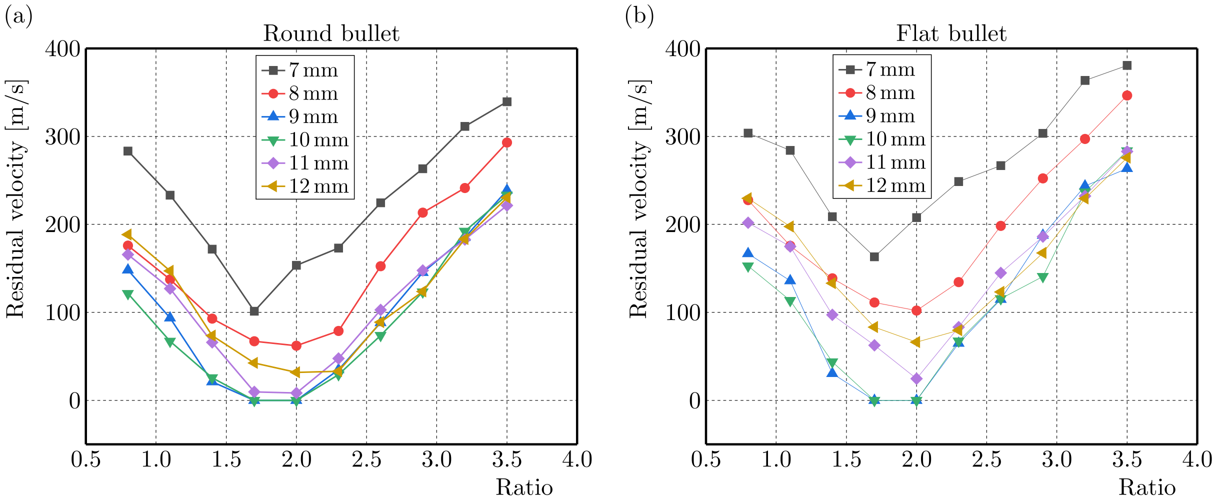

Fig. 14. Residual velocity of the ceramic ball protective structure for the same projectile: (a) round-nose bullet; (b) flat-nose bullet.

Figure 14 indicates that when the round-nose and flat-nose projectiles penetrate the ceramic ball protective structure with different ceramic ball diameter ratios, the residual velocities of both round-nose and flat-nose projectiles exhibit a V-shaped trend, characterized by an initial decrease followed by an increase. However, the bottom of the V-shaped curve for the round-nose projectiles is flatter, indicating a more gradual velocity transition. The data reveal that the residual velocity of the round-nose projectile is lower than that of the flat-nose projectile. This demonstrates that the double-diameter ceramic ball protective structure is more effective against round-nose projectiles, which is consistent with the previous conclusion.

The data indicate that residual velocity decreases gradually until reaching the optimal diameter ratio threshold (about 2.0), beyond which it rises steeply. For instance, when a round-nose projectile penetrates a protective structure fronted with 8 mm ceramic balls, the residual velocity rapidly increases as the ceramic ball diameter ratio rises to 2.6, reaching a level equivalent to that observed at a ratio of 0.8. This demonstrates that exceeding the optimal diameter ratio significantly degrades protective performance, leading to a sharp decline in anti-penetration capability.

The analyses indicate that, for both round-nose and flat-nose projectiles, the residual velocity of the projectiles exhibits a decreasing-then-increasing trend as the diameter of the front-row ceramic balls ranges from 7 mm to 12 mm. This confirms the significant influence of the ceramic ball diameter ratio on the penetration resistance of the composite protective structure.

Within the specific diameter ratio range of 1.7–2.0, the fluctuation in the residual velocity of round-nose projectiles narrows considerably (average fluctuation range: 32.9 m/s). This demonstrates that a ceramic ball size gradient (i.e., diameter ratio) within this range effectively optimizes the penetration resistance of the structure. For flat-nose projectiles, the magnitude of residual velocity change (52.7 m/s) over the same diameter ratio interval (1.7–2.0) is larger than for round-nose projectiles. Nevertheless, this change remains relatively small compared to the overall variation range, indicating that the ceramic ball composite protective structure maintains stable and effective penetration resistance within this specific diameter ratio range.

When the front-row ceramic balls have a diameter of 9 mm or 10 mm, the residual velocities of the projectiles across various diameter ratios are significantly lower. This indicates enhanced penetration resistance of the double-diameter ceramic ball composite protective structure. Notably, within the diameter ratio range of 1.7 to 2.0, the residual velocities of both round-nose and flat-nose projectiles drop to zero (i.e., the structure remains unpenetrated), thus yielding optimal protective effectiveness.

Based on the above analysis, the protective structure achieves optimal penetration resistance when the ceramic ball diameter ratio falls within the range of 1.7 to 2.0. On the one hand, if the ratio is too small, the rear-row ceramic balls become excessively large. This results in an insufficient number of rear-row ceramic balls participating in load transfer when the projectile's impact load propagates from front to rear, thereby compromising the structure's overall anti-penetration capacity. On the other hand, if the ratio is too large, the rear-row ceramic balls become excessively small. Although this increases the number of ceramic balls involved in load transfer, the inadequate compressive strength of smaller ceramic balls likewise fails to enhance the structure's penetration resistance.

5. Conclusion

This study designed ceramic ball/nylon elastomer composite structures with different ceramic ball diameters and arrangement modes, and conducted penetration tests on target plates with different structural forms using 8.08 mm round-nose/flat-nose projectiles. Combined with numerical simulations, the following main conclusions were obtained:

1) For both round-nose and flat-nose projectiles, the double-diameter ceramic ball protective structure outperforms the single-diameter and triple-diameter structures in penetration resistance. Additionally, all three types of protective structures (single-diameter, double-diameter, and triple-diameter) exhibit superior resistance to round-nose projectiles compared to flat-nose projectiles.
2) When 8.08 mm-diameter round-nose and flat-nose projectiles penetrate the double-diameter ceramic ball protective structure, penetration resistance improves with ceramic balls larger than the projectile diameter. However, protective efficacy deteriorates markedly when the ball diameter exceeds the projectile diameter by over 4 mm. Optimal anti-penetration performance occurs within the 0.73–1.01 projectile-to-ceramic-ball diameter ratio range for

the first-row ceramic balls immediately behind the strike-face, corresponding to strike-face ceramic ball diameters of 8 mm to 11 mm.

3) In the double-diameter ceramic ball protective structure, the residual velocity drops to zero when the front-to-rear ceramic ball diameter ratio is 1.7–2.0 (front-row ceramic ball diameter: 9 mm to 10 mm), resulting in complete protection (i.e., the structure remains unpenetrated).

References

1. Aktaş, L.T., & Çevik, M. (2025). Ballistic impact analysis of composite armors incorporating prismatic and spherical self-healing ceramic structures. *Mechanics of Composite Materials*, *61*(4), 739–752. https://doi.org/10.1007/s11029-025-10306-6
2. Andraskar, N., Tiwari, G., Goel, M.D., & Senthil, K. (2023). Numerical investigation of the effect of layering thickness on the ballistic response of ceramic/metal composite structure. *Mechanics of Solids*, *58*(4), 1351–1369. https://doi.org/10.3103/S002565442360071X
3. Beissel, S.R., & Johnson, G.R. (2000). An abrasion algorithm for projectile mass loss during penetration. *International Journal of Impact Engineering*, *24*(2), 103–116. https://doi.org/10.1016/S0734-743X(99)00146-3
4. Cao, J., Lai, J., Zhou, J., Kang, N., Du, L., & Miao, Y. (2020). Experiments and simulations of the ballistic response of ceramic composite armors. *Journal of Mechanical Science and Technology*, *34*(7), 2783–2793. https://doi.org/10.1007/s12206-020-0611-8
5. Fawaz, Z., Zheng, W., & Behdinan, K. (2004). Numerical simulation of normal and oblique ballistic impact on ceramic composite armours. *Composite Structures*, *63*(3–4), 387–395. https://doi.org/10.1016/S0263-8223(03)00187-9
6. Feli, S., & Asgari, M.R. (2011). Finite element simulation of ceramic/composite armor under ballistic impact. *Composites Part B: Engineering*, *42*(4), 771–780. https://doi.org/10.1016/j.compositesb.2011.01.024
7. Feng, X., & Zhu, P. (2024). Study of impact resistance of a novel bio-inspired ceramic-composite structure using finite element simulations. *Mechanics of Advanced Materials and Structures*, *31*(25), 7420–7433. https://doi.org/10.1080/15376494.2023.2245813
8. Lee, M., & Yoo, Y.H. (2001). Analysis of ceramic/metal armour systems. *International Journal of Impact Engineering*, *25*(9), 819–829. https://doi.org/10.1016/S0734-743X(01)00025-2
9. Schwer, L.E., & Day, J. (1991). Computational techniques for penetration of concrete and steel targets by oblique impact of deformable projectiles. *Nuclear Engineering and Design*, *125*(2), 215–238. https://doi.org/10.1016/0029-5493(91)90079-W
10. Tan, K., Shen, C., Chen, H., Wang, J., Cai, C., Zhang, H., & Liu, C. (2021). *Composite protection plate with non-equal-diameter ceramic balls* (Patent No. CN 212409494 U). https://patents.google.com/patent/CN212409494U/en?oq=CN+212409494+U+2011+
11. Tan, M., Zhang, X., Xiong, W., Liu, C., Han, G., & Li, Y. (2023). Influence of layered back plate on the ballistic performance of ceramic armor. *Composite Structures, 308*, Article 116688. https://doi.org/10.1016/j.compstruct.2023.116688
12. Woodward, R.L. (1990). A simple one-dimensional approach to modelling ceramic composite armour defeat. *International Journal of Impact Engineering*, *9*(4), 455–474. https://doi.org/10.1016/0734-743X(90)90035-T
13. Zaera, R., Sánchez-Sáez, S., Pérez-Castellanos, J.L., & Navarro, C. (2000). Modelling of the adhesive layer in mixed ceramic/metal armours subjected to impact. *Composites Part A: Applied Science and Manufacturing*, *31*(8), 823–833. https://doi.org/10.1016/S1359-835X(00)00027-0

Manuscript received October 28, 2025; accepted for publication February 18, 2026;
published online April 21, 2026.

JOURNAL OF THEORETICAL
AND APPLIED MECHANICS
64, 2, pp. 115–129, Warsaw 2026
https://doi.org/10.15632/jtam-pl/220006

NONLINEAR DAMPING IDENTIFICATION USING AN EXTENDED STABILIZED LAYERS METHOD

Nourhaine YOUSFI*, Rania MAKTOUF, Ali AKROUT, Lassaad WALHA,
Mohamed HADDAR

Mechanics, Modelling and Production Laboratory (LA2MP), National Engineering School of Sfax,
University of Sfax, Sfax, Tunisia

*corresponding author, *nourhainegem@gmail.com*

In many practical mechanical systems, the dynamic response is strongly influenced by time-varying stiffness, often coupled with nonlinear damping effects. Neglecting stiffness variability may lead to inaccurate predictions of vibration amplitudes and energy dissipation. This study is the first to extend and apply the stabilized layers method for nonlinear (SLMnl) damping identification to mechanical systems with time-varying stiffness. The SLMnl,kv is developed for multi-degree-of-freedom systems exhibiting nonlinear damping and time-varying stiffness. The effectiveness of the proposed method is demonstrated through its application to a spur gear pair system characterized by nonlinear damping and time-varying mesh stiffness.

Keywords: nonlinear damping identification; stabilized layers method; time-varying stiffness; system identification; sidebands.

1. Introduction

Several types of damping mechanisms can be found in mechanical systems (Qu *et al.* 2024), including viscous damping, Coulomb damping, and hysteretic damping (Liu *et al.*, 2022; Clough & Penzien, 1993). Damping identification plays a crucial role in dynamic system analysis, as accurate estimation of damping parameters is essential for design and analysis (Paz, 1991). Conventional damping identification techniques often suffer from several drawbacks, such as high computational cost and strong sensitivity to measurement noise (Zahid *et al.*, 2020). Considerable efforts have therefore been dedicated to overcoming these limitations. Among them, the stabilized layers method (SLM), introduced by Lisitano *et al.* (2018), has demonstrated good robustness and reliability by providing damping coefficients with clear physical interpretation. Nevertheless, the formulation proposed by Bonisoli *et al.* (2019) remains restricted to equivalent linear representations. In real engineering applications, numerous mechanical systems exhibit nonlinear damping phenomena arising from sources such as material hysteresis, interface friction, and geometric nonlinearities. These nonlinear effects become particularly significant under large vibration amplitudes, and ignoring them may result in substantial modeling errors (Balasubramanian *et al.*, 2018; Amabili *et al.*, 2016; Haghdoust *et al.*, 2018). Consequently, current research trends increasingly focus on parametric identification strategies capable of distinguishing linear damping effects from nonlinear contributions, thereby improving the understanding and characterization of energy dissipation mechanisms. Al-hababi *et al.* (2020) provided a comprehensive review of nonlinear damping identification methods, highlighting both their strengths and fundamental limitations. Their study concluded that approaches accounting for nonlinear damping offer a more realistic representation of structural dynamics than conventional linear models. Chatterjee and Chintha (2020) proposed an identification methodology employing harmonic excitation to evaluate damping with third-order nonlinearity. Eberle (2025) presented a computationally economical and nonparametric method dedicated to the analysis of nonlinear damping. Furthermore, Han and Kinoshita (2012) introduced an indirect identification algorithm aimed at determining nonlinear damping vibrating systems with constant stiffness properties. The SLM was later extended to nonlinear systems by Lisitano and Bonisoli (2021), enabling the identification of nonlinear damping using frequency response functions (FRFs) obtained at different vibration amplitudes. In these developments, parametric excitation, such as time-varying stiffness, was not explicitly incorporated into the identification formulation. The results presented in these studies were obtained by assuming a constant mesh stiffness (Km), while the effect of stiffness variation was indirectly introduced through the dynamic response. However, the phenomenon of parametric excitation has attracted considerable attention in various fields of engineering due to its significant influence on the damping identification process (Sofroniou & Bishop, 2014). Parametric excitation arises from time-varying system parameters such as stiffness, mass, or damping (Belhaq *et al.*, 2013). In particular, time-varying stiffness may induce complex dynamic phenomena, including parametric resonance, instability regions, amplitude modulation, and nonlinear response amplification (Guo *et al.*, 2025). Such effects are frequently encountered in aeroelastic systems, civil engineering structures subjected to periodic loading, and rotating machinery (Chen *et al.*, 2024). Recent studies have demonstrated that stiffness variations significantly modify the dynamic characteristics and stability boundaries of mechanical systems (Li *et al.*, 2024). Therefore, neglecting time-varying stiffness in system modeling may lead to inaccurate parameter estimation, especially in damping identification problems. Consequently, the objective of this study is to develop a refined identification technique capable of estimating nonlinear damping in parametrically excited systems while explicitly accounting for the effects of time-varying stiffness. The originality of the proposed method is to extend the SLM for the estimation of nonlinear (SLMnl) damping, in multi-degree-of-freedom (MDOF) systems, while taking into consideration the effects of time-varying stiffness. The harmonic representation of the time-varying dynamic stiffness exploits multiple sidebands of the frequency response function simultaneously. Unlike conventional approaches based on the mean stiffness, the present technique reconstructs the equivalent stiffness matrix by combining the receptances computed at sideband frequencies. The periodic effects of stiffness are expressed through harmonic projections on a trigonometric basis, leading to a linear system $Aa = b$. This formulation makes full use of the information contained in multiple FRFs around the meshing frequency, enabling the simultaneous identification of linear and nonlinear damping coefficients as well as variable stiffness parameters with enhanced accuracy. The developed SLMnl, named the stabilized layers method for nonlinear damping with varying stiffness (SLMnl,kv), explicitly models time-varying stiffness and enables accurate identification of nonlinear damping in MDOF systems. The location of nonlinearity is detected by using nonlinearity location methods, and the time-varying stiffness model is presented by a periodic square wave function. A description of the SLMnl damping estimation with constant stiffness is given in Section 2. The limits of the SLMnl technique in the case of varying stiffness are presented in Section 3. The new SLMnl,kv is described in Section 4. In Section 5, SLMnl,kv is implemented for the identification of nonlinear damping and time-varying stiffness coefficients in spur gear pair systems.

2. Review of the SLMnl damping

The SLMnl presented by Lisitano and Bonisoli (2021) is an estimation technique for nonlinear damping with constant stiffness. A nonlinear damping that depends on the displacement amplitude A was expressed as

$$C(A) = C + C_{eq}(A)gg^T, \tag{2.1}$$

$$C_{eq} = c_{nl,0}gg^T + ... + c_{nl,m}gg^T, \tag{2.2}$$

where g is a vector indicating the location of nonlinear damping and A is the excitation amplitude. In the SLMnl, C is the non-proportional viscous damping. The nonlinear viscous damping $C_{eq}(A)$ was defined by

$$C_{eq}(A) = \sum_{m=0}^{M} v_m c_{nl,m} A^m. \tag{2.3}$$

Replacing the nonlinear viscous damping presented in Eq. (2.1) with Eq. (2.2), and rewriting it in the vector form, yields:

$$C(A) = C + C_{eq}(A) g g^T = \begin{bmatrix} C + c_{nl,0} g g^T \\ c_{nl,1} g g^T \\ \dots \\ c_{nl,m} g g^T \end{bmatrix}. \tag{2.4}$$

The proposed approach aims to estimate both the linear and nonlinear coefficients $c_{nl,0}, c_{nl,1}, \dots$, $c_{nl,m}$ of the damping model C at $M+1$ amplitudes, where M represents the degree of nonlinearity. The equation of motion of the n-DOF system with nonlinear damping in the frequency domain subjected to an external excitation force $f(w)$ as a function of displacement $x(w)$ was presented as follows:

$$\left(K - w^2 M\right) x(w) + iw \left(C + C_{eq}(A) g g^T\right) x(w) = f(w), \tag{2.5}$$

where M, C, and $K \in R^{n,n}$ are the mass, viscous damping, and constant stiffness matrix of the system, respectively. The receptance frequency response matrix $H^R(w)$ was derived to identify the linear and nonlinear damping coefficients by using the following equation:

$$\left[w H^R(w)\right] \left[C + C_{eq}(A) g g^T\right] = G(A, w), \tag{2.6}$$

where $G(w)$ was determined from the equivalent linear damped $H^C(w)$ as follows:

$$G(A, w) = -H_I^C(A, w) \left[H_R^C(A, w)\right]^{-1}, \tag{2.7}$$

the equivalent linear damped H^C is presented by

$$H^C(w) = K - w^2 M + iw \left(C + C_{eq}(A) g g^T\right), \tag{2.8}$$

and $H_R^C(A, w)$ is the real part, and $H_I^C(A, w)$ is the imaginary part of the receptance $H^C \in C^{n,n}$. The dynamic stiffness matrix undamped H^R(w) was presented by the following equation:

$$\left[H^R(w)\right]^{-1} = K - w^2 M. \tag{2.9}$$

Equation (2.6) can be presented at $M+1$ amplitudes by

$$\left[w H^R(w) w H^R(w) v^1 A \ \dots \ w H^R(w) v^M A^M\right] \left[C + C_{eq}(A) g g^T\right] = G(A, w). \tag{2.10}$$

In order to solve Eq. (2.10), the layers method was applied. The damping matrix is presented for relative and absolute dampers. The relative layer presents the connection between two DOFs, and the absolute layer represents the connection between the DOF and the external frame. Therefore, the linear damping matrix can be presented as the following sum of NL layers:

$$\mathbf{C} = \sum_{1}^{NL} \mathbf{C}_j = \sum_{p=1}^{NA} c_p \mathbf{P}_p^A + \sum_{p=1}^{NR} c_q \mathbf{P}_q^R; \qquad \mathbf{C} = \left[P_1^A \dots P_{NA}^A P_1^R \dots P_{NR}^R\right] \begin{bmatrix} C_1 I \\ \dots \\ C_{NA} I \\ C_{NA+1} I \\ \dots \\ C_{NA+NR} I \end{bmatrix}, \tag{2.11}$$

where P_p^A and P_q^R are the absolute and relative patterns. M layers are added to represent the nonlinear damping coefficients $c_{nl,m}$. Therefore, Eq. (2.10) can be presented in the form:

$$\begin{bmatrix} V(A1) \\ V(A2) \\ \dots \\ V(AM+1) \end{bmatrix} \begin{bmatrix} P & & & \\ & P_{nl} & & \\ & & \dots & \\ & & & P_{nl} \end{bmatrix} \begin{bmatrix} c_1 I \dots c_{NA+NR} I \\ c_{nl,1} I \\ \\ c_{nl,M} I \end{bmatrix} = \begin{bmatrix} G(A1) \\ G(A2) \\ \dots \\ G(AM+1) \end{bmatrix}. \tag{2.12}$$

The first line of the matrix presents the viscous damping, and the M lines present the nonlinear damping coefficients. Finally, Eq. (2.12) was presented in the form $Aa = b$. Using the linear least square method, the unknown damping coefficients of the vector $a = [c_1 \dots. c_{NA+NR} c_{nl,1} \dots c_{nl,M}]^T$ can be obtained. As presented in Eq. (2.12), stiffness was assumed to be constant, and the effect of time-varying stiffness was not explicitly incorporated into the damping identification. The SLMnl provides valuable contributions to damping identification, but it assumes a constant system, and therefore, neglects the influence of stiffness variation on the damping identification technique. Therefore, in the proposed technique presented in this study, all equations should be reformulated to identify nonlinear damping with time-varying stiffness. The extended algorithm is presented in Section 3.

3. Nonlinear-damped systems with time-varying stiffness

The equation of motion of n DOFs with nonlinear damping and time-varying stiffness can be written as follows:

$$M\ddot{x}(t) + C(A)\dot{x}(t) + (K + K(t))\, x(t) = f(t). \tag{3.1}$$

The damping matrix is presented by Eq. (2.1). The time-varying stiffness $K(t)$ presented in Fig. 1 is given by the following equation (Yousfi *et al.*, 2018):

$$K(t) = K_0 + \sum_{h=1}^{Nh} (K_h^c \cos(h w_m t) + K_h^s \sin(h w_m t)), \tag{3.2}$$

where K_h^c and K_h^s are the harmonic coefficients of the time-varying stiffness. Nh is the number of harmonic sidebands, and w_m is the mesh frequency. The oscillations observed in Fig. 1 result from the periodic representation of the time-varying mesh stiffness in the form of a Fourier series representation. This modulating variation creates additional components in the system's dynamic response, called sidebands, located around the excitation frequency ω. The number of

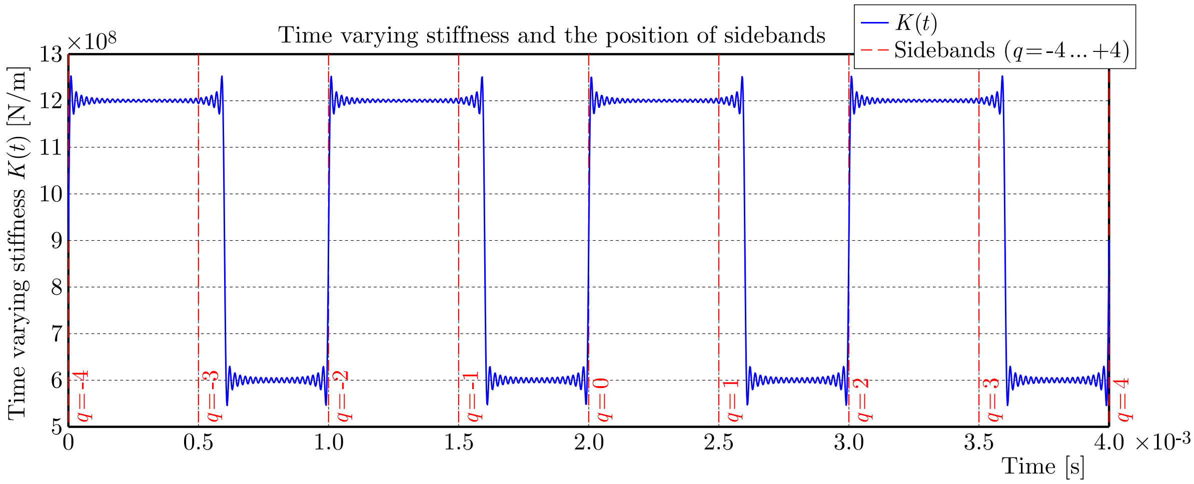

Fig. 1. Time varying stiffness.

sidebands is equal to $2Nh+1$. The sidebands are shown in Fig. 1 for $Nh=4$. These harmonics introduce local oscillatory fluctuations, especially near the transitions between single and double tooth contact regions. When such systems exhibit a nonlinear damping and time-varying stiffness, the dynamic behavior becomes even more complex, and the traditional SLMnl can affect the damping identification. The SLMnl is applied in a numerical example with varying stiffness in Section 3.1 to present its limits in identifying the nonlinear damping.

3.1. Limits of SLMnl damping identification in the case of time-varying stiffness

The SLMnl is applied to evaluate its limitations in the case of time-varying stiffness presented in Section 2. As an example, we consider a system with time-varying stiffness $K(t)$, the mass matrix M, and a viscous damping matrix C presented by

$$\begin{aligned} &M=\begin{bmatrix} 2 & & \\ & 5 & \\ & & 3 \end{bmatrix}, \qquad K=10^4\begin{bmatrix} 5 & 3 & 0 \\ 3 & 5 & 2 \\ 0 & 2 & 1 \end{bmatrix}, \qquad C=10^5\begin{bmatrix} 7 & 3 & 0 \\ 3 & 8 & 2 \\ 0 & 2 & 5 \end{bmatrix}, \\ &f_{c,nl}=g(c_0+c_2x^2)\dot{x}, \qquad c_0=140, \qquad c_2=1.35e5, \end{aligned} \tag{3.3}$$

where $f_{c,nl}$ is the nonlinear damping force, and is applied on the first DOF, so that $g=(10\ 0)$. We added a time-varying stiffness, which can be modeled by a periodic square wave function presented in Eq. (3.2). In the method presented by Lisitano and Bonisoli (2021), the stiffness should be constant. Therefore, the mean value of $K(t)$ is considered. The first step of the SLMnl is to find the receptance function Hc, which is presented in Fig. 2. As it is presented, the system responses do not exhibit any signs of nonlinear behavior. As the excitation amplitude increases, the FRF curves remain almost superimposed, indicating that the response does not vary significantly with amplitude. This behavior suggests that the nonlinear damping effect is not properly identified, either. Consequently, the SLMnl approach fails to capture nonlinear damping when applied to systems with variable stiffness and using the mean value of stiffness. Figure 3 and Fig. 4 present damping coefficients identified at low and high frequencies. At low

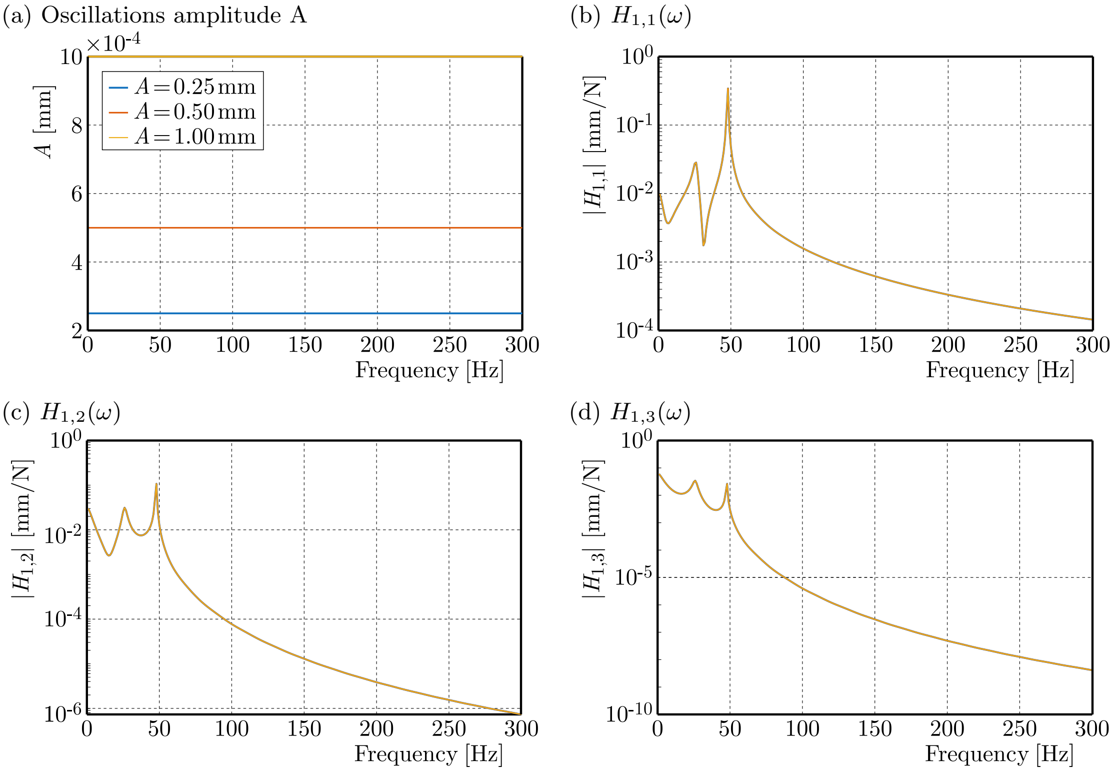

Fig. 2. Frequency response functions (FRFs) obtained with SLMnl.

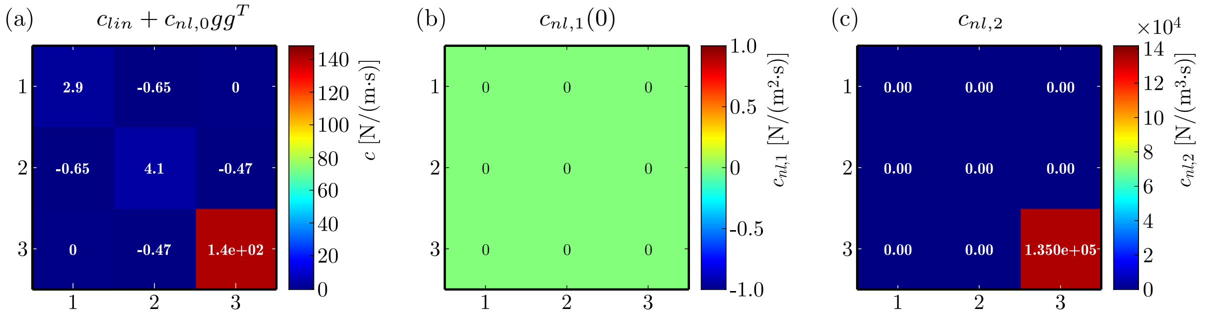

Fig. 3. Damping coefficients at low frequency computed with SLMnl.

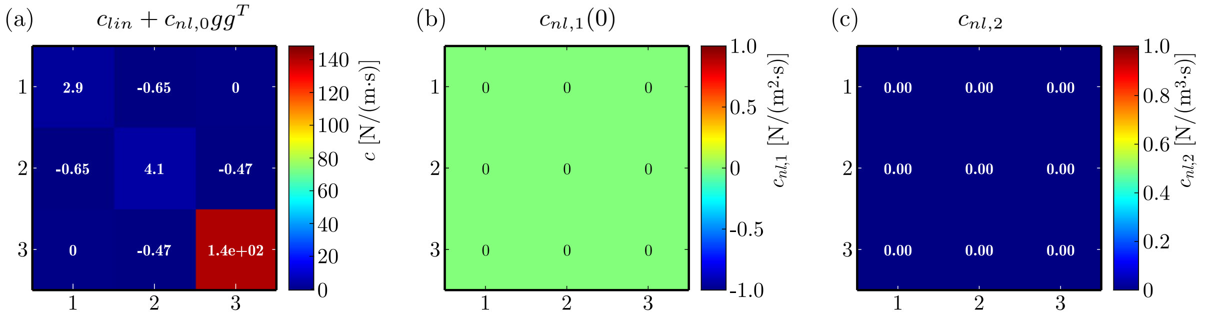

Fig. 4. Damping coefficients at high frequency computed with SLMnl.

frequency, a good correspondence is obtained with the real nonlinear coefficients $c_0 = 140$, $c_2 = 1.35e5$. However, the nonlinear coefficient c_2 identified by the SLMnl at high frequency is zero, different from the real value $c_2 = 1.35e5$. Therefore, this result suggests that, under low-frequency excitation, the system response remains sufficiently dominated by the modeled nonlinear damping effects, and the underlying assumptions of the SLMnl formulation remain valid. In contrast, at high frequency, the nonlinear damping coefficient c_2 identified by the SLMnl collapses to zero, which is a significant deviation from its true value. This behavior highlights a clear limitation of the SLMnl approach when applied to high-frequency dynamics. At elevated frequencies, the system response becomes increasingly influenced by inertial effects and higher-order dynamic interactions, which can mask the contribution of nonlinear damping. As a result, the SLMnl fails to properly isolate and estimate the nonlinear damping component. Overall, these results demonstrate that the SLMnl is highly sensitive to the selected frequency range. While it provides reliable damping identification at low frequencies, its performance degrades significantly at high frequencies due to the combined effects of unmodeled stiffness variations and reduced observability of nonlinear damping. Consequently, the SLMnl formulation presented by Lisitano and Bonisoli (2021) assumes a constant stiffness, and its applicability is limited for systems with time-varying stiffness, particularly at higher frequencies. For accurate damping estimation over a wide frequency range, it is necessary to extend the SLMnl formulation presented by Lisitano and Bonisoli (2021) to explicitly incorporate time-varying mesh stiffness. Therefore, the novelty of the present work lies in reformulating the SLMnl to add a time-varying stiffness effect. The proposed method is presented in Section 4.

4. Nonlinear damping identification in the case of time-varying stiffness

4.1. Stabilized layers method for nonlinear damping with varying stiffness (SLMnl,kv)

The equation of motion of the n-DOF system with nonlinear damping and time-varying stiffness can be expressed in the frequency domain as follows:

$$M\ddot{x}(w) + iw(C + C_{eq}(A)gg^T)x(w) + (K + K(w_m))\,x(w) = f(w), \tag{4.1}$$

where $f_{c,nl} = iwC_{eq}(A)gg^T$ is the nonlinear damping force, $x(w)$ is the displacement in the frequency domain, and $f(w)$ is the excitation force in the frequency domain. C_{eq} is the nonlinear damping matrix given by Eq. (2.4). The time-varying stiffness $K(t)$ is given by Eq. (3.2). The idea of the proposed SLMnl,kv is to identify the harmonic coefficients K_h^c and K_h^s together with the linear and nonlinear coefficients. Therefore, two vectors must be identified. One is a vector which contains the harmonic coefficients of the time-varying stiffness defined by

$$\kappa = \left[\kappa_{c,1}, \kappa_{s,1}, ..., \kappa_{c,Nh}, \kappa_{s,Nh}\right]^T, \tag{4.2}$$

and the other is a vector which contains the linear and nonlinear coefficients of the damping, as follows:

$$u_{lin+nl} = \left[c_1, ..., c_{NA+NR}, c_{nl,1}, ..., c_{nl,M}\right]^T. \tag{4.3}$$

The periodic variation of the stiffness $K(t)$ acts as a parametric excitation that modulates the vibration response of the system, resulting in the appearance of frequency sidebands (at $\pm w_m$, $\pm 2w_m$, ...) around the central excitation frequency w_m. Therefore, the selection of a frequency range around w_m can overcome the limits of the current SLMnl. The frequency range was selected around each sideband. The frequency range is presented by $w_{q,i} = w_i + qw_m$, $q \in \{-Nh, ..., Nh\}$, $i \in \{1, ..., K\}$. The dynamic stiffness matrix of the undamped system around each sideband $H^R(w_q)$ can be presented as follows:

$$\left[H^R(w_q)\right]^{-1} = K - w_q^2 M, \tag{4.4}$$

by multiplying Eq. (4.1) by $H^R(w_q)$, we obtain:

$$\begin{aligned} x(w_q) &+ H^R(w_q)\left(iw_q\left(C + C_{eq}(A)gg^T\right)\right)x(w_q) \\ &+ \left(\sum_{h=1}^{Nh} H^R(w_q)\left(K_h^c \cos(hw_m t) + K_h^s \sin(hw_m t)\right)\right)x(w_q) = H^R(w_q)f(w_q). \end{aligned} \tag{4.5}$$

Here, the product $H^R(w_q)\left(iw_q C(A)\right)$ naturally appears to indicate that it originates from the damping term, and the terms $\sum\limits_{h=1}^{Nh} H^R(w_q)\left(K_h^c \cos(hw_m t) + K_h^s \sin(hw_m t)\right)$ arise from the modulation of time-varying stiffness $K(t)$.

Therefore, the vector of displacement can be presented as follows:

$$\begin{aligned} x(w_q) = \Bigg[& 1 + H^R(w_q)\left(iw_q C + C_{eq}(A)gg^T\right) \\ & + \left(\sum_{h=1}^{Nh} H^R(w_q)\left(K_h^c \cos(hw_m t) + K_h^s \sin(hw_m t)\right)\right)\Bigg]^{-1} H^R(w_q)f(w_q). \end{aligned} \tag{4.6}$$

The transformation matrix $G(A, w_q)$ can be presented by

$$\begin{aligned} G(A, w_q) = {} & w_q H^R(w_q)\left(C + C_{eq}(A)gg^T\right) \\ & + \left(\sum_{h=1}^{Nh} H^R(w_q)\left(K_h^c \cos(hw_m t) + K_h^s \sin(hw_m t)\right)\right). \end{aligned} \tag{4.7}$$

At this stage, the stiffness modulation generates additional sideband coupling terms in the system equations. Specifically, the dissipative contribution $V_q(w_q, A) \in \mathbb{R}^{n,n}$, which is a complex block matrix associated with the q-th sideband, is defined, and the modulated contribution is presented by the vector $\nu_q \in \mathbb{R}^{n,n}$ due to the time-varying stiffness associated with the q-th sideband. These terms modify the block matrix structure. Such modulation-induced terms do not appear in the method proposed by Lisitano and Bonisoli (2021), since their model assumes constant stiffness and therefore does not generate time-periodic coefficients.

Therefore, for each sideband, we can write:

$$\begin{aligned} G(A, w_q) = {} & V_q(w_q, A)\left(C + C_{eq}(A) g g^T\right) \\ & + \nu_q(w_q, A)\left(\sum_{h=1}^{Nh}\left(K_h^c \cos(h w_m t) + K_h^s \sin(h w_m t)\right)\right). \end{aligned} \tag{4.8}$$

To transform Eq. (4.7) into the matrix form, we used the vector of harmonic coefficients presented by Eq. (4.2). Then, we introduced two vectors for cosine and sine combinations:

$$\begin{aligned} P_c^{(h)} &= \sum_{h=1}^{Nh} \cos(h w_m t)\nu_q(w_q, A), \\ P_s^{(h)} &= \sum_{h=1}^{Nh} \sin(h w_m t)\nu_q(w_q, A). \end{aligned} \tag{4.9}$$

The vectors of cosine and sine combinations are arranged in the matrix $A_\kappa \in \mathbb{C}^{n^2 \times N_k}$ with $N_k = 2Nh$ defined by

$$A_\kappa = \left[P_c^1, P_s^1, ..., P_c^{Nh}, P_s^{Nh}\right]. \tag{4.10}$$

By substituting the definition of time-varying stiffness with Eq. (3.2) and Eq. (4.9), and replacing the definition of the nonlinear viscous damping coefficients with Eq. (2.4), a matrix form of Eq. (4.7) is written in the frequency range $w_{q,i} = w_i + q w_m$, $q \in \{-Nh, ..., Nh\}$, $i \in \{1, ..., K\}$:

$$\begin{bmatrix} w_q H_R(w_{q,1}) \\ w_q H_R(w_{q,2}) v_1 A^1 \\ ... \\ w_q H_R(w_{q,K}) v_M A^M \end{bmatrix} \begin{bmatrix} C + c_{nl,0} g g^T \\ c_{nl,1} g g^T \\ ... \\ c_{nl,m} g g^T \end{bmatrix} + \begin{bmatrix} P_c^1 \\ P_s^1 \\ ... \\ P_c^{Nh} \\ P_s^{Nh} \end{bmatrix} \begin{bmatrix} \kappa_{c,1} \\ \kappa_{s,1} \\ \\ \kappa_{c,Nh} \\ \kappa_{s,Nh} \end{bmatrix} = \begin{bmatrix} G(A, w_{q,1}) \\ G(A, w_{q,2}) \\ ... \\ G(A, w_{q,K}) \end{bmatrix}. \tag{4.11}$$

Let

$$V(A) = \begin{bmatrix} w_q H_R(w_{q,1}) \\ w_q H_R(w_{q,2}) v_1 A^1 \\ ... \\ w_q H_R(w_{q,K}) v_M A^M \end{bmatrix} \in \mathbb{R}^{nK, n(M+1)}, \quad G(A) = \begin{bmatrix} G(A, w_{q,1}) \\ G(A, w_{q,2}) \\ ... \\ G(A, w_{q,K}) \end{bmatrix} \in \mathbb{R}^{nK,n}.$$

The layers method presented in Section 2 by Eq. (2.11) was applied for $M + 1$ different values of the amplitude A. The following equation can be obtained:

$$\overline{VP} \begin{bmatrix} c_1 I ... c_{NA+NR} I \\ c_{nl,1} I \\ \\ c_{nl,M} I \end{bmatrix} + A_\kappa \begin{bmatrix} \kappa_{c,1} \\ \kappa_{s,1} \\ \\ \kappa_{c,Nh} \\ \kappa_{s,Nh} \end{bmatrix} = \overline{G}, \tag{4.12}$$

where

$$\overline{V(A)} = \begin{bmatrix} V_q(A1) \\ V_q(A2) \\ ... \\ V_q(AM+1) \end{bmatrix} \mathbb{R}^{nK(M+1), n(M+1)}, \qquad \overline{G}(A) = \begin{bmatrix} G(A1) \\ G(A2) \\ ... \\ G(AM+1) \end{bmatrix} \in \mathbb{R}^{nK(M+1), n},$$

$$\overline{P} = \begin{bmatrix} P & & & \\ & P_{nl} & & \\ & & .. & \\ & & & P_{nl} \end{bmatrix} \in \mathbb{R}^{n^2K(M1),NA+NR+M}.$$

In order to identify the harmonic coefficients $\kappa = [\kappa_{c,1}, \kappa_{s,1}, ..., \kappa_{c,Nh}, \kappa_{s,Nh}]^T$ and the linear and nonlinear damping coefficients $u_{lin+nl} = [c_1, ..., c_{NA+NR}c_{nl,1}, ..., c_{nl,M}]^T$, the matrices $Zi \in \mathbb{R}^{n(NA+NR+M),(NA+NR+M)}$ and $Yi \in \mathbb{R}^{n,1}$ are introduced to isolate the correct coefficients in the vector u_{lin+nl}. Zi is associated with the coefficients in $\overline{V}$, and Yi is associated with those in $\overline{G}$. They mostly contain 0 and 1, used to pick out the relevant terms for each equation:

$$\begin{aligned} &Zi = 0 \quad \text{and} \quad (Zi)_{(y-1)_{n,y}} = 1 \quad \text{with} \quad y = 1, ..., NA + NR + M, \\ &Yi = 0 \quad \text{and} \quad (Yi)_{i,1} = 1. \end{aligned} \tag{4.13}$$

Equation (4.12) can be presented as follows:

$$\begin{bmatrix} \overline{VP}Z1 \\ \overline{VP}Z2 \\ ... \\ \overline{VP}Zn \end{bmatrix} u_{lin+nl} + A_\kappa \kappa = \overline{G}. \tag{4.14}$$

A summation is carried out over all Nh sidebands:

$$\sum_1^{Nh} \begin{bmatrix} \overline{VP}Z1 \\ \overline{VP}Z2 \\ ... \\ \overline{VP}Zn \end{bmatrix} u_{lin+nl} + \sum_1^{Nh} A_\kappa \kappa = \overline{Q}. \tag{4.15}$$

Finally, we introduced the matrix form $Aa = b$, which can be solved using the linear least squares method:

$$\sum_1^{Nh} \begin{bmatrix} A_{lin+nl}(A, w_q) & A_\kappa(A, w_q) \end{bmatrix} \begin{bmatrix} u_{lin+nl} \\ \kappa \end{bmatrix} = \text{vec}\,(Q(A, w_q)), \tag{4.16}$$

where

$$A_{lin+nl}(A, w_q) = \begin{bmatrix} \overline{VP}Z1 \\ \overline{VP}Z2 \\ ... \\ \overline{VP}Zn \end{bmatrix}.$$

We can conclude that, in the SLMnl,kv, the effect of time-varying stiffness is introduced in the identification formulation compared with the SLMnl, which neglected the time-varying stiffness effect. The last step of the proposed technique is to verify its reliability using a global stability matrix for different amplitudes and spectral lines K:

$$S = \bigcap_{h=1}^{NA+NR+M} S_h, S_h(k, r) = 1 \quad \text{if} \quad \frac{c_{hkr} - c_{hk+jr+i}}{c_{hkr}} \le \varepsilon \forall (i, j) = \pm 1. \tag{4.17}$$

4.2. Numerical example

In order to prove the suitability of the new SLMnl,kv for damping identification in the case of time-varying stiffness, a numerical example presented in Section 3 is used. The steps of the SLMnl,kv are applied. Figure 5 presents the damping matrices identified by the SLMnl,kv at high frequency. A good correspondence is obtained with the damping matrices of Eq. (3.3). We can conclude that the SLMnl,kv approach overcomes the limitations of the SLMnl through its new formulation, which explicitly considers the effect of stiffness variation by defining spectral frequency w_q.

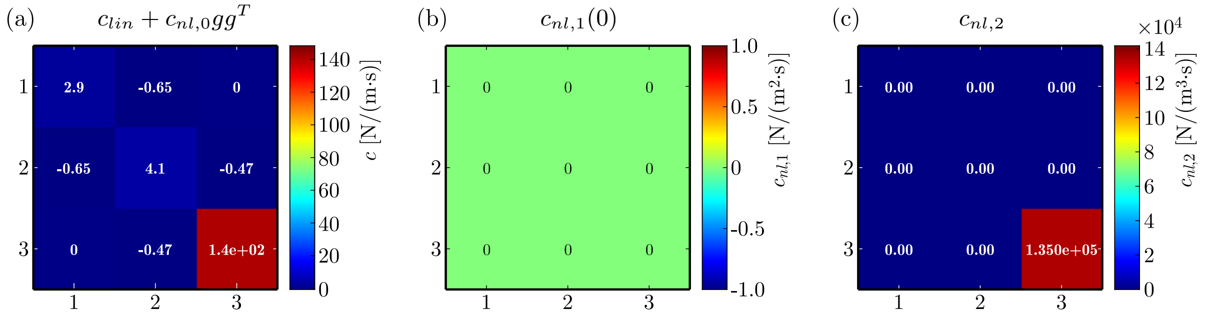

Fig. 5. Damping coefficients at high frequency computed with SLMnl,kv.

5. Identification of nonlinear damping in spur gear pair system

The SLMnl,kv, proposed in Section 4, is applied in a spur gear pair system. The numerical response employed in this work is obtained using the dynamic model described in the dynamic analysis of spur gear systems presented by Wei *et al.* (2021), which has been experimentally validated on a dedicated test bench. In that study, the simulated vibration responses were compared with measured data, showing a good agreement in both time and frequency domains. The values of the mass, stiffness, and gear variables are obtained from this reference model, and the vibration signal is derived through the numerical integration of the model equations. In Section 5.1 the linear structural damping and nonlinear damping due to the interaction between the pinion and gear are identified using the proposed SLMnl,kv.

5.1. Model of spur gear pair system

The dynamic model of the spur gear pair system is presented in Fig. 6. The system is composed of a gear, pinion, load, and motor. The contact between the pinion and the motor is represented by torsional stiffness k_{c1} and torsional damping c_{c1}, while k_{c2} and c_{c2} represent the contact between the gear and the load. k_{x1}, k_{y1}, c_{x1}, and c_{y1} are the equivalent support stiffness and the equivalent support damping in the two directions, x and y, of the pinion. k_{x2}, k_{y2}, c_{x2}, and c_{y2} are the equivalent support stiffness and the equivalent support damping in the two directions, x and y, of the gear. The dampers c_{x1}, c_{y1}, c_{x2}, and c_{y2}, which are not plotted in

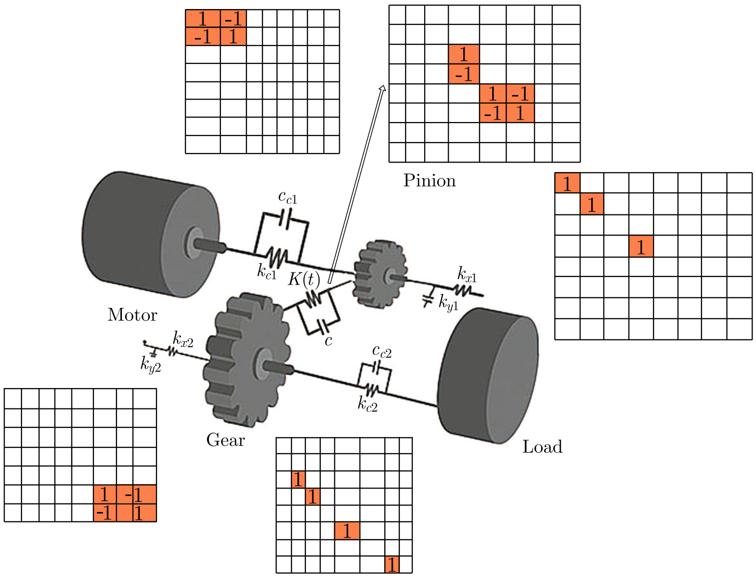

Fig. 6. Absolute and relative layers representation.

Fig. 6, will be given in the equation of motion. The mesh damping model utilized in this study is quadratic nonlinear with the nonlinear damping force, as follows:

$$f_{cnl} = \left(c_{nl,0} + c_{nl,2}x^2\right)\dot{x}, \tag{5.1}$$

where

$$c_{nl,0} = 240 \qquad \text{and} \qquad c_{nl,2} = 2.4e8.$$

θm, θ_1, θ_1, θ_L are the angular displacements of the motor, the pinion, the gear, and the load. x_1, y_1, x_2, y_2 are the displacements of the pinion and the gear in the x-, y-directions. Therefore, the system presents 8 DOFs. The equation of motion of the spur gear pair system is given by

$$M\ddot{x}(t) + (C + C_b)\,\dot{x}(t) + (Kb + K(t))\,x(t) = f(t), \tag{5.2}$$

where $x(t)$ represents the displacement vector expressed as

$$x(t) = [x_1, y_1, \theta m, \theta_1, \theta_1, \theta_L, x_2, y_2], \tag{5.3}$$

$f(t)$ is the excitation force, M is the mass matrix, and C_b is structural damping. The contact between the gear and the pinion is modeled by a time-varying stiffness and structural stiffness $K = K(t) + Kb$, where $K(t)$ is the time-varying stiffness presented in Section 2 by Eq. (3.2) as follows:

$$M = \begin{bmatrix} m_1 &&&&&&& \\ & m_1 &&&&&& \\ && I_m &&&&& \\ &&& I_1 &&&& \\ &&&& m_2 &&& \\ &&&&& m_2 && \\ &&&&&& I_L & \\ &&&&&&& I_2 \end{bmatrix}, \tag{5.4}$$

$$K_b = \begin{bmatrix} k_{x1} &&&&&&& \\ & k_{y1} &&&&&& \\ && k_{c1} & -k_{c1} &&&& \\ && -k_{c1} & k_{c1} &&&& \\ &&&& k_{x2} &&& \\ &&&&& k_{y2} && \\ &&&&&& k_{c2} & -k_{c2} \\ &&&&&& -k_{c2} & k_{c2} \end{bmatrix},$$

$$C_b = \begin{bmatrix} c_{x1} &&&&&&& \\ & c_{y1} &&&&&& \\ && c_{c1} & -c_{c1} &&&& \\ && -c_{c1} & c_{c1} &&&& \\ &&&& c_{x2} &&& \\ &&&&& c_{y2} && \\ &&&&&& c_{c2} & -c_{c2} \\ &&&&&& -c_{c2} & c_{c2} \end{bmatrix}. \tag{5.5}$$

5.2. Nonlinear damping identification

The nonlinear damper is located at the contact between the pinion and the gear. Therefore, $g = [0\ 0\ 0\ 10\ 0\ 0\ 1]$. The degree of nonlinearity $M = 2$. The SLMnl,kv is applied for 3 amplitudes $A = [0.25\ 0.5\ 1]$. Two absolute layers are defined to present the contact between the pinion support, and the contact gear support. Three relative layers are defined to show the pinion-motor, pinion-gear and gear-load contacts. Two layers $P_{nl} = gg^T$ are defined to identify the nonlinear coefficients. All layers are presented in Fig. 7.

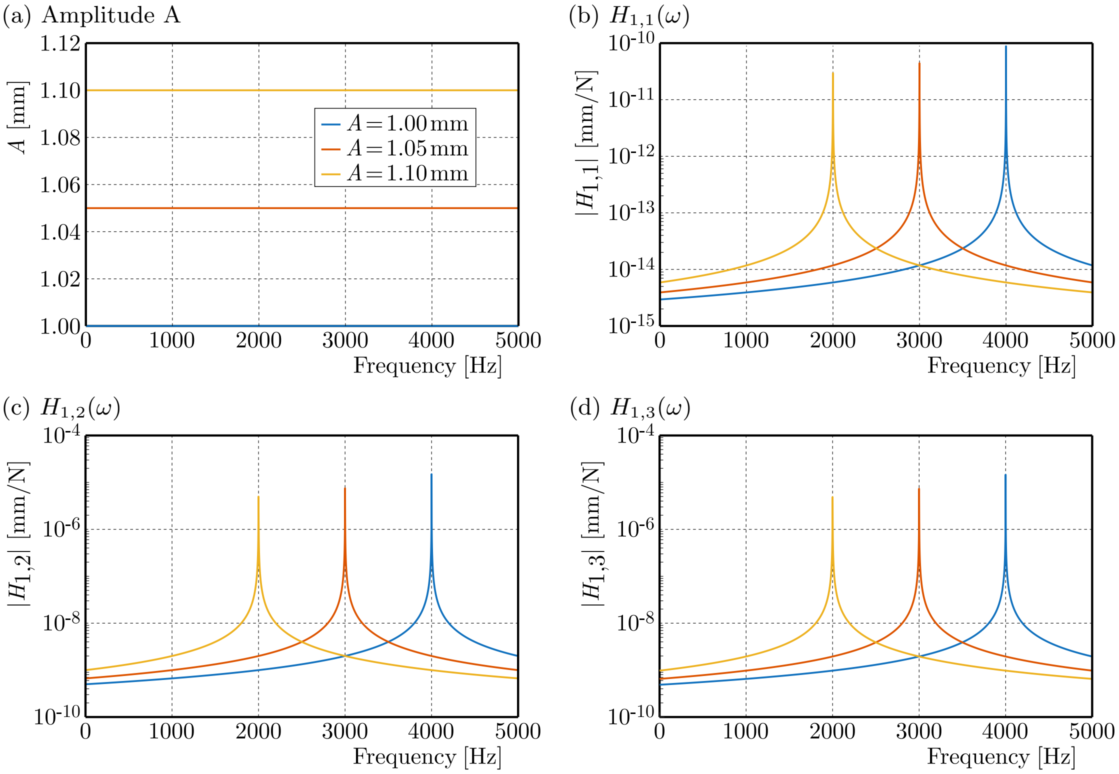

Fig. 7. Frequency response functions (FRFs) obtained with SLMnl,kv.

We defined the vector composed by linear and nonlinear damping coefficient:

$$u_{lin+nl} = \left[\frac{c_{x1} + c_{y1}}{2}, \frac{c_{x2} + c_{y2}}{2}, c_{c1}, c_{nl,0}, c_{c2}, c_{nl,1}, c_{nl,2}\right]. \tag{5.6}$$

The frequency range is presented by $w_{q,i} = w_i + qw_m$, $q \in \{-Nh, ..., Nh\}$, $i \in \{1, ..., K\}$, where $w_m = \frac{2\pi}{T_1}$, T_1 represents the mesh period of the gear system calculated by $T_1 = \frac{60}{NZ_1}$, where N is the input rotational speed and z_1 is the tooth number of the pinion. The first step of the SLMnl,kv is to find the receptance function Hc, which is presented in Fig. 7. We can conclude that the effects of nonlinearity are visible. As the amplitude A increases, both the second and third peaks decrease in amplitude and move toward lower frequencies, while the first peak remains essentially unchanged. The FRFs exhibit a pronounced amplitude dependency, characterized by a progressive shift of resonance frequencies toward lower values as the excitation amplitude increases. This behavior indicates a dominant softening nonlinearity induced by the gear mesh stiffness variation. Moreover, the limited growth of resonance peaks at higher amplitudes highlights the presence of nonlinear damping mechanisms. Figure 8 presents the identified linear damping matrices, the damping values obtained using the SLMnl,kv correspond closely to the reference values $c_{nl,0} = 240$, confirming the accuracy of the proposed identification strategy for linear dissipation. Figure 9a presents the nonlinear damping coefficient $c_{nl,1}$, which corresponds to the real value $c_{nl,1} = 0$, indicating that the method is able to capture the first-order

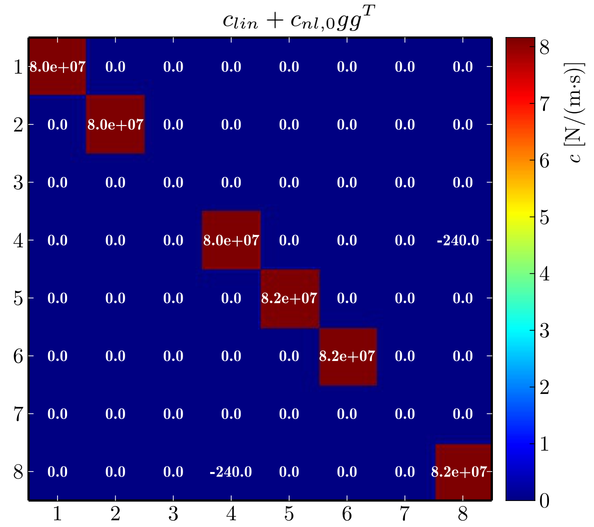

	1	2	3	4	5	6	7	8
1	8.0e+07	0.0	0.0	0.0	0.0	0.0	0.0	0.0
2	0.0	8.0e+07	0.0	0.0	0.0	0.0	0.0	0.0
3	0.0	0.0	0.0	0.0	0.0	0.0	0.0	0.0
4	0.0	0.0	0.0	8.0e+07	0.0	0.0	0.0	-240.0
5	0.0	0.0	0.0	0.0	8.2e+07	0.0	0.0	0.0
6	0.0	0.0	0.0	0.0	0.0	8.2e+07	0.0	0.0
7	0.0	0.0	0.0	0.0	0.0	0.0	0.0	0.0
8	0.0	0.0	0.0	-240.0	0.0	0.0	0.0	8.2e+07

Fig. 8. Linear damping coefficients computed with SLMnl,kv.

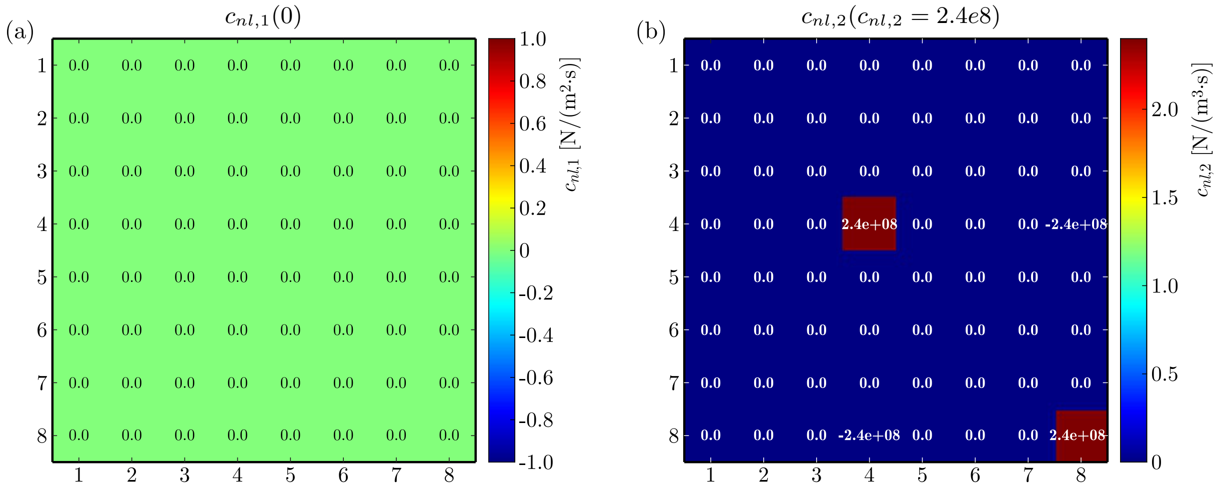

(a)

	1	2	3	4	5	6	7	8
1	0.0	0.0	0.0	0.0	0.0	0.0	0.0	0.0
2	0.0	0.0	0.0	0.0	0.0	0.0	0.0	0.0
3	0.0	0.0	0.0	0.0	0.0	0.0	0.0	0.0
4	0.0	0.0	0.0	0.0	0.0	0.0	0.0	0.0
5	0.0	0.0	0.0	0.0	0.0	0.0	0.0	0.0
6	0.0	0.0	0.0	0.0	0.0	0.0	0.0	0.0
7	0.0	0.0	0.0	0.0	0.0	0.0	0.0	0.0
8	0.0	0.0	0.0	0.0	0.0	0.0	0.0	0.0

(b)

	1	2	3	4	5	6	7	8
1	0.0	0.0	0.0	0.0	0.0	0.0	0.0	0.0
2	0.0	0.0	0.0	0.0	0.0	0.0	0.0	0.0
3	0.0	0.0	0.0	0.0	0.0	0.0	0.0	0.0
4	0.0	0.0	0.0	2.4e+08	0.0	0.0	0.0	-2.4e+08
5	0.0	0.0	0.0	0.0	0.0	0.0	0.0	0.0
6	0.0	0.0	0.0	0.0	0.0	0.0	0.0	0.0
7	0.0	0.0	0.0	0.0	0.0	0.0	0.0	0.0
8	0.0	0.0	0.0	-2.4e+08	0.0	0.0	0.0	2.4e+08

Fig. 9. (a) Nonlinear damping coefficient $c_{nl,1}$ computed with SLMnl,kv; (b) nonlinear damping coefficient $c_{nl,2}$ computed with SLMnl,kv.

nonlinear dissipation mechanism associated with the gear mesh. Figure 9b presents the nonlinear damping coefficient $c_{nl,2}$, which corresponds to the real value $c_{nl,2} = 2.4e8$, demonstrating the capability of the method to identify higher-order nonlinear effects. From the obtained results, linear and nonlinear coefficients can be correctly estimated using the proposed new formulation of the SLMnl,kv technique. Therefore, the option that the damping identification is performed in each frequency range $w_{q,i} = w_i + q w_m$, $q \in \{-Nh, ..., Nh\}$, $i \in \{1, ..., K\}$ helps find the real linear and nonlinear damping coefficients. Furthermore, performing the damping identification separately within each frequency range significantly improves the robustness of the estimation, as it allows the method to account for amplitude-dependent stiffness variations and localized resonance phenomena. This frequency-dependent identification strategy enhances the physical consistency of the identified parameters and enables an accurate reconstruction of the system's dynamic behavior across different operating conditions.

6. Conclusion

A new technique is proposed of nonlinear damping estimation in a mechanical system with n DOFs in the case of time-varying stiffness. The time-varying stiffness is characterized by a periodic variation around the excitation frequency w_m, which leads to the appearance of Nh sidebands in the system's response. Each sideband is characterized by a spectral frequency around each frequency. If the effect of the time-varying stiffness is not considered during the damping identification process, as it is presented in the traditional methods, significant estimation errors may arise due to the modulation of the dynamic behavior of the system. Therefore, an appropriate consideration of time-varying stiffness effects leads to a better identification of the linear and nonlinear damping coefficients. The idea of this research is to account for the time-varying stiffness on sidebands. Then, the estimation process is applied in each sideband. The identified harmonic coefficients and linear and nonlinear damping coefficients are obtained by summation over all sidebands. Since the gear systems are characterized by a time-varying stiffness, the SLMnl,kv is applied to estimate nonlinear damping in the spur gear pair system. In conclusion, the proposed SLMnl,kv approach offers a promising solution for the estimation of nonlinear damping in dynamic systems. Future work can focus on further refining this method to test its applicability to identifying damping in the case of backlash, including experimental validation, where contact loss and re-engagement introduce strong nonlinearities and piecewise stiffness variations. Incorporating such effects into the identification framework would enable the assessment of the method's robustness under more complex dynamic conditions.

References

1. Al-hababi, T., Cao, M., Saleh, B., Alkayem, N.F., & Xu, H. (2020). A critical review of nonlinear damping identification in structural dynamics: Methods, applications, and challenges. *Sensors*, *20*(24), Article 7303. https://doi.org/10.3390/s20247303
2. Amabili, M., Alijani, F., & Delannoy, J. (2016). Damping for large-amplitude vibrations of plates and curved panels, part 2: Identification and comparisons. *International Journal of Non-Linear Mechanics*, *85*, 226–240. https://doi.org/10.1016/j.ijnonlinmec.2016.05.004
3. Balasubramanian, P., Ferrari, G., & Amabili, M. (2018). Identification of the viscoelastic response and nonlinear damping of a rubber plate in nonlinear vibration regime. *Mechanical Systems and Signal Processing*, *111*, 376–398. https://doi.org/10.1016/j.ymssp.2018.03.061
4. Belhaq, M., Kirrou, I., & Mokni, L. (2013). Periodic and quasiperiodic galloping of a wind-excited tower under external excitation. *Nonlinear Dynamics*, *74*(3), 849–867. https://doi.org/10.1007/s11071-013-1010-9
5. Bonisoli, E., Lisitano, D., & Vigliani, A. (2019). Damping identification and localisation via Layer Method: Experimental application to a vehicle chassis focused on shock absorbers effects. *Mechanical Systems and Signal Processing*, *116*, 194–216. https://doi.org/10.1016/j.ymssp.2018.06.013
6. Chatterjee, A., & Chintha, H.P. (2020). Identification and parameter estimation of cubic nonlinear damping using harmonic probing and Volterra series. *International Journal of Non-Linear Mechanics*, *125*, Article 103518. https://doi.org/10.1016/j.ijnonlinmec.2020.103518
7. Chen, R., Lv, J., Tian, J., Ai, Y., Zhang, F., & Yao, Y. (2024). Modeling and nonlinear dynamic characteristics analysis of fault bearing time-varying stiffness-flexible rotor coupling system. *Mathematics*, *12*(22), Article 3591. https://doi.org/10.3390/math12223591
8. Clough, R.W., & Penzien, J. (1993). *Dynamics of structures* (2nd ed.). McGraw-Hill.
9. Eberle, R. (2025). Estimating nonlinear damping for mechanical single-degree-of-freedom systems: A robust and effective approach. *Proceedings in Applied Mathematics and Mechanics*, *25*(1), Article e202400158. https://doi.org/10.1002/pamm.202400158
10. Guo, Z., Zhang, Y., Sheng, M., Liu, L., & Li, Y. (2025). Vibration characteristics of a beam with elastic time-varying stiffness boundaries. *Applied Sciences*, *15*(21), Article 11365. https://doi.org/10.3390/app152111365
11. Haghdoust, P., Lo Conte, A., Cinquemani, S., & Lecis, N. (2018). A numerical method to model non-linear damping behaviour of martensitic shape memory alloys. *Materials*, *11*(11), Article 2178. https://doi.org/10.3390/ma11112178

12. Han, S.L., & Kinoshita, T. (2012). Nonlinear damping identification in nonlinear dynamic system based on stochastic inverse approach. *Mathematical Problems in Engineering*, *2012*(1), 1–20, Article 574291. https://doi.org/10.1155/2012/574291
13. Li, C., Hao, J., Liu, H., Hua, C., & Yao, Z. (2024). Nonlinear parametric vibration and stability analysis of worm drive system with time-varying meshing stiffness and backlash. *Journal of Sound and Vibration*, *575*, Article 118264. https://doi.org/10.1016/j.jsv.2024.118264
14. Lisitano, D., & Bonisoli, E. (2021). Direct identification of nonlinear damping: application to a magnetic damped system. *Mechanical Systems and Signal Processing*, *146*, Article 107038. https://doi.org/10.1016/j.ymssp.2020.107038
15. Lisitano, D., Bonisoli, E., & Mottershead, J.E. (2018). Experimental direct spatial damping identification by the Stabilised Layers Method. *Journal of Sound and Vibration*, *437*, 325–339. https://doi.org/10.1016/j.jsv.2018.08.055
16. Liu, Q., Wang, Y., Sun, P., & Wang, D. (2022). Comparative analysis of viscous damping model and hysteretic damping model. *Applied Sciences*, *12*(23), Article 12107. https://doi.org/10.3390/app122312107
17. Paz, M. (1991). Structural dynamics: Theory and computation (3rd ed.). Van Nostrand Reinhold.
18. Qu, C., Tu, G., Gao, F., Sun, L., Pan, S., & Chen, D. (2024). Review of bridge structure damping model and identification method. *Sustainability*, *16*(21), Article 9410. https://doi.org/10.3390/su16219410
19. Sofroniou, A., & Bishop, S. (2014). Dynamics of a parametrically excited system with two forcing terms. *Mathematics*, *2*(3), 172–195. https://doi.org/10.3390/math2030172
20. Wei, S., Chu, F.-L., Ding, H., & Chen, L.-Q. (2021). Dynamic analysis of uncertain spur gear systems. *Mechanical Systems and Signal Processing*, *150*, Article 107280. https://doi.org/10.1016/j.ymssp.2020.107280
21. Yousfi, N., Zghal, B., Akrout, A., Walha, L., & Haddar, M. (2018). Damping models identification of a spur gear pair. *Mechanism and Machine Theory*, *122*, 371–388. https://doi.org/10.1016/j.mechmachtheory.2018.01.002
22. Zahid, F.B., Ong, Z.C., & Khoo, S.Y. (2020). A review of operational modal analysis techniques for in-service modal identification. *Journal of the Brazilian Society of Mechanical Sciences and Engineering*, *42*(8), Article 398. https://doi.org/10.1007/s40430-020-02470-8

Manuscript received December 27, 2025; accepted for publication March 25, 2026;

JOURNAL OF THEORETICAL
AND APPLIED MECHANICS
64, 2, pp. 131–144, Warsaw 2026
https://doi.org/10.15632/jtam-pl/221438

DRIVING TORQUE FOR A STEER-BY-WIRE SYSTEM HAND WHEEL ACTUATOR BASED ON THE REFERENCE DRIVING TORQUE FROM AN ELECTRIC POWER STEERING SYSTEM

Marek Bogdan BRYKCZYŃSKI*, Andrzej HARLECKI

Faculty of Mechanical Engineering and Computer Science, University of Bielsko-Biała, Bielsko-Biała, Poland
*corresponding author, *marek.brykczynski@gmail.com*

This paper experimentally determines an electric motor driving torque for a steer-by-wire (SBW) system hand wheel actuator (HWA). An equivalent electric motor driving torque for an SBW system HWA is determined with an objective to mirror the steering wheel angular position trajectory of an electric power steering (EPS) system by iterative examination of steering wheel trajectories of the SBW system HWA obtained for a series of driving torques against those from a reference EPS. The objective function criteria are defined by a maximum value of a mean relative error of the steering wheel angular position.

Keywords: driving torque; electric power steering; hand wheel actuator; road wheel actuator; steer-by-wire.

Nomenclature

Constant parameters

c_{em}, $c_{em'}$, $c_{em''}$ – viscous damping coefficient of the EPS motor, HWA motor, and RWA motor $[\mathrm{Nm} \cdot \mathrm{s}]$,
c_{ms}, $c_{ms'}$, $c_{ms''}$ – viscous damping coefficient of the electric motor shaft and worm engagement for: EPS system, HWA and RWA $[\mathrm{Nm} \cdot \mathrm{s}]$,
$c_r, c_{r''}$ – damping coefficient of the steering rack for EPS and RWA [Ns/m],
c_{sw}, $c_{sw'}$ – viscous damping coefficient of the EPS steering wheel and HWA steering wheel [Nms],
k_{ms}, $k_{ms'}$, $k_{ms''}$ – stiffness coefficient of the electric motor shaft engagements with a worm gear [Nm/rad],
k_r, $k_{r''}$ – stiffness coefficient of the steering rack for EPS and RWA [N/m],
k_{tb}, $k_{tb'}$ – stiffness coefficient of the torsion bars of the EPS and HWA [Nm/rad],
m_r, $m_{r''}$ – mass of the steering rack of the EPS and RWA [kg],
m_{wg}, m_{ww} – mass of the worm and worm wheel [kg],
r_p – radius of the pinion transmitting power to the rack [m],
C_f – C-factor – coefficient describing the linear displacement of the rack relative to the angular displacement of the pinion [mm/rad],
J_{em}, $J_{em'}$, $J_{em''}$ – moments of inertia of electric motors for: EPS, HWA, and RWA $[\mathrm{kg} \cdot \mathrm{m}^2]$,
J_{sw}, $J_{sw'}$ – moments of inertia of the EPS steering wheel and HWA steering wheel $[\mathrm{kg} \cdot \mathrm{m}^2]$,
J_{wg}, $J_{wg'}$, $J_{wg''}$ – symbols of the moment of inertia of the worm gear in: EPS, HWA, and RWA $[\mathrm{kg} \cdot \mathrm{m}^2]$,
J_{ww}, $J_{ww'}$, $J_{ww''}$ – symbols of the moment of inertia of the column and worm wheel assembly in: EPS, HWA, and RWA $[\mathrm{kg} \cdot \mathrm{m}^2]$,
$T_{\max} = 4.5$ – value of the maximum driving torque on the electric motor shaft [Nm] (Nidec Corporation, n.d.),
$\tau = 125$ – duration of the pulse shaped driving torque excitation [ms],
τ_{HWA} – time constant of the analyzed HWA model for the transfer function $\theta_{sw'} = \theta_{sw'}(T_{em'})$.

Input signals:

F_r – a value of rack force interacting on tie rods [N],
T_{em}, $T_{em'}$, $T_{em''}$ – values of driving torques generated by the EPS motor, HWA motor, and RWA motor [Nm],
T^a_{em} – a value of a reference driving torque from the EPS system [Nm],

$T^{b}_{em'}(j)$ – a value of a j-index driving torque for the HWA subsystem [Nm],
T_{dr} – a value of a driver's torque (external torque on the steering wheel) [Nm].

Variables:

θ_{em}, $\theta_{em'}$, $\theta_{em''}$ – angular displacements of the electric motor shaft for: EPS, HWA, and RWA [rad],
θ_{sw}, $\theta_{sw'}$ – sequentially angular displacements of the steering wheel for EPS and HWA [rad],
θ_{wg}, $\theta_{wg'}$, $\theta_{wg''}$ – sequentially worm gear angular displacements of the EPS, HWA, and RWA [rad],
θ_{ww}, $\theta_{ww'}$, $\theta_{ww''}$ – sequentially worm wheel angular displacements of the EPS, HWA, and RWA [rad],
χ_r, $\chi_{r''}$ – linear displacement of the steering rack for EPS and RWA [m],
$T_{cww} = T_{cww}(\theta_{wg}, \theta_{ww})$, $T_{cwg} = T_{cwg}(\theta_{wg}, \theta_{ww}), T_{cww'}, T_{cwg'}, T_{cww''}, T_{cwg''}$
– the reaction torques of the worm wheel and the worm gear in a worm drive [Nm].

1. Introduction

The steering system is responsible for positioning the vehicle's front (steered) wheels at the correct angle and, consequently, for controlling the desired direction of driving (steering). It "transmits" commands from the driver to steering knuckles, and simultaneously, in the opposite direction, "transmits" information to the driver about the vehicle current position on the road, also "allowing" the driver to sense the torque (torque of resistance) exerted on the steering wheel by the steering system, which is the result of the road's resistance forces acting on the front wheels. The coming years are expected to see a radical shift in the way automotive steering systems operate. It is predicted that the conventional electric power steering (EPS) systems currently used in (passenger) vehicles, in which the steering wheel is mechanically connected to the steering knuckles via the steering column, will in the future be replaced by steer-by-wire (SBW) systems. In these systems, the steering wheel and steering knuckles are connected solely via an electrical interface (an electrical communication bus), eliminating the mechanical connection.

The aim of the research described in this article is to determine the electric motor driving torque for the SBW system hand wheel actuator (HWA) subsystem, based on the steering wheel angle trajectory from a reference EPS system. As part of the study, the authors implemented a mathematical model of the EPS system and developed a mathematical model for the SBW system. The main focus of this work has been on the HWA subsystem, as both systems are coupled with the steering wheel. The SBW system road wheel actuator (RWA) subsystem is presented for reference to indicate the complete mechanical SBW system model. In the last stage of the study, the authors formulate a functional relation for an electric motor driving torque for the HWA dependent on the reference torque from the EPS system. The resultant function to derive the driving torque from the reference torque is formed with the objective to enable its implementation in the electronic control unit (ECU) of the SBW system, which is a real-time embedded microprocessor system. Consequently, a driver holding the steering wheel of a car equipped with this system will experience steering resistance comparable to an EPS system, resulting from the forces exerted by the road surface on the front wheels. It is worth noting that the EPS system has a significant limitation: the steering ratio between the steering wheel and the steering knuckles remains constant. This limitation is eliminated by the SBW system, which varies the ratio, thus enabling faster turning maneuvers. This, in turn, can significantly aid the driver while parking, as it will require fewer steering wheel turns than with a conventional EPS system.

After the introduction, the authors review available literature, starting with EPS systems, then followed by SBW systems. In the next step, the mathematical models of the EPS system and SBW system are presented and followed by the model comparison with the indication of key mechanical differences. Subsequently, the authors present the objective, methodology and results of their research. Finally, conclusions are drawn, indicating a direction for further research.

2. Literature review

The first scientific paper introducing an EPS system in (passenger) vehicles was published by Shimizu and Kawai (1991), where the authors presented the EPS system concept along with basic research on such a solution and its impact on reducing fuel consumption by 5.5 % compared to an electrohydraulic power steering system. Badawy *et al.* (1999) devised a modeling strategy for the EPS system and its transformation into a simplified model aimed at providing basic criteria for automatic steering systems. Canudas-de-Wit *et al.* (2005) focused on a review of automatic steering techniques to improve driving comfort while ensuring satisfactory functional safety for EPS systems. Research results by Pfeffer *et al.* (2008) described the effect of changes in the main parameters of the EPS system on steering torque, steering feel, and vehicle understeer. A model for an EPS system that integrates a control algorithm for basic assistance functionality, damping, steering return, and inertia compensation was proposed by Hu *et al.* (2008). Chen *et al.* (2011) presented a model of the EPS system and a method for developing a boost curve incorporated into the power steering characteristics to improve the mobility and stability of a steering system equipped with EPS. In their research, Ciarla *et al.* (2012) conducted a study of amplification criteria in boost curves, including steering wheel jerk and friction phenomena in the EPS system. Tamura *et al.* (2013) proposed a model incorporating the LuGre friction model for a column-type EPS system to analyze its performance under static and dynamic operating conditions. A method for active friction compensation in a column-type EPS system was presented by Wilhelm *et al.* (2016). In this study, a model of a column EPS system was proposed that takes into account the influence of slip and pressure on friction forces. Mirmohammad Sadeghi *et al.* (2017) established a procedure for determining friction forces for a column-type EPS system. Kuranowski (2019) published a dynamic model of the EPS system along with the results of its correlation with the tested real system, which demonstrated good model correlation with the real system. Manca *et al.* (2021) conducted research to estimate the performance of the EPS system for an autonomous, fully electric, four-wheel drive racing car participating in the Formula Student competition. Jang *et al.* (2022) proposed a method for modeling the torque from the road forces acting on the EPS system. Haas *et al.* (2023) developed a method for objectively evaluating feedback from a steering system equipped with an EPS system to the driver, which affects functional safety. Guan *et al.* (2024) formulated a closed-loop automatic control strategy for the EPS system, oriented towards steering wheel feel. Nguyen (2025) conducted a review of the scientific literature, classifying and analyzing various types of characteristics of EPS system assistance curves.

SBW systems are an evolution of EPS-based vehicle control. SBW technology is part of the X-By-Wire (XBW) family of technical solutions, of which the first production-scale implementation started with the Fly-By-Wire system in the F-16 Fighting Falcon military aircraft in 1973. In 1988, Fly-By-Wire technology was implemented in the Airbus A320 commercial passenger aircraft, which entered service with Air France. The first example of a car without a conventional mechanical coupling between the steering wheel and the steering rack was the Saab Prometheus concept car, presented in 1992. The vehicle was controlled using a joystick. Due to the difficulties of driving, the concept was not further developed. In 1996, Mercedes-Benz introduced the Mercedes-Benz F200 Imagination in Paris, in which the vehicle control system was implemented using two joysticks. The first scientific publications on SBW systems in the automotive industry date back to 1999, when Führer and Schedl (1999) presented research results demonstrating enormous potential for increasing passive and active functional safety in motor vehicles. Dilger *et al.* (1999) obtained a patent in the United States for a technical solution for the steering wheel control (steer-by-wire) steering system. Feick *et al.* (2000) published research results on a redundant steering wheel control (steer-by-wire) system providing force feedback to the driver on the vehicle's interaction with the road while driving. Dominke *et al.* (2002) published a patent proposing a strategy for increasing the level of functional safety in the steering wheel control (steer-by-wire) system through the use of auxiliary diagnostics of key signals. In the following years, further patents were published on various technical solutions for the HWA subsystem by Magnus *et al.* (2002) and Menjak *et al.* (2004). Yih and Gerdes (2004) published research conducted on a vehicle with an SBW system, which included an estimation of its side slip angle using information about the steering torque. Li and He (2005) proposed a bond graph model of the SBW system and conducted simulations of the dynamic behavior of the system in terms of the vehicle's maneuverability and steering feel. Yih (2005) presented doctoral thesis research on the impact of the SBW system on interaction with the car and on functional safety. Kazemi and Mousavinejad (2011) devised a new method of modeling the SBW system by applying the bond graph theory. Han *et al.* (2014) developed a method for designing the torque ratio based on the characteristics of the torque on the steering wheel in the SBW system. Tavoosi *et al.* (2014) presented a control algorithm aimed at improving the controllability of a car with an SBW system. In their work, they used a four-degree-of-freedom model and tested it in a hardware in the loop (HIL) environment. Polmans (2016) published a patent introducing a technical solution for the SBW system in which each front wheel had a separate RWA positioning system. Eickholt *et al.* (2019) published a patent presenting the mechanical assembly of the RWA subsystem components. Yin *et al.* (2024) formulated a control algorithm for the SBW system using a two-layer closed-loop model. The study proposed a strategy for observing the difference in the steering angle of the wheels in order to achieve a given steering angle. Perdana *et al.* (2025) conducted studies on various control strategies for SBW systems, assessing their impact on individual goals set for automatic control algorithms, such as: accuracy of obtained output values, operating range, feedback from the control system, and error detection.

The analyzed literature addresses either EPS or SBW systems separately, investigating their modeling, advanced control algorithms, and interaction with the vehicle. The present study focuses on providing methodology for determining the driving torque of the electric motor in the hand wheel actuator (HWA) of a steer-by-wire (SBW) system, using the driving torque characteristics of an electronic motor employed in a conventional electric power steering (EPS) system as the reference basis. The research aims to reproduce the steering wheel dynamics of the conventional EPS system, thereby ensuring that the driver experiences a comparable steering sensation.

3. Mathematical models

3.1. Conventional EPS system

The primary part of the column EPS system in Fig. 1 is the column (1), which is connected at the top to the steering wheel via a torsion bar (2). The lower end of the column is connected via a universal joint (3) to the upper end of the intermediate shaft (4). The lower end of this shaft is connected by means of another universal joint (3) with the upper end of the output shaft (5), which, at its lower end, has a pinion (6), cooperating with a toothed bar (7). The column-type

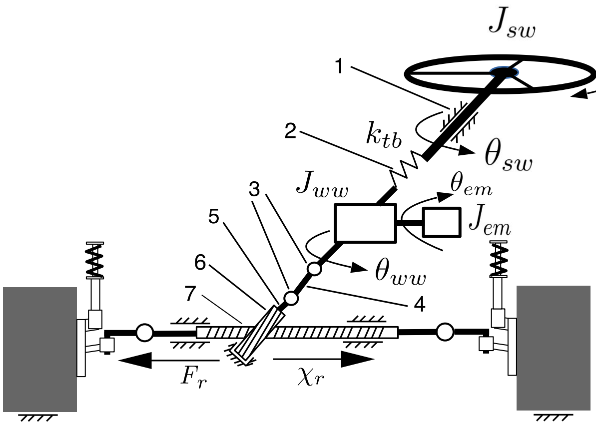

Fig. 1. Conventional EPS system with a column.

EPS system can be represented by the following equations of motion as shown by Hu *et al.* (2008) and later Tamura *et al.* (2013):

$$J_{sw}\ddot{\theta}_{sw} = -k_{tb}(\theta_{sw} - \theta_{ww}) - c_{sw}\dot{\theta}_{sw} + T_{dr}, \tag{3.1}$$

$$J_{ww}\ddot{\theta}_{ww} = k_{tb}(\theta_{sw} - \theta_{ww}) - r_p C_f k_r \left(\theta_{ww} - \frac{\chi_r}{C_f}\right) - c_{ww}\dot{\theta}_{ww} + T_{cww}, \tag{3.2}$$

$$J_{wg}\ddot{\theta}_{wg} = k_{ms}(\theta_{em} - \theta_{wg}) + c_{ms}(\dot{\theta}_{em} - \dot{\theta}_{wg}) + T_{cwg}, \tag{3.3}$$

$$J_{em}\ddot{\theta}_{em} = T_{em} - k_{ms}(\theta_{em} - \theta_{wg}) - c_{ms}(\dot{\theta}_{em} - \dot{\theta}_{wg}) - c_{em}\dot{\theta}_{em}, \tag{3.4}$$

$$m_r\ddot{\chi}_r = k_r(C_f\theta_{ww} - \chi_r) - c_r\dot{\chi}_r - F_r. \tag{3.5}$$

3.2. SBW steering system

The SBW steering system shown in Fig. 2 consists of two subsystems: the HWA and the RWA. The HWA steering subsystem is coupled to the steering wheel. Its main function, as that of the EPS system, is to "read" the driver's commands regarding the desired vehicle direction and, conversely, to "transmit" information to the driver about the current position of the front wheels. Both systems simultaneously "allow" the driver to sense the torque exerted on the steering wheel by the steering system, which is the result of the resistance forces acting on the front wheels from the road. The RWA vehicle wheels positioning subsystem is coupled to the front wheels via a rack and a pinion. The front wheel control unit $\mathrm{ECU_{RWA}}$ adjusts the wheels so that the vehicle can move in the direction specified by the driver. The RWA electronic control unit $\mathrm{ECU_{RWA}}$ microprocessor receives the information (command) about the desired steering direction digitally via a serial communication bus from the $\mathrm{ECU_{HWA}}$ control unit's microprocessor. The coupling digital communication bus between the HWA and the RWA of the SBW system depends on the actual design and can be realized by CAN 2.0, CAN FD, FlexRay or Automotive Ethernet protocols. The mechanical components of an SBW steering system (communication bus-coupled vehicle control system) can be represented by the following equations of motion as published by Han *et al.* (2014) with additional considerations as presented by Tamura *et al.* (2013) and Wilhelm *et al.* (2016).

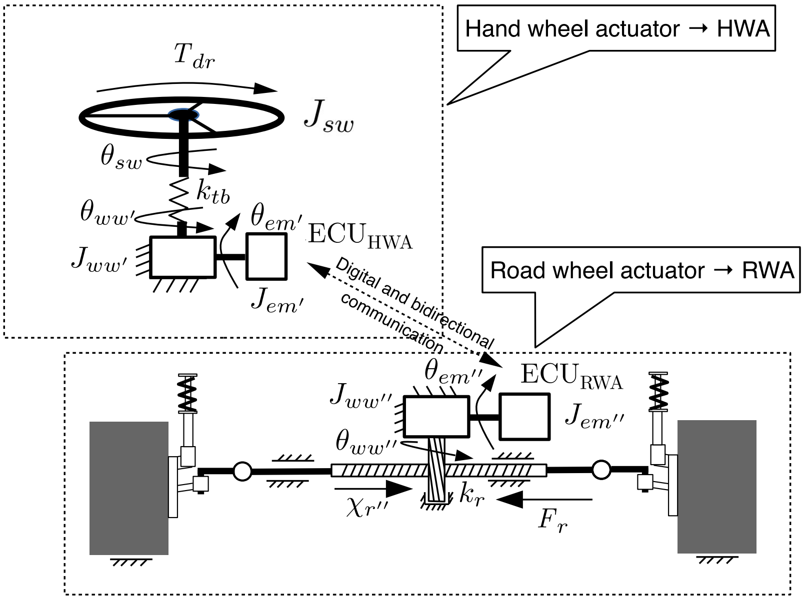

Fig. 2. SBW steering system.

HWA subsystem:

$$J_{sw'}\ddot{\theta}_{sw} = -k_{tb'}(\theta_{sw'} - \theta_{ww'}) - c_{sw'}\dot{\theta}_{sw'} + T_{dr}, \tag{3.6}$$

$$J_{ww'}\ddot{\theta}_{ww'} = k_{tb'}(\theta_{sw'} - \theta_{ww'}) - c_{ww'}\dot{\theta}_{ww'} + T_{cww'}, \tag{3.7}$$

$$J_{wg'}\ddot{\theta}_{wg'} = k_{ms'}(\theta_{em'} - \theta_{wg'}) + c_{ms'}(\dot{\theta}_{em'} - \dot{\theta}_{wg'}) + T_{cwg'}, \tag{3.8}$$

$$J_{em'}\ddot{\theta}_{em'} = T_{em'} - k_{ms'}(\theta_{em'} - \theta_{wg'}) - c_{ms'}(\dot{\theta}_{em'} - \dot{\theta}_{wg'}) - c_{em'}\dot{\theta}_{em'}. \tag{3.9}$$

RWA subsystem:

$$J_{ww''}\ddot{\theta}_{ww''} = -r_p C_f k_{r''}\left(\theta_{ww''} - \frac{\chi_{r''}}{C_f}\right) - c_{ww''}\dot{\theta}_{ww''} + T_{cww''}, \tag{3.10}$$

$$J_{wg''}\ddot{\theta}_{wg''} = k_{ms''}(\theta_{em'} - \theta_{wg''}) + c_{ms''}(\dot{\theta}_{em'} - \dot{\theta}_{wg''}) + T_{cwg''}, \tag{3.11}$$

$$J_{em''}\ddot{\theta}_{em''} = T_{em''} - k_{ms''}(\theta_{em'} - \theta_{wg''}) - c_{ms''}(\dot{\theta}_{em'} - \dot{\theta}_{wg''}) - c_{em''}\dot{\theta}_{em''}, \tag{3.12}$$

$$m_{r''}\ddot{\chi}_{r''} = k_{r''}(C_f\theta_{ww''} - \chi_{r''}) - c_{r''}\dot{\chi}_{r''} - F_r. \tag{3.13}$$

The set of the RWA subsystem motion Eqs. (3.10)–(3.13) are presented for the SBW steering system model completeness. Besides Eq. (3.13), which is used in the comparison of the EPS and SBW system models, the corresponding equations are presented for reference.

3.3. Worm drive model, reaction torques $T_{cww} = T_{cww}(\theta_{wg}, \theta_{ww})$ and $T_{cwg} = T_{cwg}(\theta_{wg}, \theta_{ww})$

The worm drive contact model was published by Dohring *et al.* (1993). The reaction forces and reaction torques in the left-handed worm drive for the EPS system and the HWA subsystem were considered using the contact model shown in Fig. 3 published in (Tamura *et al.*, 2013) and further developed by Wilhelm *et al.* (2016). The stiffness of the contact points 1 and 2 of the worm and the worm wheel teeth is k_c. The equations of motion of the worm and the worm wheel about their respective axes of motion: x for the worm and y for the worm wheel, are presented in Fig. 3:

$$m_{wg}\ddot{x} = F^x_{cwg} = N_{2,wg}\sin\gamma\cos\beta - F_{f2,wg}\cos\gamma - N_{1,wg}\sin\gamma\cos\beta - F_{f1,wg}\cos\gamma, \tag{3.14}$$

$$m_{ww}\ddot{y} = F^y_{cww} = -N_{2,ww}\cos\gamma\cos\beta - F_{f2,ww}\sin\gamma + N_{1,ww}\cos\gamma\cos\beta - F_{f1,ww}\sin\gamma. \tag{3.15}$$

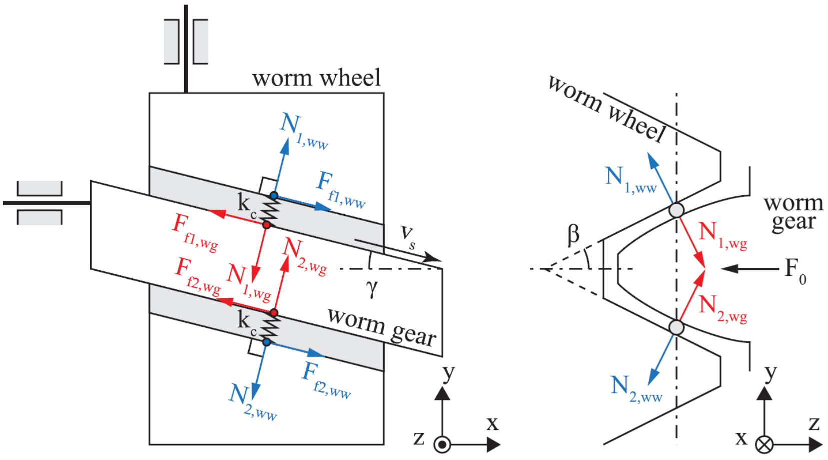

Fig. 3. Worm gear and worm wheel contact model (Wilhelm *et al.*, 2016).[1]

---

[1] Reprinted with permission from Wilhelm, F., Tamura, T., Fuchs, R., & Müllhaupt, P. (2016). Friction compensation control for power steering. *IEEE Transactions on Control Systems Technology*, © 2016 IEEE.

As shown in Fig. 3, the worm teeth are pressed against the worm wheel teeth by an initial pressure force F_0. As a result of the initial load, the contact points are precompressed by a distance h_0, which is described by Eq. (3.16):

$$h_0 = \frac{F_0}{2k_c \sin\beta}. \tag{3.16}$$

During motion, the elastic connection at the interaction points 1 and 2 of the worm gear and the worm wheel will undergo compression and decompression by a distance dh, which is described by Eq. (3.17). Compression by a distance dh of the elastic connection at contact 1 is equivalent to decompression at point 2, and vice versa. This dependence is included in the notation in the form of contact and normal forces presented in Eqs. (3.22) and (3.23) as a function of displacement dh where $\Delta\theta_{wg} = \Delta\theta_{wg}(t+\Delta t) - \theta_{wg}(t)$ and $\Delta\theta_{ww} = \Delta\theta_{ww}(t+\Delta t) - \theta_{ww}(t)$:

$$dh = r_{wg}\Delta\theta_{wg}\sin\gamma - r_{ww}\Delta\theta_{ww}\cos\gamma. \tag{3.17}$$

Normal forces in contact points:

$$N_{2,ww} = N_{2,wg} = k_c(\max(h_0 - dh, 0)), \tag{3.18}$$

$$N_{1,ww} = N_{1,wg} = k_c(\max(h_0 + dh, 0)). \tag{3.19}$$

Friction forces, where μ is the kinetic friction coefficient:

$$\operatorname{sgn} v_{wg}\mu N_{2,ww} = F_{f2,ww} = F_{f2,wg}, \tag{3.20}$$

$$\operatorname{sgn} v_{wg}\mu N_{1,ww} = F_{f1,ww} = F_{f1,wg}. \tag{3.21}$$

Notation in the form of contact and normal forces as a function of displacement dh:

$$F_C(dh) = N_{1,ww} - N_{2,ww} = N_{1,wg} - N_{2,wg}, \tag{3.22}$$

$$F_N(dh) = N_{1,ww} + N_{2,ww} = N_{1,wg} + N_{2,wg}. \tag{3.23}$$

The equations of motion (3.14) and (3.15), after taking into account Eqs. (3.18)–(3.21), can be written using the contact and normal force representation as functions of dh, as presented by Wilhelm *et al.* (2016):

$$F^x_{cwg} = -F_C \sin\gamma\cos\beta - \operatorname{sgn} v_{wg}\mu F_N \cos\gamma, \tag{3.24}$$

$$F^y_{cww} = F_C \cos\gamma\cos\beta - \operatorname{sgn} v_{wg}\mu F_N \sin\gamma. \tag{3.25}$$

The kinetic friction coefficient μ in the EPS and SBW systems uses the model proposed by Rooney and Deravi (1982), in which the kinetic friction coefficient μ'_k is modeled by a hyperbolic tangent:

$$\mu'_k = \mu_{k_{\max}} \tanh C|\dot{x}|. \tag{3.26}$$

The meaning of the symbols in Eq. (3.26) is as follows: μ'_k is the equivalent of the kinetic friction coefficient, $\mu_{k_{\max}}$ is the maximum kinetic friction coefficient, $\dot{x}$ is the sliding velocity, C is a constant. The reaction torques T_{cwg} and T_{cww}, as published by Wilhelm *et al.* (2016), are defined by equations:

$$T_{cwg} = r_{wg}F^x_{cwg}, \tag{3.27}$$

$$T_{cww} = r_{ww}F^y_{cww}. \tag{3.28}$$

3.4. Comparison of the EPS system and the HWA subsystem

The conventional EPS system model shown in Fig. 1 differs from the communication bus-coupled SBW system model shown in Fig. 2 by the existence of a mechanical connection between the steering wheel and the road wheels. In mathematical models, this difference is represented by the expression $r_p C_f k_r(\theta_{ww} - \frac{\chi_r}{C_f})$ in Eq. (3.2). However, this component does not exist in the SBW system model. Equation (3.7) describing the HWA subsystem does not have this expression since there is no mechanical linkage between road wheels and the steering wheel. Equation (3.7) is equivalent to Eq. (3.2) from the EPS system model. Similarly, Eq. (3.13), which describes the RWA subsystem, is equivalent to Eq. (3.5) from the EPS system model. This element of the model constitutes the mechanical coupling between the steering rods and the steering wheel. The lack of direct impact of the force in the rods F_r on the steering wheel is ensured in the SBW steering system, which provides this information digitally via a communication bus, in order to generate feedback torque on the steering wheel for the driver. The models differ in the number of degrees of freedom. In total, EPS has five, while SBW has eight. Additionally, they partially differ in the scope of the functions they perform in the automotive vehicle. The most important functionality of sensing the driver's intentions regarding the vehicle's driving direction is exactly the same in the EPS and the HWA systems. In the EPS system, the desired steering angle is transmitted via a mechanical linkage. In the HWA subsystem of the SBW system, information about the desired steering angle is transmitted digitally by its ECU microprocessor via a communication bus to the microprocessor of the RWA subsystem ECU in the SBW system. An example of a functional difference between the EPS system and the HWA subsystem is the assistance function, which helps overcome resistance. This function is present in the EPS system, resulting, among other things, from the direct mechanical connection between the steering wheel and the road via tires, linkages, the steering rack, and other connecting elements. The HWA subsystem does not have a direct connection to the road; therefore, the resistance felt on the steering wheel in the EPS system does not occur in the HWA subsystem. The HWA subsystem generates a resistance torque for the driver, stiffening the steering wheel so that the driver can feel the steering system interacting with the road and the vehicle's behavior.

4. An experimental determination of the equivalent driving torque

An experiment to determine the equivalent electric motor driving torque for the HWA is divided into two stages: a and b. During stage a of the experiment, the angular displacements of the joint positions in the reference model (EPS system) are determined at a given electric motor driving torque $T^a_{em}(t)$. Stage b of the experiment uses the iterative execution of the multiple fourth-order Runge–Kutta method (RK4) integrations to find whether any of the results satisfies the given criteria, i.e., Eq. (4.1). Stage b of the experiment determines the family of driving torques $[T^b_{em'}]$, which is represented by a matrix with the number of rows equal to the number of time samples i and the number of columns equal to the number of evaluated driving torque amplitudes j. The matrix of the driving torque family is associated with the matrix of steering wheel angular displacement trajectories $[\theta^b_{sw'}(t)]$, where each row corresponds to a time sample and each column corresponds to an experimental result obtained for a particular driving torque from the family $T^b_{em'}(t)(j)$, i.e., $[\theta^b_{sw'}] = [\theta^b_{sw'}]([T^b_{em'}])$. The final driving torque is the one from the family $[T^b_{em'}]$ for which the associated angular displacement trajectory at the time of the steady state (time interval equal to five time constants) meets the given error criteria or yields a better result as per Eq. (4.1). For each experiment, the rack force $F_r = 0\,[\mathrm{N}]$ and the driver's torque $T_{dr} = 0\,[\mathrm{Nm}]$ will not affect the EPS system and the HWA subsystem.

$$Q(x) = \delta_{\theta_{sw\mathrm{Av}}} = f(T_{em'_{\mathrm{Amp}}}) \to \min \leq 5\,\%, \tag{4.1}$$

$$\delta_i = \left|\frac{\theta^b_{sw'}(i) - \theta^a_{sw}(i)}{\theta^a_{sw}(i)}\right| \cdot 100\,\%, \tag{4.2}$$

$$\delta = \frac{1}{n}\sum_{0}^{n} \delta_i, \tag{4.3}$$

$$\delta_{\theta_{sw\mathrm{Av}}} = \frac{1}{n}\sum_{0}^{n} \left|\frac{\theta^b_{sw'}(i) - \theta^a_{sw}(i)}{\theta^a_{sw}(i)}\right| \cdot 100\,\%. \tag{4.4}$$

The formulas are for the relative momentary error – Eq. (4.2), the general representation of the average relative error – Eq. (4.3), and the mean relative error of the angular position θ^b_{sw} – Eq. (4.4). In this study, the reference model is the EPS system. The driving torque T_{em} available on the electric motor's shaft is used as an input signal during simulations. The examined systems are excited by driving torques: T^a_{em} for the EPS system and $[T^b_{em'}]$ for the HWA. All driving torques are shaped as a pulse during analysis and their general form is defined by Eq. (4.5). The excitation driving torques T^a_{em} and $[T^b_{em'}]$ are defined as pulses lasting $\tau = 125\,\mathrm{ms}$. The input signals $T^a_{em}(t)$, $[T^b_{em'}(t)]$ are used to excite the examined systems into accelerated motion while driving and to allow the examined systems to settle on the final position in the steady states. During the simulation, a special case is examined in which all corresponding parameters are assumed to be the same for the EPS system and the HWA subsystem, i.e., $J_{em'} = J_{em}$, $J_{wg'} = J_{wg}$, $J_{ww'} = J_{ww}$, $J_{sw'} = J_{sw}$, $k_{ms'} = k_{ms}$, $k_{tb'} = k_{tb}$, $c_{em'} = c_{em}$, $c_{ms'} = c_{ms}$, $c_{sw'} = c_{sw}$. The individual transient driving torques $T^b_{em'}(t)(j)$ are described by Eq. (4.6), where j denotes the index of the element of the driving torque family $T^b_{em'}(t)$. During the experiment, the amplitude will belong to the interval $T^b_{em'}(t)(j) \in [0, T_{\max}]$:

$$T^a_{em}(t) = T_{\max} \cdot (1(t) - 1(t-\tau)), \tag{4.5}$$

$$T^b_{em'}(t)(j) = T^b_{\max'}(j) \cdot (1(t) - 1(t-\tau)). \tag{4.6}$$

The reference driving torque is defined by Eq. (4.5), where $\tau = 125\,\mathrm{ms}$. The target driving torques for the HWA subsystem of a family $[\theta^b_{sw'}(t)]$ are derived iteratively. Table 1 presents the selected driving torque amplitudes $T_{em'}(j)^b(t)$ and the results for the mean relative steering wheel angular position errors $\theta_{sw'}(j)^b(t)$.

Table 1. List of selected amplitudes of $T^b_{em'}(t)$
with their corresponding mean relative position errors $\theta^b_{sw'}(t)$.

Index	$T_{em'_{\mathrm{Amp}}}$	$\delta_{\theta_{sw\mathrm{Av}}}$
0	0	96.688
1	0.40704	96.688
2	0.42965	92.303
3	1.0176	69.422
4	1.5151	54.543
5	2.0126	39.854
6	2.5101	25.229
7	3.0075	10.648
8	**3.2769**	**4.568**
9	3.3026	4.605
10	3.505	6.718
11	4.0025	18.556
12	4.5	32.827

Figure 4a presents the reference driving torque for the EPS system $T^{a}_{em}(t)$ and selected driving torques for the family of driving torques for the HWA subsystem $[T^{b}_{em'}(t)]$, respectively indexed as: 0, 8, 11 from Table 1. The reference driving torque $T^{a}_{em}(t)$ is marked with a green line. The selected driving torques from the family $[T^{b}_{em}(t)]$ are marked as follows: $T^{b}_{em'}(t)(0) \rightarrow$ magenta line, $T^{b}_{em'}(t)(8) \rightarrow$ red line, $T^{b}_{em'}(t)(11) \rightarrow$ blue line. The driving torque $T^{b}_{em'}(t)(0)$ is deliberately equal to 0 because it verifies that the model of the system will not start motion unless it is externally driven. This is confirmed by ensuring that all of joint angular displacements: $\theta^{b}_{sw'}(t)(0)$, $\theta^{b}_{ww'}(t)(0)$, $\theta^{b}_{wg'}(t)(0)$, $\theta^{b}_{em'}(t)(0)$ are equal to 0. Figure 4b presents the reference angular position $\theta^{a}_{sw}(t) \rightarrow$ red line related to the reference driving torque $T^{a}_{em}(t)$ and the obtained angular positions: $\theta^{b}_{sw'}(t)(0) \rightarrow$ the magenta line, $\theta^{b}_{sw'}(t)(8) \rightarrow$ red line, $\theta^{b}_{sw'}(t)(11) \rightarrow$ blue line.

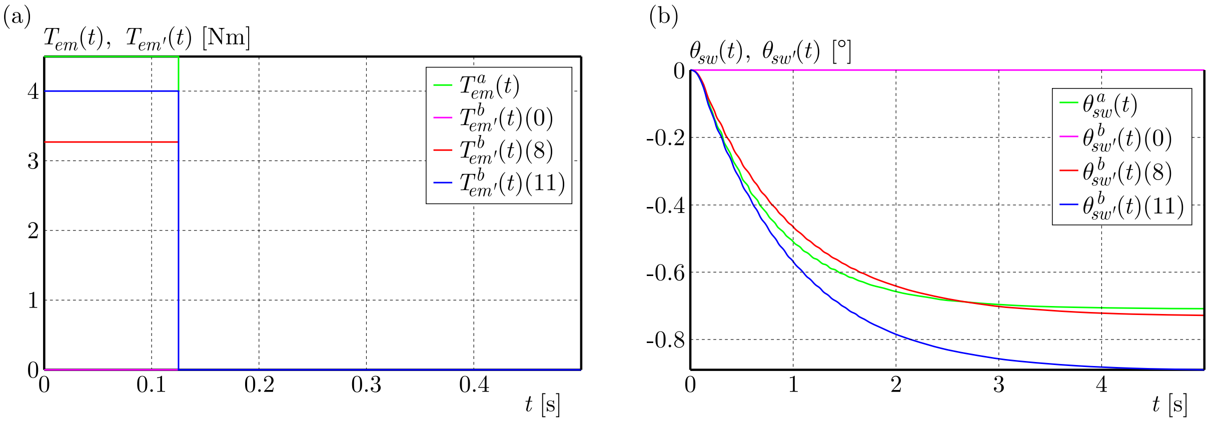

Fig. 4. (a) Driving torques $T_{em}(t)$, $T_{em'}(t)$; (b) angular displacements of the steering wheel $\theta_{sw}(t)$, $\theta_{sw'}(t)$ (normalized).

The indexes of the angular positions $0, 8, 11$ correspond to the driving torque amplitudes as shown in Table 1 and as they are presented in Fig. 4a. Table 1 presents the key results from hundreds of numerical calculations performed by the authors. The examined HWA subsystem model time constant for the steering wheel angular position as a function of the driving torque $\theta_{sw'} = \theta_{sw'}(T_{em'})$ is equal to $\tau_{\mathrm{HWA}} = 0.983\,[\mathrm{s}]$. The τ_{HWA} was determined from the measurements as a time when the HWA system achieves its steering wheel angular position $\theta^{b}_{sw'}(t)(8)$ equal to 62.31 % of the target position in the steady state $\theta^{b}_{sw'}(t = 5\tau_{\mathrm{HWA}})(8)$. The best results considering the steering wheel position in a steady state are obtained for $\theta^{b}_{sw'}(t)(8)$, which is affected by the mean relative error $\delta_{\theta_{sw\mathrm{Av}}}(8)$ at the level of 4.568 %, comparing to the reference angular position trace $\theta^{a}_{sw}(t)$. The index 0, by means of $\theta^{b}_{sw'}(t)(0)$, verifies the model by confirming that it is not in motion for a driving torque equal to $0 \rightarrow T^{b}_{em'}(t)(0)$. The $\theta^{b}_{sw'}(t)(12)$ which is related to the driving torque $T^{b}_{em'}(t)(12) = T^{a}_{em}(t)$ is affected by the mean relative error $\delta_{\theta_{sw\mathrm{Av}}}(12)$ at the level of 32.827 %. Figure 5 presents the momentary relative error of the steering wheel angular position $\delta\theta^{b}_{sw'}(t)(8)$ for the HWA subsystem which is obtained for $T^{b}_{em'}(t)(8)$ from Table 1. As a result of stages a and b, the driving torque amplitude for the HWA subsystem was obtained, which lies within the assumed permissible error of the objective function $Q(x)$ defined by Eq. (4.1). The smallest mean relative error $\delta_{\theta_{sw\mathrm{Av}_{\min}}} = 4.568\,\%$ was obtained for the driving torque amplitude $T_{em'_{\mathrm{Amp}}} = 3.2769\,\mathrm{Nm}$. The final driving torque will be denoted as $T^{c}_{em'}(t) = T^{b}_{em'}(t)(j = j_{\min})$:

$$T^{c}_{em'}(t) = T_{\max'} \cdot (1(t) - 1(t-\tau)), \tag{4.7}$$

$$T^{c}_{em'}(t) = 3.2769 \cdot (1(t) - 1(t-0.125)). \tag{4.8}$$

The work was focused on the strategy to determine a driving torque considering the trajectory in the time interval until the target steering wheel angular position is obtained, i.e., the

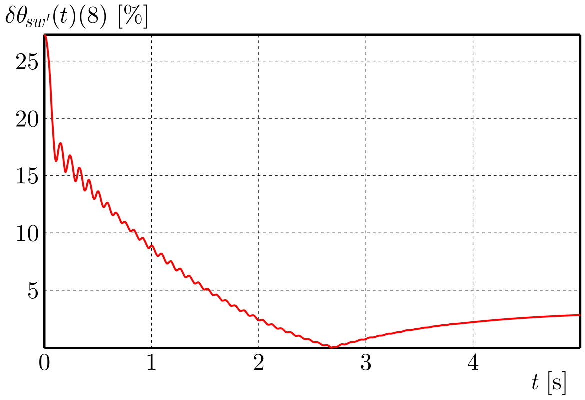

Fig. 5. Momentary relative error [%] of angular displacement for $\theta^{b}_{sw'}(t)(8)$ in the time interval until the steady state.

steady state is achieved. Figure 6 presents the trace of the momentary relative error for the angular position $\delta\theta^{b}_{sw'}(t)(8)$. When it comes to the time interval when the HWA is excited by the electric motor's driving torque, the mean momentary relative error $\delta\theta_{sw\mathrm{Av}}(8)_{t=125\,\mathrm{ms}} = 21.8\,\% \in [0\,\mathrm{ms}, 125\,\mathrm{ms}]$. Considering the $\theta^{b}_{sw'}(t)(8)$ trajectory in the excitation time interval $t_{\mathrm{exc}} \in [0\,\mathrm{ms}, 125\,\mathrm{ms}]$, in the transient state phase, the electric motor driving torque for the HWA direct scaling from the reference EPS requires a different strategy.

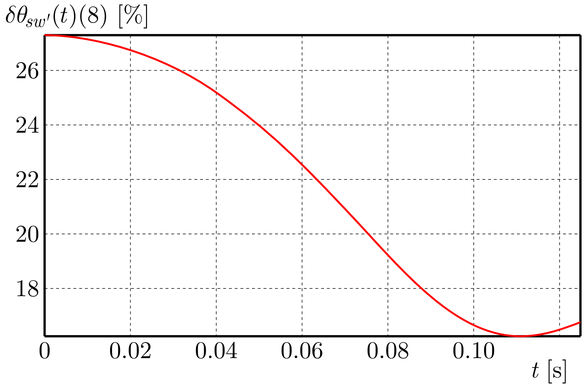

Fig. 6. Momentary relative error [%] of angular displacement for $\theta^{b}_{sw'}(t)(8)$ during the HWA excitation by its electric motor's driving torque $T^{b}_{em'}(t)(8)$.

5. Summary

The empirically obtained data allows the authors to formulate a coefficient which scales the amplitude of the driving torque from the EPS system to the HWA subsystem s_{EPS2HWA^*}, thus ensuring that the trajectory of the HWA steering wheel angular displacement falls within the range of the predefined mean relative error as per Eq. (4.4) in the time interval required to achieve the steady state, and fulfilling the criteria defined by Eq. (4.1):

$$s_{\mathrm{EPS2HWA}^*} = \frac{T_{em_{\mathrm{AmpHWA}}}}{T_{em_{\mathrm{AmpEPS}}}} = \frac{3.2769}{4.5} = 0.7282. \tag{5.1}$$

The scaling coefficient s_{EPS2HWA^*}, which is defined by Eq. (5.1), transforms the amplitude of a pulse shaped reference electric motor driving torque. The coefficient s_{EPS2HWA^*} allows a command to be scaled from a projected motor torque curve from the EPS system to a HWA subsystem. The linear scaling coefficient can be applied in microprocessor embedded systems in various automotive ECUs. Its impact on the computational capability and the microcontroller resources is low and can be performed in real time. Applying the scaling factor from Eq. (5.1) of the HWA subsystem electric motor driving torque can be defined by Eq. (5.2):

$$T_{em'}(t) = s_{\mathrm{EPS2HWA}^*} \cdot T_{em}(t). \tag{5.2}$$

The results were obtained for a specific case where all of the corresponding constant parameters of the EPS system and the HWA subsystem were assumed as equal (Subsection 3.4). Further research is focused on determining a scaling coefficient which is dependent on multiple parameter relations:

$$s_{\mathrm{EPS2HWA}} = s_{\mathrm{EPS2HWA}}\left(\frac{T_{em'}}{T_{em}}, \frac{J_{em'}}{J_{em}}, \frac{J_{wg'}}{J_{wg}}, \frac{J_{ww'}}{J_{ww}}, \frac{J_{sw'}}{J_{sw}}, \frac{k_{ms'}}{k_{ms}}, \frac{k_{tb'}}{k_{tb}}, \frac{c_{em'}}{c_{em}}, \frac{c_{ms'}}{c_{ms}}, \frac{c_{sw'}}{c_{sw}}\right). \tag{5.3}$$

Based on the analysis of the obtained traces, it is concluded that the proposed model of the HWA subsystem of the SBW system, in terms of shape, reflects the conventional EPS system steering wheel angular position trajectory with good approximation in the time interval ending in steady state. Additionally, limitations of the driving torque scaling strategy were observed during the system excitation interval, which constitutes a direction for further research.

References

1. Badawy, A., Zuraski, J., Bolourchi, F., & Chandy, A. (1999). Modeling and analysis of an electric power steering system. *SAE Technical Papers*. https://doi.org/10.4271/1999-01-0399
2. Canudas-de-Wit, C., Bechart, H., Claeys, X., Dolcini, P., & Martinez, J.-J. (2005). Fun-to-drive by feedback. *European Journal of Control*, *11*(4–5), 353–383. https://doi.org/10.1016/s0947-3580(05)71042-6
3. Chen, H., Yang, Y., & Zhang, R. (2011). Study on Electric Power Steering system based on ADAMS. *Procedia Engineering*, *15*, 474–478. https://doi.org/10.1016/j.proeng.2011.08.090
4. Ciarla, V., Cahouet, V., Canudas De Wit, C., & Quaine, F. (2012). Genesis of booster curves in Electric Power Assistance Steering systems. In *2012 15th International IEEE Conference on Intelligent Transportation Systems* (pp. 1345–1350). IEEE. https://doi.org/10.1109/ITSC.2012.6338807
5. Dilger, E., Ahner, P., Lohner, H., Dominke, P., Cao, C.-T., Nguyen, N.-T., Janetzke, H., Allgeier, T., Pfeiffer, W., Yuan, B., Muller, B., Ries-Mueller, K., Harter, W., Sauer, T., Hess, W., & Blessing, P. (2001). S*teer-by-wire steering system for motorized vehicles* (U.S. Patent No. 6219604B1). U.S. Patent and Trademark Office. http://www.google.com/patents/US6219604
6. Dohring, M.E., Lee, E., & Newman, W.S. (1993). A load-dependent transmission friction model: theory and experiments. In *[1993] Proceedings IEEE International Conference on Robotics and Automation*, Vol. 3 (pp. 430–436). IEEE. https://doi.org/10.1109/robot.1993.292210
7. Dominke, P., Cao, C.-T., Pfeiffer, W., Yuan, B., Leimbach, K.-D., Mueller, B., Harter, W., Blessing, P., Schuele, J., & Lohner, H. (2002). *Method for controlling a steer-by-wire system* (U.S. Patent No. 6871127B2). U.S. Patent and Trademark Office. https://patents.google.com/patent/US6871127B2/en?oq=US+6%2C871%2C127
8. Eickholt, M.A., Golda, F.N., Kern, P.E., Marr, J.L., Otto, J.M., & Stilwell, E.N. (2019). *Road wheel actuator assembly* (U.S. Patent No. 10322744B2). U.S. Patent and Trademark Office. http://www.google.com/patents/US10322744
9. Feick, S., Pandit, M., Zimmer, M., & Uhler, R. (2000). Steer-by-wire as a mechatronic implementation. *SAE Technical Papers*, *109*, 1152–1160. https://doi.org/10.4271/2000-01-0823
10. Führer, T., & Schedl, A. (1999). The steer-by-wire prototype implementation: Realizing time triggered system design, fail silence behavior and active replication with fault-tolerance support. *SAE Technical Papers*. https://doi.org/10.4271/1999-01-0400
11. Guan, X., Zhang, Y.N., Lu, P.P., Duan, C.G., & Zhan, J. (2024). The control strategy of the electric power steering system for steering feel control. *Proceedings of the Institution of Mechanical Engineers, Part D: Journal of Automobile Engineering*, *238*(2–3), 347–357. https://doi.org/10.1177/09544070221132131

12. Haas, A., Menze, G., Sieberg, P. M., & Schramm, D. (2023). An objective evaluation approach for safety-relevant steering feedback on a test bench. *Vehicles*, *5*(4), 1727–1742. https://doi.org/10.3390/vehicles5040094

13. Han, Y., He, L., Wang, X., & Zong, C. (2014). Research on torque ratio based on the steering wheel torque characteristic for steer-by-wire system. *Journal of Applied Mathematics*, *2014*(1), Article 929164. https://doi.org/10.1155/2014/929164

14. Hu, T.-H., Yeh, C.-J., Ho, S.-R., Hsu, T.-H., & Lin, M.-C. (2008). Design of control logic and compensation strategy for electric power steering systems. In *2008 IEEE Vehicle Power and Propulsion Conference (VPPC)*. IEEE. https://doi.org/10.1109/VPPC.2008.4677471

15. Jang, B., Lee, D., Kim, K., & Kim, K.-S. (2022). Road torque modeling for electric power steering systems. *International Journal of Automotive Technology*, *23*(3), 765–773. https://doi.org/10.1007/s12239-022-0068-0

16. Kazemi, R., & Mousavinejad, I. (2011). A Comprehensive model for developing of Steer-By-Wire System. *International Journal of Mechanical, Industrial and Aerospace Sciences*, *5*(8), 1688–1694. https://scholarly.org/pdf/display/a-comprehensive-model-for-developing-of-steer-by-wire-system

17. Kuranowski, A. (2019). Electrical power steering – modelling and bench testing. *Technical Transactions*, *8*(116), 143–158. https://doi.org/10.4467/2353737xct.19.085.10864

18. Li, Q., & He, R. (2005). Modeling and simulation study of the steer by wire system using bond graph. *2005 IEEE International Conference on Vehicular Electronics and Safety* (pp. 7–11). IEEE. https://doi.org/10.1109/ICVES.2005.1563604

19. Magnus, B.J., Augustine, M.J., & Cole, M.J. (2002). *Steer-by wire handwheel actuator* (U.S. Patent No. 0189888A1). U.S. Patent and Trademark Office. https://patents.google.com/patent/US20020189888A1/en

20. Manca, R., Circosta, S., Khan, I., Feraco, S., Luciani, S., Amati, N., Bonfitto, A., & Galluzzi, R. (2021). Performance assessment of an electric power steering system for driverless formula student vehicles. *Actuators*, *10*(7), Article 165. https://doi.org/10.3390/act10070165

21. Menjak, R., Haupt, J., Card, J.M., & Thomas, S.M. (2004). *Hand wheel actuator* (U.S. Patent No. 6799654B2). U.S. Patent and Trademark Office. http://www.google.com/patents/US6799654

22. Mirmohammad Sadeghi, S.H., Sesana, R., & Maffiodo, D. (2017). Friction calculation and simulation of column electric power steering system. *International Journal of Mechanical and Mechatronics Engineering*, *11*(1), 153–160. https://doi.org/10.5281/zenodo.1339980

23. Nguyen, T.A. (2025). Mathematical modeling and characteristics of automotive electric power steering systems: A state–of–the–art literature review. *Ain Shams Engineering Journal*, *16*(9), Article 103516. https://doi.org/10.1016/j.asej.2025.103516

24. Nidec Corporation, *Automotive EPS*. Retrieved February 7, 2025, from https://www.nidec.com/en/product/search/category/ B101/M102/S100/NCJ-Automotive-EPS-02/.

25. Perdana, M.A.P., Budiman, A.C., Ristiana, R., Muharam, A., Ismail, K., Kurnia, M.R., Amin, Huda, N., Kaleg, S., & Hapid, A. (2025). Control strategies for steer-by-wire systems: An overview. *Technologies*, *13*(1), Article 6. https://doi.org/10.3390/technologies13010006

26. Pfeffer, P.E., Harrer, M., & Johnston, D.N. (2008). Interaction of vehicle and steering system regarding on-centre handling. *Vehicle System Dynamics*, *46*(5), 413–428. https://doi.org/10.1080/00423110701416519

27. Polmans, K. (2016). *Steer-by-wire steering system with couplable single-wheel steering systems* (German Patent No. WO2017198549A1). German Trademark and Patent Office. https://patents.google.com/patent/WO2017198549A1/en

28. Rooney, G.T., & Deravi, P. (1982). Coulomb friction in mechanism sliding joints. *Mechanism and Machine Theory*, *17*(3), 207–211. https://doi.org/10.1016/0094-114X(82)90006-4

29. Shimizu, Y., & Kawai, T. (1991). Development of electric power steering. *SAE Technical Papers*. https://doi.org/10.4271/910014

30. Tamura, T., Maroonian, A., Higashi, M., & Fuchs, R. (2013). Modeling and simulation for dynamic analysis of column type electric power steering. *JTEKT Engineering Journal*, *1010*(1010E), 19–25. https://www.jtekt.co.jp/e/engineering-journal/assets/1010/1010e_05.pdf

31. Tavoosi, V., Kazemi, R., & Hosseini, S.M. (2014). Vehicle handling improvement with steer-by-wire system using hardware in the loop method. *Journal of Applied Research and Technology*, *12*(4), 769–781. https://doi.org/10.1016/S1665-6423(14)70093-8

32. Wilhelm, F., Tamura, T., Fuchs, R., & Müllhaupt, P. (2016). Friction compensation control for power steering. *IEEE Transactions on Control Systems Technology*, *24*(4), 1354–1367. https://doi.org/10.1109/TCST.2015.2483561

33. Yih, P. (2005). *Steer-by-wire: Implications for vehicle handling and safety* [doctoral dissertation, Stanford University]. Stanford University, Dynamic Design Lab. https://ddl.stanford.edu/publications/thesis/steer-wire-implications-vehicle-handling-and-safety

34. Yih, P., & Gerdes, J. (2004). Steer-by-wire for vehicle state estimation and control. *Proceedings of AVEC*, 785–790. http://www-cdr.stanford.edu/dynamic/bywire/avec2004_v2.pdf

35. Yin, H., Wang, Z., Liu, J., & Liu, P. (2024). Steer-by-wire control algorithm using a dual-layer closed-loop model. *Scientific Reports*, *14*, Article 28536. https://doi.org/10.1038/s41598-024-79703-6

Manuscript received October 25, 2025; accepted for publication May 4, 2026;

JOURNAL OF THEORETICAL
AND APPLIED MECHANICS
64, 2, pp. 145–163, Warsaw 2026
https://doi.org/10.15632/jtam-pl/221708

AN ADAPTIVE SEMI-EMPIRICAL FRAMEWORK FOR ROLLING RESISTANCE PREDICTION INCORPORATING TIRE MASS AND DYNAMIC GEOMETRIC PARAMETERS

Mohammad Sadegh NAEBI[1], Hamed RAEISIFARD[1]*, Nader MOHAMMADI[2]

[1] *Department of Mechanical Engineering, WT.C., Islamic Azad University, Tehran, Iran*
[2] *Department of Mechanical Engineering, Pa.C., Islamic Azad University, Parand, Tehran, Iran*
*corresponding author, *ha.raeisifard@iau.ac.ir*

Rolling resistance (RR) is a key factor affecting vehicle energy efficiency and fuel consumption, and it is strongly influenced by tire design parameters. In this study, the effects of tire mass and key geometric parameters, including dynamic sidewall, dynamic diameter, and seated width, on RR are systematically investigated through experimental measurements and analytical modeling. Unlike conventional studies that primarily focus on applied load, this work emphasizes the influence of the tire's intrinsic mass and incorporates multiple design parameters within a unified framework. To better represent tire behavior under rolling conditions, dynamic (functional) geometric parameters are used instead of nominal values. Based on experimental data obtained under controlled conditions in accordance with ISO 28580, individual relationships between each parameter and RR are established using curve-fitting techniques. A comprehensive model is then developed by combining these effects through different weighting approaches. In particular, a novel sliding normalization model (MSN) is proposed to adaptively determine variable weighting coefficients. Unlike constant and sigmoid-based methods, the MSN approach adjusts parameter weights based on their normalized positions within the dataset range, thereby improving flexibility and predictive performance. The proposed model is validated using 27 tire samples, including 21 test tires and 6 additional tires not used in model calibration. The results show that the MSN approach achieves a lower prediction error than conventional weighting methods. The model demonstrates strong predictive capability within the investigated parameter ranges. It should be noted that the proposed framework is semi-empirical and is developed under controlled testing conditions, with operational variables such as inflation pressure, temperature, and velocity kept constant. Therefore, the model's applicability beyond the studied domain requires further investigation. Nevertheless, the present study provides a practical, adaptable approach for analyzing the influence of tire design parameters on RR and lays a foundation for future model development.

Keywords: tire rolling resistance (RR); parameters affecting RR; comprehensive model for RR; RR test.

1. Introduction

Rolling resistance (RR) is a critical factor influencing vehicle energy efficiency, fuel consumption, and environmental impact. As regulations on emissions and energy performance become increasingly stringent, improving tire performance has become a key focus in both academic research and industrial development. RR is primarily associated with energy dissipation mechanisms within the tire structure, including hysteresis losses in the rubber and tire deformation during rolling.

Previous studies have extensively investigated the effects of operational parameters, such as vertical load, inflation pressure, temperature, and speed, on RR. In particular, the effect of applied load (vehicle weight) has been widely analyzed and incorporated into both experimental and analytical models. However, comparatively less attention has been given to the role of the tire's intrinsic properties, especially the influence of the tire's own mass and its interaction with geometric design parameters. The investigation of RR has been approached through experimental testing or finite element modeling (FEM). Experimental studies have provided direct measurements of rolling forces under varying loads, velocities, and material conditions. However, such methods are time-intensive and costly, as they require specialized testing drums and the fabrication of tire samples.

A fundamental understanding of RR is closely related to energy dissipation mechanisms within the tire structure. Walter and Conant (1974) demonstrated that RR primarily originates from hysteresis losses in the viscoelastic materials of the tire. During rolling, cyclic deformation of the tire leads to continuous energy dissipation, as part of the mechanical energy is converted into heat and cannot be fully recovered. Their work revealed that these energy losses depend not only on material properties but also on tire structural characteristics and the nature of deformation. This indicates that RR is inherently governed by both material behavior and tire design parameters.

Further studies have emphasized the role of tire design and material composition in RR. Martini (1983) demonstrated that tread compounding significantly affects energy losses, as modifications in rubber formulation can alter hysteresis behavior. However, improvements in RR are often accompanied by trade-offs with other performance characteristics, such as traction and wear resistance. This indicates that tire performance optimization is inherently a multi-parameter problem involving both material and structural design considerations.

In addition to material effects, the influence of design and construction parameters has been widely investigated. Walter (1983) analyzed the impact of several key design variables on RR and cornering force, showing that tire performance is strongly affected by the combined influence of multiple parameters. The study also demonstrates that improvements in one performance aspect may affect others, underscoring the multi-parameter, interdependent nature of tire design.

Recent studies have highlighted the importance of testing conditions in RR measurements. Ejsmont *et al.* (2025) investigated the influence of temperature on RR measurements and demonstrated that tire behavior is highly sensitive to thermal conditions. Due to viscoelastic effects, increasing temperature reduces material stiffness and hysteresis losses, thereby lowering RR. The study showed that RR values vary significantly during the heating phase and emphasized that accurate measurements must be performed under thermal equilibrium conditions. These findings highlight the critical role of temperature control and thermal history in obtaining reliable RR data. In addition, Ejsmont *et al.* (2024) compared different RR measurement methods and surface conditions, demonstrating that measured values vary significantly depending on testing approach and contact characteristics. The study showed that factors such as surface roughness and testing configuration influence tire deformation and energy dissipation, leading to discrepancies between laboratory and real-world results. These findings indicate that RR is not an intrinsic constant, but rather a system-dependent parameter influenced by measurement conditions and surface interactions.

More recent studies have adopted combined experimental and numerical approaches to analyze tire performance. Liang *et al.* (2020) evaluated RR and grip characteristics using both testing and simulation, and demonstrated that improvements in RR are often associated with reductions in grip performance. Their findings highlight the multi-objective nature of tire design, where performance optimization requires balancing competing criteria. Comprehensive reviews have further emphasized the multi-factor nature of RR.

Ydrefors *et al.* (2021) provided a comprehensive review demonstrating that RR is governed by complex interactions among material properties, tire design, and operating conditions. While hysteresis losses in viscoelastic materials are the primary source of energy dissipation, the study showed that factors such as temperature, load, inflation pressure, and speed significantly influence tire deformation behavior and energy losses. Their findings reveal that RR is inherently a multifactor, nonlinear phenomenon and cannot be accurately described by a single parameter.

Xu *et al.* (2025) demonstrated that advanced material engineering at the rubber-filler interface can significantly improve tire performance. By introducing chain difunctionalization in styrene-butadiene rubber via thiol-ene click reactions, the interfacial interaction with silica was substantially enhanced, leading to improved filler dispersion and a more stable rubber-filler network. This resulted in reduced hysteresis losses and a significant decrease in RR, while simultaneously improving wet grip and wear resistance. These results show that RR is not only governed by macroscopic design parameters but is also strongly influenced by molecular-level interfacial phenomena.

Pillai and Fielding–Russell (1992) introduced an energy-based framework for evaluating RR by defining a whole-tire hysteresis ratio. They developed a simple equation for tire RR, in terms of the whole-tire hysteresis ratio, tire load, and footprint dimensions based on energetic considerations. Their approach established a direct relationship between RR and the energy dissipated during cyclic deformation, providing a macroscopic metric that links viscoelastic material behavior to overall tire performance. This work demonstrated that RR can be fundamentally interpreted as a manifestation of energy loss within the tire structure.

On the other hand, numerical studies using FEM and thermo-mechanical simulations have enabled predictive analysis of RR based on viscoelastic properties. However, they often depend on empirical assumptions and may overlook parameter interdependencies.

Ebbott *et al.* (1999) investigated the coupled thermo-mechanical behavior of tires using finite element analysis and demonstrated that RR is strongly influenced by temperature evolution within the tire. Cyclic deformation generates heat, which alters viscoelastic properties and hysteresis losses, creating a nonlinear feedback mechanism. Their results indicate that accurate prediction of RR requires simultaneous consideration of thermal and mechanical effects.

Shida *et al.* (1999) demonstrated that RR can be effectively estimated using static finite element analysis by incorporating equivalent hysteresis effects. Their approach significantly reduced computational complexity while maintaining reasonable accuracy, thus highlighting the practicality of numerical modeling in tire performance prediction. However, the use of simplified static representations also indicates limitations in fully capturing coupled dynamic and rate-dependent behaviors.

Luchini *et al.* (2001) studied tire RR for a group of radial medium truck tires, both experimentally and numerically (FEA modeling). They investigated the effect of tread depth on tire RR and demonstrated that increasing tread depth increases energy dissipation through greater cyclic deformation of the rubber. Their results showed a clear positive correlation between tread depth and RR, indicating that even small geometric variations can significantly influence hysteresis losses. This study highlights the strong dependence of RR on geometric design parameters and the trade-off between energy efficiency and traction performance.

Ma *et al.* (2007) developed an energy-based model to compute RR by analyzing hysteresis losses in viscoelastic rubber materials. Their approach demonstrated that RR arises from cyclic energy dissipation during deformation and can be quantitatively predicted from material properties. The study provided a fundamental link between viscoelastic behavior and tire performance, emphasizing that RR is primarily governed by material-induced energy losses.

Wang *et al.* (2018) proposed a region-based framework for RR analysis, demonstrating that energy dissipation is spatially non-uniform within tire structures. By dividing the tire into crown and non-crown regions and performing finite element-based sensitivity analysis, they showed that the crown region, particularly the tread, dominates RR with nearly 70 % contribution. At the same time, other components such as the sidewall, carcass, and apex contribute to the remaining portion. The study further revealed that different structural parameters exhibit location-dependent sensitivity, indicating that RR is governed by both the magnitude and spatial distribution of energy loss. This work highlights the limitations of purely global models and underscores the importance of localized structural optimization.

Mangal *et al.* (2021) introduced a variable modulus framework to optimize RR by tailoring the spatial distribution of mechanical properties within the tire. Their results showed that RR is closely linked to viscoelastic deformation, where an increased modulus reduces hysteresis losses, while a lower modulus enhances grip. By strategically varying the modulus across different regions, the study demonstrated the potential to mitigate the traditional trade-off between RR and traction. This work highlights the critical role of material distribution in governing tire energy dissipation and performance.

Jittham *et al.* (2022) employed finite element analysis to investigate the RR behavior of pneumatic and solid tires, providing insight into the role of structural configuration and material behavior. Their results showed that tire structure significantly affects deformation patterns, stress distribution, and energy dissipation mechanisms. These findings demonstrate that RR is not solely determined by material properties but is strongly influenced by the interactions among structure, material behavior, and contact mechanics. They showed that increasing the contact area reduced tire RR, whereas increasing the tread depth increased it.

Ydrefors *et al.* (2024) investigated RR at low temperatures and found that lower temperatures significantly alter the viscoelastic behavior of tire materials. Increased stiffness and changes in hysteresis characteristics lead to higher energy dissipation and, consequently, increased RR. The study further demonstrated that tire behavior under low-temperature conditions deviates from standard testing assumptions, underscoring the need to account for real-world operating conditions in RR analysis.

Most existing studies examine individual parameters independently, whereas in practical tire design, multiple parameters, such as diameter, sidewall, and seated width, are simultaneously varied. This limitation restricts the applicability of existing models when multiple design variables are modified concurrently. Furthermore, conventional approaches often rely on nominal geometric parameters that may not accurately reflect tire behavior under rolling conditions, where deformation alters the effective geometry.

While previous research has extensively examined the influence of applied load on RR, the tire's own mass has not been explicitly treated as a separate parameter. This may be attributed to the dominant influence of external loading conditions in typical operating scenarios, as well as the practical difficulty of isolating tire mass effects experimentally. In this study, an effort is made to account for tire mass within the modeling framework explicitly.

To address these limitations, the present study investigates the combined effects of key tire design parameters, including tire mass, dynamic sidewall, dynamic diameter, and seated width, on RR. In contrast to nominal values, dynamic (functional) geometric parameters better capture the tire's actual deformation characteristics during rolling.

Based on experimental measurements conducted under controlled conditions in accordance with ISO 28580, individual relationships between each parameter and RR are established using curve-fitting techniques. A comprehensive analytical model is then developed by combining these effects within a unified framework. The originality of this work lies in the formulation of an analytical structure that integrates the independent empirical relations of each design factor into a unified model.

Unlike conventional weighting approaches such as constant or sigmoid-based models, which rely on predefined functional forms, the present study introduces a sliding normalization model (MSN) to determine weighting coefficients in a data-adaptive manner. In this approach, the contribution of each parameter is dynamically adjusted based on its relative position within the dataset range, allowing the model to better reflect variations in parameter influence without imposing prior assumptions. Therefore, the MSN provides a more general and adaptable framework for modeling RR than the other two approaches.

It should be noted that the proposed framework is semi-empirical, in which the total RR is represented as a weighted superposition of individual parameter effects. Although explicit interaction terms are not included, variable weighting coefficients enable indirect consideration of concurrent parameter influences. The proposed model is validated using independent experimental data and demonstrates improved predictive performance compared to conventional weighting approaches. However, the model is developed within a specific parameter range and under controlled testing conditions, and its applicability beyond this domain requires further investigation.

The remainder of this paper is organized as follows. Section 2 describes the experimental work and data acquisition. Section 3 presents the analytical modeling. Section 4 presents a comprehensive analytical model, and finally, Section 5 discusses the results and model validation.

2. Experimental work

An ISO 28580-based RR testing machine (as shown in Fig. 1) is employed to measure the RR of the test tires. The system includes controlled loading, speed, and environmental conditions to ensure repeatability and accuracy of the measurements.

Fig. 1. Schematic of the experimental setup used for RR measurements in accordance with ISO 28580.

Prior to experimentation, the Design of Experiments (DoE) framework was established, comprising the selected parameters, the number of tests, replications, environmental conditions, permissible and impermissible errors, estimates and approximations, testing procedures, standards, requirements, and constraints. All aspects of the test – requirements, conditions, specifications, tolerances, errors, correction factors, and the testing procedure – conformed to ISO 28580 (2018 edition) and ECE Regulation No. 117 (2016 edition).

The RR measurements were conducted using a drum-type testing machine. The apparatus consists of a steel drum with a 2 m diameter, designed to minimize vibration and ensure stable test conditions. During the tests, the tire was mounted on the spindle and brought into contact with the rotating drum, where a normal load equivalent to 80 % of the tire's maximum allowable load was applied. All tests were performed under controlled laboratory conditions, with an ambient temperature maintained at 25 °C, a constant inflation pressure of 210 kPa (±3 kPa), and a steady rolling speed of 22.2 m/s (±0.14 m/s). Prior to data acquisition, each tire underwent a warm-up phase of approximately 30 minutes to reach thermal equilibrium. The RR force was then measured under steady-state conditions, and multiple measurements were performed to ensure repeatability and reliability of the results. All test procedures, tolerances, correction factors, and measurement protocols were implemented in accordance with ISO 28580 requirements to ensure consistency and comparability of the obtained data. Operational parameters such as inflation pressure, temperature, and speed were kept constant in order to isolate the effects of tire design parameters. Incorporating these operational variables into the model is considered a direction for future research.

Table 1 shows selected parameters related to the testing equipment and testing conditions.

2.1. Design parameters and test tires

This study focuses on the design-parameter group among the four parameter groups – tire design parameters, environmental parameters, tire performance parameters, and road parame-

Table 1. Parameters related to the testing equipment and testing conditions.

Parameter	Value
Drum diameter of the RR machine	2 m
Ambient temperature in the drum, 1 meter above the drum, and 15 centimeters below the drum	25 °C
Linear test velocity / Speed of the drum (Class C1 tires)	22.2 m/s (±0.14 m/s)
Tire acceleration	$0.14\,\mathrm{m/s^2}$
Tire pressure (ambient air)	210 kPa (±3 kPa)
Tire warm-up time	30 min
Tire Spindle force (Class C1 tires)	Min: 100 N
	Max: 200 N
The load applied to the tire is 80% of the tire's maximum allowable load	

ters – that influence RR. Unlike the other three groups, design parameters are specific to the tire manufacturer and designer. The study meticulously and comprehensively analyzes four parameters from the design-parameter group: tire mass, overall diameter, sidewall, and seated width. To do this, four sets of test tires are selected, each with only one of these design parameters fixed, while the remaining parameters vary.

In the existing literature, RR has been predominantly analyzed in relation to external load, which represents the operational weight applied to the tire. Consequently, the contribution of the tire's own mass has not been explicitly isolated or systematically investigated. This is likely due to the experimental challenges associated with decoupling tire mass from other design parameters. The present work addresses this limitation by explicitly considering tire mass as an independent variable. By incorporating tire mass as an independent parameter, the proposed model provides a more comprehensive representation of RR behavior. It is foreseeable that an increase in tire weight will lead to greater heat generation, increased energy loss, and consequently higher RR. To quantify tire mass effects, two test tire series were selected. Each series is geometrically identical to the others, but their compounds – and hence their masses – differ (as shown in Table 2). The compounds employed in this study are of three types, and the densities of these compounds fall between $0.9\,\mathrm{g/cm^3}$ and $1.2\,\mathrm{g/cm^3}$.

Herein, the examination of the influence of the tire sidewall on RR presents a fundamental difference from prior research. The numerical value of the tire sidewall is computed from the tire diameter rather than from the tire width. In addition, the dynamic sidewall derived from the dynamic diameter is employed here. Because the aspect ratio (the sidewall-to-width ratio) is a bivariate parameter, and its consideration does not permit precise isolation of the individual effects of tire sidewall and tire width on RR, the effect of tire sidewall, instead of the aspect ratio, is examined here. In evaluating the influence of tire sidewall on RR, not only must all geometric parameters (except for the sidewall) of the tested tires be identical, but the material of the sidewall of the tires must also be the same. In this study, five test tires are used, each with a different sidewall (and mass), while keeping other design parameters, including width, constant (as shown in Table 2).

The nominal radius, or the unloaded radius of a tire, also referred to as the overall radius, is one of the important parameters that affect tire RR. The static radius for a stationary vehicle, depending on the sidewall value and the tire compound, typically has about 5 % to 10 % sag relative to the nominal radius. In contrast, the dynamic radius, which depends on vehicle and wind velocities and the tire's overall stiffness, is larger than the static radius. Here, the tire's dynamic radius is examined. To evaluate tire diameter, the tire pressure and load applied to all test tires must match the standard values; otherwise, these influential parameters may introduce errors in the evaluation of the tire diameter's effect on RR. In this study, five test tires are

Table 2. RR values measured for the test tires.

Design parameters	Tire size	Dynamic sidewall [m]	Dynamic diameter [m]	Seated width [m]	Mass [kg]	RR_0 [N/kN]	RR_C
Mass	205/50R17	0.092	0.566	0.164	9.07	9.15	9.15
		0.093	0.574		9.34	9.43	9.43
		0.095	0.581		9.62	9.65	9.65
	215/55R18	0.106	0.660	0.174	11.135	8.84	8.84
		0.1085	0.670		11.350	9.08	9.08
		0.11	0.677		11.530	9.21	9.21
Sidewall	225/55R19	0.1107	0.704	0.174	12.640	9.45	9.45
	225/60R18	0.1224	0.702		12.810	9.52	9.367
	225/65R17	0.1331	0.698		13.050	9.60	9.231
	225/70R16	0.1453	0.697		12.550	9.10	9.18
	225/75R15	0.1565	0.694		12.300	8.81	9.15
Diameter	205/60R13	0.113	0.556	0.164	7.640	8.9	9.80
	205/60R14	0.112	0.580		8.155	9.14	9.644
	205/60R15	0.112	0.605		8.715	9.31	9.31
	205/60R16	0.111	0.627		9.270	9.20	8.645
	205/60R17	0.112	0.655		9.810	9.50	8.515
Seated width	205/55R16	0.1013	0.609	0.164	8.350	9.22	9.22
				0.172		8.85	8.85
				0.1756		8.40	8.40
				0.1795		8.22	8.22
				0.1808		8.17	8.17

employed, differing only in diameter and mass, and all other design parameters and practical conditions (tire pressure, applied load, tire velocity, etc.) are kept constant (as shown in Table 2).

The seated width of a tire, a design parameter with a fixed value, is defined as the width of the tire's ground-contact patch under a standard load and inflation pressure. Herein, variations in seated width due to changes in the tire pressure, vehicle weight, or the load applied to the tire are not considered. An increase in seated width leads to an enlargement of the tire-ground contact area, a reduction in vertical pressure, less localized deformation, lower energy losses, and, consequently, a reduction in tire RR. In this study, five test tires are employed, differing only in seated width, while all other design parameters remain the same (as shown in Table 2).

2.2. Test results

The results of the RR tests (RR_0) for four design parameters – mass, sidewall, diameter, and seated width – are presented in Table 2.

3. Analytical model

3.1. Mass effect on RR

Using the Curve Fitting Toolbox-MATLAB, a linear regression equation for the RR values as a function of the tire mass is approximated as follows:

$$\begin{aligned} \mathrm{RR}(M_1) &= 0.9083\,M_1 + 0.9232, \\ \mathrm{RR}(M_2) &= 0.9425\,M_2 - 1.6427, \end{aligned} \tag{3.1}$$

where RR is the RR value (RR_0 values are shown in Table 2) and M is the mass of the test tires. The subscripts 1 and 2 denote the two test tire series used for evaluating the effect of the tire mass parameter on RR.

Equation (3.1) shows that the change in tire RR with mass is linear, with a slope of 90 %. Although the tires used to examine the effect of mass are geometrically identical, and generalizing to the entire range of tires is challenging, examining tires from the Michelin and Bridgestone brands (tires are geometrically identical but with different densities) also suggests that a linear regression equation with a slope close to 100 % for RR as a function of the tire mass can be approximated. By extending this equation to all tires in the 8 to 12 [kg] range (which includes most passenger tires), a linear regression equation for the influence of mass on RR is approximated as follows (it is shown in Fig. 2):

$$\mathrm{RR}(M) = 0.9\,M + 0.987. \tag{3.2}$$

The predicted RR values from the fitted mass-effect curve are presented in Table 3.

Table 3. Predicted RR values from the fitted curve (mass effect).

Tire size	Mass [kg]	RR_0	RR_C	RR_1
205/50R17	9.07	9.15	9.15	9.15
	9.34	9.43	9.43	9.393
	9.62	9.65	9.65	9.645
215/55R18	11.135	8.84	8.84	11.009
	11.350	9.08	9.08	11.202
	11.530	9.21	9.21	11.364

The derived linear relationship between tire mass and RR is valid over the investigated mass range (8 kg to 12 kg), which corresponds to typical passenger-car tires. Application of this relationship outside this range may introduce additional uncertainty. It should be noted that the proposed mass-RR relationship is derived empirically based on experimental data within the investigated mass range and should not be extrapolated beyond this domain. The non-zero intercept of the fitted function arises from the curve-fitting process. It does not represent a physically meaningful condition, since a tire of zero mass is not physically realizable.

As shown in Fig. 2, RR increases approximately linearly with tire mass for geometrically identical tires. This trend can be attributed to the increased material volume and internal hysteresis losses associated with heavier tires. The observed linear behavior over the investigated mass range (8 kg to 12 kg) supports the use of a first-order approximation to model the mass–RR

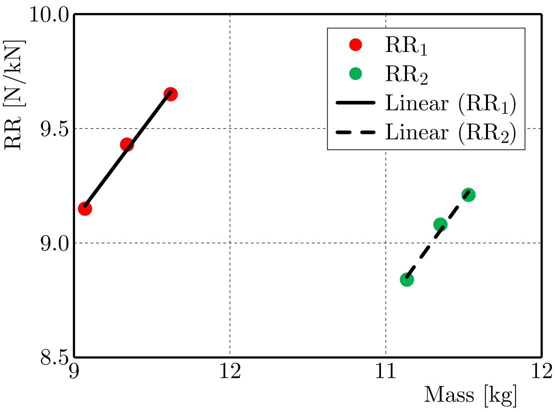

Fig. 2. Relationship between tire mass and RR for tires with identical geometric characteristics. The results indicate an approximately linear trend within the investigated mass range, supporting the use of a first-order approximation.

relationship. It should be noted, however, that this linearity is valid within the studied domain and may not necessarily extend beyond this range.

3.2. Sidewall effect on RR

In examining the effect of tire sidewall and diameter parameters on RR, the test specimens not only have different sidewall and diameter values but also vary in mass (as shown in Table 2). This difference in the mass of the test specimens is due, from a technical standpoint, to the fact that it is not feasible to produce tires with different sidewall and diameter values that have the same mass. Therefore, by equalizing tire mass, the influence of mass changes on RR must be removed from the test results to ensure that the findings reflect solely the effects of tire sidewall or diameter parameters on RR. Using Eq. (3.2), the influence of mass changes on the RR values is removed (see RR_C in Table 2).

Using the Curve Fitting Toolbox-MATLAB, the quadratic and cubic equations are identified as the best candidates for the fitting curve of the RR values as a function of the sidewall. First, the accuracy of these two models is assessed using the root-mean-square (RMS) percentage error (% RMSE) criterion:

$$\mathrm{RMSE}\,(\%) = 100\frac{\sqrt{\frac{\sum_{i=1}^{N}[\mathrm{RR}_C(i)-\mathrm{RR}_{\mathrm{Model}}(i)]^2}{N}}}{\sum_{i=1}^{N}\frac{\mathrm{RR}_C(i)}{N}}, \tag{3.3}$$

where RR_C are the corrected test results for RR (RR_C can be seen in Table 2), and $\mathrm{RR}_{\mathrm{Model}}$ are the predicted RR values from the fitted curve (RR_2 and RR_3 can be seen in Table 4). Additionally, N is the number of data points.

Table 4. Predicted RR values from the fitted curve (sidewall effect).

Tire size	RR_C	RR_2	RR_3
225/55R19	9.45	9.46	9.453
225/60R18	9.367	9.338	9.352
225/65R17	9.231	9.251	9.251
225/70R16	9.18	9.182	9.166
225/75R15	9.15	9.146	9.153

From Table 4 and using Eq. (3.3), the RMSE values are computed for each model, therefore

$$\mathrm{RMSE}_2 = 0.18\,\%, \qquad \mathrm{RMSE}_3 = 0.14\,\%.$$

Considering the RSME values, both models are acceptable. Here, the more straightforward quadratic equation is used. It should be noted that although higher-order polynomial models (e.g., cubic) were also evaluated, they did not provide a significant improvement in accuracy compared to quadratic models. Therefore, quadratic functions were selected to maintain model simplicity and avoid potential overfitting. The fitted curve for the RR values as a function of the tire sidewall (S) is expressed as follows (it is shown in Fig. 3):

$$\mathrm{RR}(S) = 105.22\,S^2 - 34.986\,S + 12.044. \tag{3.4}$$

Figure 3 illustrates the effect of the dynamic sidewall on RR after applying mass correction (RR_C). The results indicate a clear dependency of RR on sidewall height. This behavior can be explained by the role of sidewall deformation in energy dissipation mechanisms. Tires with larger sidewall values tend to exhibit different deformation patterns, which directly influence hysteresis losses and, consequently, RR.

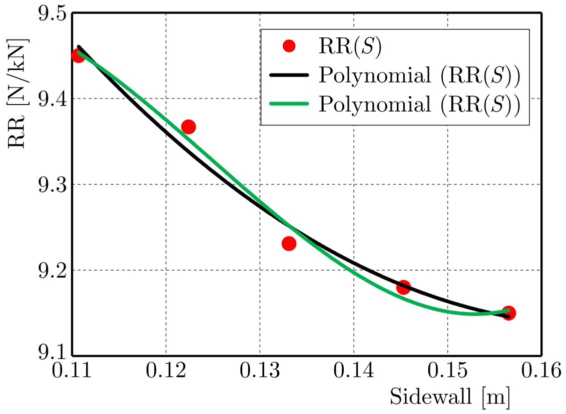

Fig. 3. Effect of dynamic sidewall on corrected rolling resistance (RR_C). Experimental data after removing the influence of tire mass are presented as red markers, while quadratic and cubic regression fits are shown by black and green lines, respectively.

3.3. Diameter effect on RR

The quadratic and cubic equations are identified as the best candidates for fitting the RR values as a function of diameter. From the predicted RR values from the fitted curve (RR_2 and RR_3 can be seen in Table 5) and using Eq. (3.3), the RMSE values are computed for each model, thus

$$\mathrm{RMSE}_2 = 1.5\,\%, \qquad \mathrm{RMSE}_3 = 1\,\%.$$

Table 5. Predicted RR values from the fitted curve (diameter effect).

Tire size	RR_C	RR_2	RR_3
205/60R13	9.80	9.809	9.730
205/60R14	9.644	9.514	9.654
205/60R15	9.310	9.191	9.240
205/60R16	8.645	8.893	8.812
205/60R17	8.515	8.495	8.494

Considering the RSME values, both models are acceptable. Here, the more straightforward quadratic equation is used. Therefore, the fitted curve for the RR values as a function of the diameter (D) is expressed as follows (it is shown in Fig. 4):

$$\mathrm{RR}(D) = -13.269\,D^2 + 2.8\,D + 12.354. \tag{3.5}$$

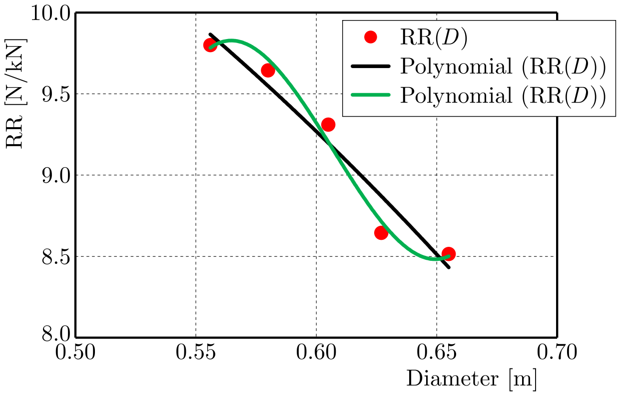

Fig. 4. Effect of dynamic diameter on RR_C. Experimental data, after removing the influence of tire mass, are presented as red markers, and quadratic and cubic regression fits are shown by black and green lines, respectively.

As shown in Fig. 4, increasing the dynamic diameter generally reduces RR. This can be physically interpreted as larger diameters reducing the curvature of the contact region, thereby decreasing cyclic deformation and associated energy losses per revolution. The trend is consistent across the dataset under investigation and supports including diameter as a key design parameter.

3.4. Seated width effect on RR

The quadratic and cubic equations are identified as the best candidates for fitting the RR values as a function of seated width. From the predicted RR values from the fitted curve (RR_2 and RR_3 can be seen in Table 6) and using Eq. (3.3), the RMSE values are computed for each model, hence

$$\mathrm{RMSE}_2 = 0.068\,(0.8\,\%), \qquad \mathrm{RMSE}_3 = 0.107\,(1.25\,\%).$$

Table 6. Predicted RR values from the fitted curve (seated width effect).

Tire size	Seated width [m]	RR_0	RR_2	RR_3
205/55R16	0.164	9.22	9.236	9.321
	0.172	8.85	8.753	8.941
	0.1756	8.40	8.511	8.532
	0.1795	8.22	8.230	8.287
	0.1808	8.17	8.132	8.299

Considering the RSME values, both models are acceptable. Here, the more straightforward quadratic equation is used. Therefore, the fitted curve for the RR values as a function of the seated width (W) is expressed as follows (it is shown in Fig. 5):

$$\mathrm{RR}(W) = -608.9\,W^2 + 144.21\,W + 1.9629. \tag{3.6}$$

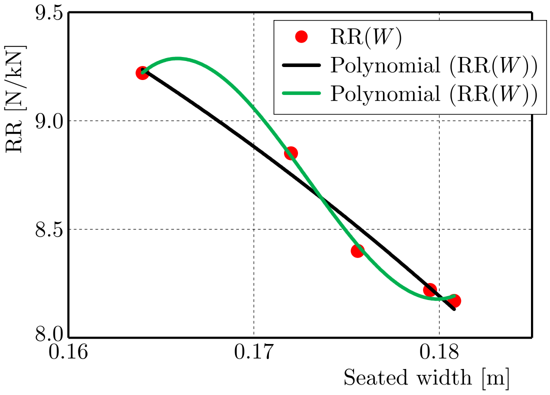

Fig. 5. Effect of seated width on rolling resistance (RR_0). Experimental data are presented as red markers, and quadratic and cubic regression fits are shown by black and green lines, respectively.

Figure 5 presents the influence of seated width on RR. The results suggest that variations in seated width affect the contact patch geometry and stress distribution, which in turn influence deformation behavior and hysteresis losses. Although the relationship is not strictly linear, the observed trend confirms that seated width is an important parameter in RR modeling.

4. Comprehensive analytical model

In tire design, it is essential to have a comprehensive model that can simultaneously predict the effects of tire geometric parameters (sidewall, diameter, and seated width) and mass on RR. This comprehensive model can be expressed in the form of Eq. (4.1):

$$\mathrm{RR}(S,D,W,M) = C(S)\mathrm{RR}(S) + C(D)\mathrm{RR}(D) + C(W)\mathrm{RR}(W) + C(M)\mathrm{RR}(M), \tag{4.1}$$

in which the function $\mathrm{RR}(S, D, W, M)$ is the comprehensive model for RR, and the coefficients $C(X)$ represent the contribution and weight of parameter X in the comprehensive model of RR. Herein, three approaches to determining $C(X)$ coefficients are presented: one assumes the coefficients are constant, and two assume the coefficients are variable.

It should be noted that the proposed formulation is semi-empirical, in which the total RR is represented as a weighted superposition of individual parameter effects. Although explicit interaction terms are not included, the use of variable weighting coefficients in the MSN framework permits indirect consideration of concurrent parameter influences.

4.1. Comprehensive model with constant coefficients

The constant coefficient approach is presented primarily as a baseline model for comparison. As expected, its predictive performance is lower than that of the adaptive weighting approaches. To determine the constant coefficients C, mid tires are selected from each set of test tires (as shown in Table 7), and the geometric parameters of the selected tires – including sidewall, diameter, and seated width – as well as their masses and the predicted RR values from the fitted curves (RR_1 and RR_2) are substituted into the comprehensive model.

Table 7. Mid tire specifications.

Design parameters	Tire size	Dynamic sidewall	Dynamic diameter	Seated width	Mass
Mass	205/50R17	0.093	0.574	0.164	9.34
Sidewall	225/65R17	0.1331	0.698	0.174	12.640
Diameter	205/60R15	0.112	0.605	0.164	8.715
Seated width	205/55R16	0.1013	0.609	0.1756	8.350

Therefore, the equations of the comprehensive model can be simplified as follows:

$$\begin{aligned}
9.251\,C_1 + 7.844\,C_2 + 8.620\,C_3 + 12.363\,C_4 &= 9.251,\\
9.445\,C_1 + 9.191\,C_2 + 9.236\,C_3 + 8.831\,C_4 &= 9.191,\\
9.580\,C_1 + 9.138\,C_2 + 8.511\,C_3 + 8.502\,C_4 &= 8.511,\\
9.70\,C_1 + 9.098\,C_2 + 9.236\,C_3 + 9.393\,C_4 &= 9.393.
\end{aligned}$$

From solving the above system of equations, the coefficients C_i are obtained. Then the coefficients are normalized to lie in the range $[-1, 1]$ and finally substituted into Eq. (4.1), yielding a comprehensive model with constant coefficients. Therefore

$$\begin{aligned}
\mathrm{RR}(S, D, W, M) = {} & 0.244(105.220\,S^2 - 34.986\,S + 12.044)\\
& + 0.288(-13.269\,D^2 + 2.80\,D + 12.354)\\
& + 0.458(-608.90\,W^2 + 144.21\,W + 1.9629)\\
& + 0.01(0.9\,M + 0.987).
\end{aligned} \tag{4.2}$$

4.2. Comprehensive model with sigmoid variable coefficients

An analysis of plots derived from the analytical equations of the geometric parameters and mass reveals an S-shaped, or sigmoid, behavior. Accordingly, the sigmoid function is adopted to determine the coefficients of the comprehensive model. The sigmoid model employed is expressed as follows:

$$\frac{\mathrm{RR}(X)_{\max} - C(X)}{C(X) - \mathrm{RR}(X)_{\min}} = \exp[K_X(X - X_C)]. \tag{4.3}$$

The sigmoid variable coefficients are therefore determined as:

$$C(X) = \mathrm{RR}(X)_{\min} + \frac{\mathrm{RR}(X)_{\max} - \mathrm{RR}(X)_{\min}}{1 + \exp[K_X(X - X_C)]}, \tag{4.4}$$

where $\mathrm{RR}(X)_{\mathrm{max}}$ and $\mathrm{RR}(X)_{\mathrm{min}}$ represent the maximum and minimum values of RR predicted from the fitted curve corresponding to parameter X, K_X denotes the slope coefficient of the sigmoid function, and X_C denotes the value of parameter X at which RR is at its average value (it can be seen in Table 8 to Table 11). To determine coefficient K_X, the data corresponding to each parameter (as shown in Table 8 to Table 11) are substituted into the sigmoid model (Eq. (4.4)), the corresponding K_X values are computed, and the most accurate K_X coefficient is selected using the RMS criterion.

Table 8. Data corresponding to mass parameter.

M	RR	$\mathrm{RR}(X)_{\mathrm{max}}$	$\mathrm{RR}(X)_{\mathrm{min}}$	$\mathrm{RR}(X)_{\mathrm{avg}}$	X_C	K_X
9.07	9.15	9.645	9.15	9.398	9.345	−0.84
9.34	9.393					
9.62	9.645					

Table 9. Data corresponding to sidewall parameter.

S	RR	$\mathrm{RR}(X)_{\mathrm{max}}$	$\mathrm{RR}(X)_{\mathrm{min}}$	$\mathrm{RR}(X)_{\mathrm{avg}}$	X_C	K_X
0.1107	9.460	9.460	9.146	9.276	0.1297	110
0.1224	9.338					
0.1331	9.251					
0.1453	9.182					
0.1565	9.146					

Table 10. Data corresponding to diameter parameter.

D	RR	$\mathrm{RR}(X)_{\mathrm{max}}$	$\mathrm{RR}(X)_{\mathrm{min}}$	$\mathrm{RR}(X)_{\mathrm{avg}}$	X_C	K_X
0.556	9.809	9.809	8.495	9.152	0.608	45
0.580	9.514					
0.605	9.191					
0.627	8.893					
0.655	8.495					

Table 11. Data corresponding to seated width parameter.

W	RR	$\mathrm{RR}(X)_{\mathrm{max}}$	$\mathrm{RR}(X)_{\mathrm{min}}$	$\mathrm{RR}(X)_{\mathrm{avg}}$	X_C	K_X
0.164	9.236	9.236	8.132	8.684	0.1731	350
0.172	8.753					
0.1756	8.511					
0.1795	8.230					
0.1808	8.132					

Therefore, the sigmoid variable coefficients are expressed as:

$$
\begin{aligned}
C(M) &= 9.150 + \frac{0.495}{1+\exp\left[-0.84(M-9.345)\right]},\\
C(S) &= 9.146 + \frac{0.314}{1+\exp\left[110(S-0.1297)\right]},\\
C(D) &= 8.495 + \frac{1.314}{1+\exp\left[45(D-0.608)\right]},\\
C(W) &= 8.132 + \frac{1.104}{1+\exp\left[350(W-0.1731)\right]}.
\end{aligned}
\tag{4.5}
$$

The coefficients are then normalized and finally substituted into Eq. (4.1), yielding a comprehensive model with sigmoidal variable coefficients.

4.3. MSN comprehensive model

Here, a new model (research innovation) named the “Slide Model” (MSN) is presented. As shown in Fig. 6, the MSN model is expressed as follows:

$$\frac{\ln Y_{\max} - \ln Y(X)}{\ln Y_{\max} - \ln Y_{\min}} = \left(\frac{X - X_{\min}}{X_{\max} - X_{\min}}\right)^2. \tag{4.6}$$

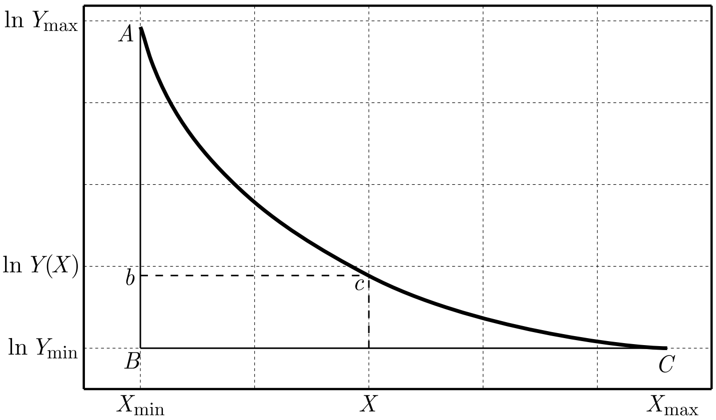

Fig. 6. MSN model used to determine the coefficients of the comprehensive model.

The quantity $Y(X)/Y_{\max}$ is regarded as the variable coefficient $C(X)$, and Eq. (4.6) is then rewritten as follows:

$$\begin{aligned} \ln C(X) &= \ln\left(\frac{\mathrm{RR}(X)_{\min}}{\mathrm{RR}(X)_{\max}}\right)\left(\frac{X - X_{\min}}{X_{\max} - X_{\min}}\right)^2, \\ C(X) &= \exp\left[\left(\frac{\mathrm{RR}(X)_{\min}}{\mathrm{RR}(X)_{\max}}\right)\left(\frac{X - X_{\min}}{X_{\max} - X_{\min}}\right)^2\right]. \end{aligned} \tag{4.7}$$

The above equation for the mass parameter is rewritten as follows:

$$C(X) = \exp\left[\left(\frac{\mathrm{RR}(X)_{\min}}{\mathrm{RR}(X)_{\max}}\right)\left(\frac{X - X_{\max}}{X_{\max} - X_{\min}}\right)^2\right]. \tag{4.8}$$

All parameters of the two relations above were listed in Table 8 to Table 11. Therefore, the MSN variable coefficients are expressed as:

$$\begin{aligned} C(M) &= \exp\left[\left(\frac{9.15}{9.645}\right)\left(\frac{M - 9.62}{0.55}\right)^2\right], \\ C(S) &= \exp\left[\left(\frac{9.146}{9.460}\right)\left(\frac{S - 0.1107}{0.0458}\right)^2\right], \\ C(D) &= \exp\left[\left(\frac{8.495}{9.809}\right)\left(\frac{D - 0.556}{0.099}\right)^2\right], \\ C(W) &= \exp\left[\left(\frac{8.132}{9.236}\right)\left(\frac{W - 0.164}{0.0168}\right)^2\right]. \end{aligned} \tag{4.9}$$

The coefficients are then normalized and finally substituted into Eq. (4.1), yielding a comprehensive model with MSN variable coefficients.

It should be noted that the proposed formulation in Eq. (4.1) is semi-empirical in nature, where the total RR is represented as a weighted superposition of individual parameter effects. Although explicit interaction terms are not included, the use of variable weighting coefficients in the MSN framework permits indirect consideration of concurrent parameter influences. The MSN formulation relies on normalization within the dataset's minimum and maximum bounds; therefore, its application outside the calibrated parameter range should be performed with caution.

5. Results and model validation

The results and comparisons of the models are presented in Table 12, where the predicted values from the fitted curve and from the comprehensive models – comprising the constant coef-

Table 12. Data corresponding to mass parameter.

Tire		RR_0	RR_{Fitted}	$RR_{Constant}$	$RR_{Sigmoid}$	RR_{MSN}	$RMS_{Constant}$ [%]	$RMS_{Sigmoid}$ [%]	RMS_{MSN} [%]	Equalized mass
Test tires (sidewall)	225/55R19	9.45	9.460	8.63	9.820	9.699	7.5	5.5	4.1	12.64
	225/60R18	9.52	9.338	8.60	9.790	9.667				
	225/65R17	9.60	9.251	8.58	9.770	9.644				
	225/70R16	9.10	9.182	8.57	9.75	9.63				
	225/75R15	8.81	9.146	8.56	9.75	9.61				
Test tires (diameter)	205/60R13	8.9	9.809	9.49	9.340	9.37	3.6	3.8	3.7	8.715
	205/60R14	9.14	9.514	9.36	9.262	9.288				
	205/60R15	9.31	9.191	9.27	9.180	9.20				
	205/60R16	9.20	8.893	9.19	9.10	9.12				
	205/60R17	9.50	8.495	9.07	9.01	9.03				
Test tires (seated width)	205/55R16	9.22	9.236	9.28	9.123	9.166	5.4	5.7	6.0	8.35
	205/55R16	8.85	8.753	9.07	9.00	9.03				
	205/55R16	8.40	8.511	8.95	8.94	8.97				
	205/55R16	8.22	8.230	8.83	8.88	8.909				
	205/55R16	8.17	8.132	8.78	8.86	8.888				
Test tires (mass)	205/50R17	9.15	9.15	9.44	9.423	9.43	2.2	1.8	1.8	9.07
	205/50R17	9.43	9.393	9.44	9.482	9.48				9.34
	205/50R17	9.65	9.645	9.45	9.54	9.54				9.62
Out-of-test tires	225/65R17	9.6	N/A	8.59	9.895	9.747	7.0	3.7	2.8	13.05
	205/60R17	9.5		9.08	9.274	9.30				9.81
	205/60R15	9.31		9.27	9.19	9.21				8.715
	205/55R16	8.85		9.06	9.01	9.00				8.35
	235/50R19	10.13		8.69	9.98	9.91				12.500
	165/65R13	9.7		10.12	9.13	9.54				5.360
	215/55R18	8.84		8.756	9.38	9.379				11.135
	215/55R18	9.08		8.758	9.434	9.40				11.350
	215/55R18	9.21		8.759	9.58	9.48				11.530

ficients, sigmoid variable coefficients, and MSN variable coefficients for 27 tires (comprising the 21 test tires and 6 additional tires not used in model calibration) – are evaluated against the measurements obtained with the RR testing apparatus. It should be noted that, to verify the models, the second series of tires from the mass test, with a size of 215/55R18 (without accounting for mass changes), along with the 6 additional tires not used in model calibration, were used in addition to the test tires.

In addition, Fig. 7 and Fig. 8 show scatter plots comparing the RR values of the models and the experimental results for both the test tires and the additional tires not used in model calibration.

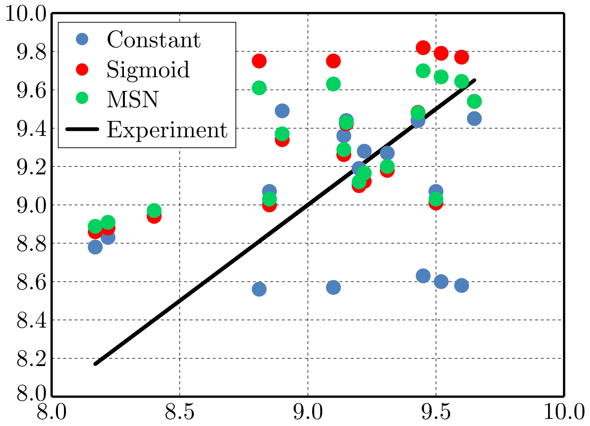

Fig. 7. Comparison of RR predictions using constant, sigmoid, and MSN weighting approaches. The MSN model shows improved agreement with experimental data across the investigated parameter range.

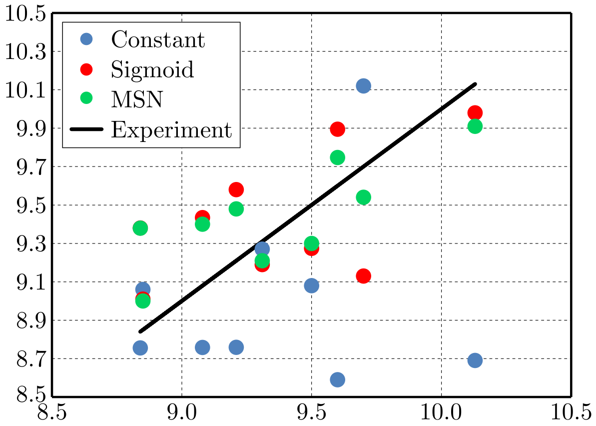

Fig. 8. Validation of the proposed model using independent tire data not included in the calibration set. The MSN approach demonstrates improved predictive performance compared to conventional methods within the studied domain.

Figure 7 compares the predictive performance of the constant, sigmoid, and MSN weighting approaches. The MSN model provides closer agreement with experimental data across the parameter range. This improvement can be attributed to the data-adaptive nature of the MSN weighting mechanism, which enables the model to capture variations in parameter influence better.

As shown in Fig. 8, the validation results using independent tire data demonstrate that the MSN model achieves the lowest prediction error among the evaluated approaches. This indicates that the proposed method has improved predictive capability beyond the calibration dataset. Nevertheless, it should be noted that the validation is limited to the investigated parameter range.

According to Table 12, the predictive accuracy of the MSN model is markedly higher for tires that were not used in model calibration than for the other two models. For these tires, the MSN model exhibits an error of 2.8 %, while the sigmoid model attains 3.7 % and the constant coefficient model 7 %. The MSN model's ability to predict tire RR, not used in the formulation of the comprehensive analytical model, demonstrates its potential for development and generalization, highlighting it as a key strength of the approach. The constant coefficient model, while offering a fast, straightforward methodology suitable for multiple variables with linear variation, exhibits the lowest accuracy among the models studied.

6. Discussion

The results of this study provide new insights into how tire mass and geometric parameters collectively influence RR. The developed analytical framework integrates individual empirical relations for tire mass, sidewall, diameter, and seated width into a unified formulation. Compared to previous approaches that primarily treated these parameters independently, the present model captures their combined influence within a consistent structure. However, the interactions are represented semi-empirically.

The experimental analysis revealed that increases in tire mass consistently lead to higher RR values, primarily due to greater internal energy dissipation and viscoelastic deformation during rotation. This observation is consistent with the thermomechanical understanding that heavier tires experience larger cyclic strain amplitudes, which increase hysteresis losses and heat generation in the tread and carcass layers. Within the investigated range, the approximately linear relationship between mass and RR suggests that the dominant energy-loss mechanisms scale proportionally with tire mass; however, extrapolation beyond this range should be approached with caution.

The effects of geometric parameters – sidewall, diameter, and seated width – were also systematically evaluated. Increasing the tire sidewall reduces flexibility and increases structural stiffness, thereby reducing RR. Similarly, larger tire diameters reduce RR by decreasing deformation per unit revolution. At the same time, increasing seated width lowers RR by enlarging the contact area, distributing the load more uniformly, and reducing localized deformation. These trends are generally consistent with previous studies (e.g., Walter (1983) and Ebbott *et al.* (1999)), while the present work extends them by incorporating tire mass into the same analytical framework.

The proposed MSN demonstrated the best overall agreement with experimental data, achieving an average prediction error below 3%. In contrast to constant and sigmoid weighting approaches, the MSN formulation dynamically adjusts weighting coefficients based on the parameter values and their normalized ranges. This feature enables the model to partially capture nonlinear interactions among variables, although it does not explicitly represent physical coupling mechanisms. As a result, the MSN framework offers improved predictive capability within the studied parameter space. Nevertheless, since the formulation relies on normalization within the dataset's minimum and maximum bounds, its application outside the calibrated range requires careful validation. Furthermore, extension of the model to different tire categories or operating conditions would require additional experimental data and recalibration of the weighting functions.

7. Conclusion

This research developed and validated a comprehensive analytical model capable of predicting tire RR while accounting for mass and geometric parameters. Experimental measurements were performed using an ISO 28580-based RR testing apparatus on 21 passenger tires, providing the foundation for analytical modeling. Curve-fitting methods were applied to derive individual functional relationships between RR and each geometric parameter and tire mass; these relationships were subsequently integrated into a comprehensive analytical model. Three approaches were explored to determine the weighting coefficients that quantify each parameter's contribution within the model: constant coefficients, variable sigmoid-based coefficients, and a novel MSN. The MSN approach, introduced in this study, enables the derivation of dynamic weighting coefficients based on tire behavior within the considered dataset.

Model validation was performed by comparing the analytical predictions with experimental measurements for 27 tires (21 test tires and 6 additional tires not used in model calibration). The validation dataset includes tires with varying geometric and structural characteristics, providing an initial assessment of the model's predictive capability beyond the calibration set. The results indicate that the MSN model provides greater predictive accuracy than the other approaches. While the number of validation samples is limited, the results consistently show that the MSN model performs better than the alternative methods within the studied range. The MSN model achieves an RMS error of 2.8 %, whereas the sigmoid and constant coefficient models yield RMSE values of 3.7 % and 7 %, respectively.

The proposed approach provides a practical analytical framework for evaluating the influence of design parameters on RR. However, it should be noted that the model is semi-empirical in nature and is validated within the studied dataset and parameter ranges; therefore, its applicability beyond these conditions requires further investigation. In particular, the current formulation does not explicitly account for environmental and operating conditions such as temperature, inflation pressure, speed, and road surface, which may affect RR behavior.

The analytical framework presented here can serve as a basis for future research on multi-parameter tire optimization. Further studies may extend the MSN formulation by incorporating additional parameters and by validating the model using larger, more diverse datasets. In addition, coupling the proposed approach with finite element simulations or vehicle energy models could enhance its applicability for practical tire design and energy-efficiency assessments.

References

1. Ebbott, T.G., Hohman, R.L., Jeusette, J.-P., & Kerchman, V. (1999). Tire temperature and rolling resistance prediction with finite element analysis. *Tire Science and Technology*, *27*(1), 2–21. https://doi.org/10.2346/1.2135974

2. Ejsmont, J., Ronowski, G., Berge, T., Sommer, S., Owczarzak, W., & Szerszyńska, A. (2025). At what temperature should the tire rolling resistance be measured? *Proceedings of the Institution of Mechanical Engineers, Part D: Journal of Automobile Engineering*, *239*(12), 5961-5969. https://doi.org/10.1177/09544070241280316

3. Ejsmont, J., Ronowski, G., Ydrefors, L., Owczarzak, W., Sommer, S., & Świeczko-Żurek, B. (2024). Comparison of tire rolling resistance measuring methods for different surfaces. *International Journal of Automotive Technology*, *25*(4), 965–976. https://doi.org/10.1007/s12239-024-00092-w

4. Jittham, P., Sucharitpwatskul, S., Siriruk, S., & Meesaringkarn, S. (2022). Finite element analysis of elastomer: Case study – Rolling resistances of pneumatic and solid tyres. *IOP Conference Series: Materials Science and Engineering*, *1234*, Article 012002. https://iopscience.iop.org/article/10.1088/1757-899X/1234/1/012002

5. Liang, Ch., Li, H., Mousavi, H., Wang, G., & Yu, K. (2020). Evaluation and improvement of tire rolling resistance and grip performance based on test and simulation. *Advances in Mechanical Engineering*, *12*(12). https://doi.org/10.1177/1687814020981173

6. Luchini, J.R., Motil, M.M., & Mars, W.V. (2001). Tread depth effects on tire rolling resistance. *Tire Science and Technology*, *29*(3), 134–154. https://doi.org/10.2346/1.2135235

7. Ma, G., Xu, H., & Cui, W. (2007). Computation of rolling resistance caused by rubber hysteresis of truck radial tire. *Journal of Zhejiang University – SCIENCE A*, *8*, 778–785. https://doi.org/10.1631/jzus.2007.A0778

8. Mangal, Sh., Ghosh, P., Narasimha Rao, K.V., & Mukhopadhyay, R. (2021). Variable modulus approach to optimize tire rolling resistance. *Tire Science and Technology*, *49*(1), 39–54. https://doi.org/10.2346/tire.19.180200
9. Martini, M.E. (1983). Passenger tire rolling loss: A tread compounding approach and its tradeoffs. In D.J. Schuring (Ed.), *Tire rolling resistance* (pp. 181–197). American Chemical Society. https://books.google.com/books/about/Tire_Rolling_Resistance_Rubber_Division.html?id=gSkBMgAACAAJ
10. Pillai, P.S., & Fielding-Russell, G.S. (1992). Tire rolling resistance from whole-tire hysteresis ratio. *Rubber Chemistry and Technology*, *65*(2), 444–452. https://doi.org/10.5254/1.3538623
11. Shida, Z., Koishi, M., Kogure, T., & Kabe, K. (1999). A rolling resistance simulation of tires using static finite element analysis. *Tire Science And Technology*, *27*(2), 84–105. https://doi.org/10.2346/1.2135980
12. Walter, J.D., & Conant, F.S. (1974). Energy losses in tires. *Tire Science and Technology*, *2*(4), 235–260. https://doi.org/10.2346/1.2167188
13. Walter, S.L. (1983). The effects of five basic design and construction parameters on radial tire rolling resistance and cornering force. *SAE Transactions*, *92*, 579–591. https://www.jstor.org/stable/44644395
14. Wang, G., Wu, X., Liang, Ch., & Yang, J. (2018). Design of low rolling resistance tire structure based on region energy loss. *Recent Patents on Mechanical Engineering*, *11*(2), 135–145. https://doi.org/10.2174/2212797611666180509161710
15. Xu, Y., Liu, Y., Gao, Y., Liu, L., & Zhang, L. (2025). Designing high-performance green tire treads by reinforcing the styrene-butadiene rubber/silica interface with chain difunctionalization. *Composites Part B: Engineering*, *290*, Article 111887. https://doi.org/10.1016/j.compositesb.2024.111887
16. Ydrefors, L., Hjort, M., Kharrazi, S., Jerrelind, J., & Stensson Trigell, A. (2021). Rolling resistance and its relation to operating conditions: A literature review. *Proceedings of the Institution of Mechanical Engineers, Part D: Journal of Automobile Engineering*, *235*(12), 2931–2948. https://doi.org/10.1177/09544070211011089
17. Ydrefors, L., Hjort, M., Kharrazi, S., Jerrelind, J., & Stensson Trigell, A. (2024). Measurement and evaluation of rolling resistance of car tyres at low operating temperatures. In W. Huang & M. Ahmadian (Eds.), *Advances in Dynamics of Vehicles on Roads and Tracks III* (pp. 845–856). Springer. https://link.springer.com/chapter/10.1007/978-3-031-66968-2_83

Manuscript received January 7, 2026; accepted for publication May 11, 2026;
published online June 17, 2026.

JOURNAL OF THEORETICAL
AND APPLIED MECHANICS
64, 2, pp. 165–181, Warsaw 2026
https://doi.org/10.15632/jtam-pl/224523

DYNAMIC INSTABILITY ANALYSIS OF POROUS SIGMOID FUNCTIONALLY GRADED TRUNCATED CONICAL SHELLS SUBJECTED TO COMBINED PRESSURES

Xiao-lin HUANG[1], Haoyuan LIU[1], Yuting HAN[1], Yuhua WEI[1], Wei WU[2*]

[1] *School of Architecture and Transportation Engineering, Guilin University of Electronic Technology, Guilin, China*
[2] *School of Physics and Telecommunication, Yulin Normal University, Yulin, China*
*corresponding author, *hxl-68@163.com*

An improved model for assessing the material properties of porous sigmoid functionally graded (S-FGM) conical shells is introduced. Governing equations are derived within thin-shell theory, incorporating static hydraulic pressure, axial periodic loading, and a Winkler–Pasternak foundation. Critical frequencies and unstable regions are obtained via the Galerkin and Bolotin methods. Parametric studies show that the critical frequency decreases with higher porosity, half-vertex angle, or radius-thickness ratio, but increases with ceramic content or foundation stiffness. Porosity fraction and static axial loading notably affect instability regions, while hydraulic pressure has a negligible effect.

Keywords: dynamic stability; buckling; conical shell; sigmoid functionally graded materials; pores.

1. Introduction

Due to their outstanding advantages of light weight, high strength, and high temperature resistance, functionally graded materials (FGMs) have been applied in various engineering structures. Over the past two decades, the stability analysis of FGM shell structures has attracted substantial research attention. Sofiyev (2009; 2016) conducted extensive investigations to analyze the stability of FGM truncated conical shells subjected to various loads and resting on elastic foundations. They found that the material volume fraction, foundation parameters, half-vertex angle, radius-to-thickness ratio, length-to-radius ratio, and environmental temperature exert remarkable effects on buckling pressures. Naj *et al.* (2008) carried out an investigation into the thermal and mechanical instability of FGM conical shells. The results demonstrated that the critical buckling temperature decreases with the increase in the half-vertex angle and ratios of radius to thickness and length to thickness. Also, the discrepancies in the critical temperatures between an FGM and a homogeneous conical shell were discussed in detail. Zhang and Li (2010) explored the dynamic buckling responses of FGM truncated conical shells under normal impact loads. The results illustrated that the material gradient index imposes a significant influence on the critical buckling load. Duc *et al.* (2018) employed the Galerkin integral method combined with the smeared stiffener technique to examine the stability of stiffened FGM conical shells under mechanical loads and surrounded by elastic media. They found that FGM stiffeners improve shell stability far more effectively than homogeneous stiffeners. To address the nonlinear dynamic buckling of FGM toroidal shell segments, Ali and Hasan (2019) utilized Galerkin's integral technique, the Budiansky–Roth criterion, and the Runge–Kutta iterative approach to determine the nonlinear static and dynamic buckling loads. It was revealed that a higher loading velocity leads to a larger critical buckling load. Fan *et al.* (2021) studied the dynamic stability of magnetostrictive-face-bonded FGM conical microshells while accounting for nonlinear cubic stiffness and viscoelastic foundation effects. The results showed that the natural frequency rises within the prebuckling region under a fixed axial load. In contrast, it was reduced in the postbuckling domain. Yuan *et al.* (2021) investigated the dynamic stability of FGM conical microshells combined with magnetostrictive facesheets. They found that a larger material gradient index reduces the natural frequency in the prebuckling stage. Moreover, Nemati and Mahmoodabadi (2020) analyzed how different micromechanical models affect the stability of FGM conical panels exposed to various thermal fields. Despite abundant existing research focusing on the buckling analysis of FGM conical shells, studies concerning their dynamic stability are relatively scarce.

All the above-cited literature assumes that shell structures are perfect and free of internal pores. In reality, internal pores are inevitably generated inside material substrates (Mallek *et al.*, 2025; Wu *et al.*, 2020; Zhu *et al.*, 2001). Consequently, some studies have been conducted to examine how these internal pores affect the stability of FGM conical shells. Allahkarami *et al.* (2020) integrated the generalized differential quadrature method with Bolotin's approach to determine the dynamic instability region of a bi-directional FGM truncated conical shell, in which multiple boundary conditions and elastic foundations were taken into consideration. Fu *et al.* (2021) quantified the pore effect on the upper and lower bounds of the dynamic instability regions. Hoa *et al.* (2022) discussed the impact of internal pores on the critical buckling load of FGM conical shells. All these investigations revealed that the presence of internal pores significantly influences both the critical buckling load and the dynamic instability region of porous shell structures. Another notable limitation of the material property models adopted in these papers lies in their questionable basic assumption: they presume the pore volume fraction is sufficiently small and can be neglected when calculating the total volume of shell components.

Sigmoid functionally graded materials (S-FGMs) are advanced subclasses of FGMs, distinguished by their distinctive three-layer ceramic–metal–ceramic gradient configuration, in which the material fractions vary smoothly along the thickness direction following a sigmoid function (Chi & Chung, 2006). Unlike conventional FGM, S-FGM proves to be particularly effective in alleviating stress concentrations at interfaces where material properties would otherwise change abruptly, thereby remarkably enhancing structural integrity under various loading conditions. Due to these superior advantages, S-FGM truncated conical shells are increasingly considered for critical applications in aerospace, marine, and mechanical engineering such as rocket adapters, submarine pressure hulls, and aircraft fuselage components where lightweight design and high load-bearing capacity are paramount. In these demanding applications, the structures are frequently subjected to complex combined loads such as axial compression, external pressure, and thermal loads. Therefore, a thorough understanding of the buckling and dynamic characteristics of porous S-FGM conical shells under such conditions is essential for reliable and damage-tolerant engineering design. However, despite their evident practical significance, only a handful of publications have reported the static and dynamic mechanical behaviors of S-FGM truncated conical shells, particularly regarding dynamic stability analysis under combined loads (Bich & Ninh, 2016; Duc & Cong, 2015; Foroutan & Torabi, 2026; Pal *et al.*, 2025).

The foregoing literature review reveals that research regarding the dynamic stability of S-FGM conical shells is still limited. To the best knowledge of the authors, no previous study has explored the dynamic stability of porous S-FGM truncated shells, especially those with specific pore distribution patterns and under combined multi-type loads. Additionally, the literature review demonstrates that the previous model for assessing the properties of porous S-FGM materials overlooked the influence of the porosity volume on the total volume of S-FGM shells. To fill these research gaps, the present study proposes an improved model for S-FGM material properties and conducts a systematic analysis of the dynamic stability characteristics of porous S-FGM truncated conical shells under simply supported boundary conditions, subjected to combined static hydraulic pressure, axial periodic loading, and a Winkler–Pasternak elastic foundation.

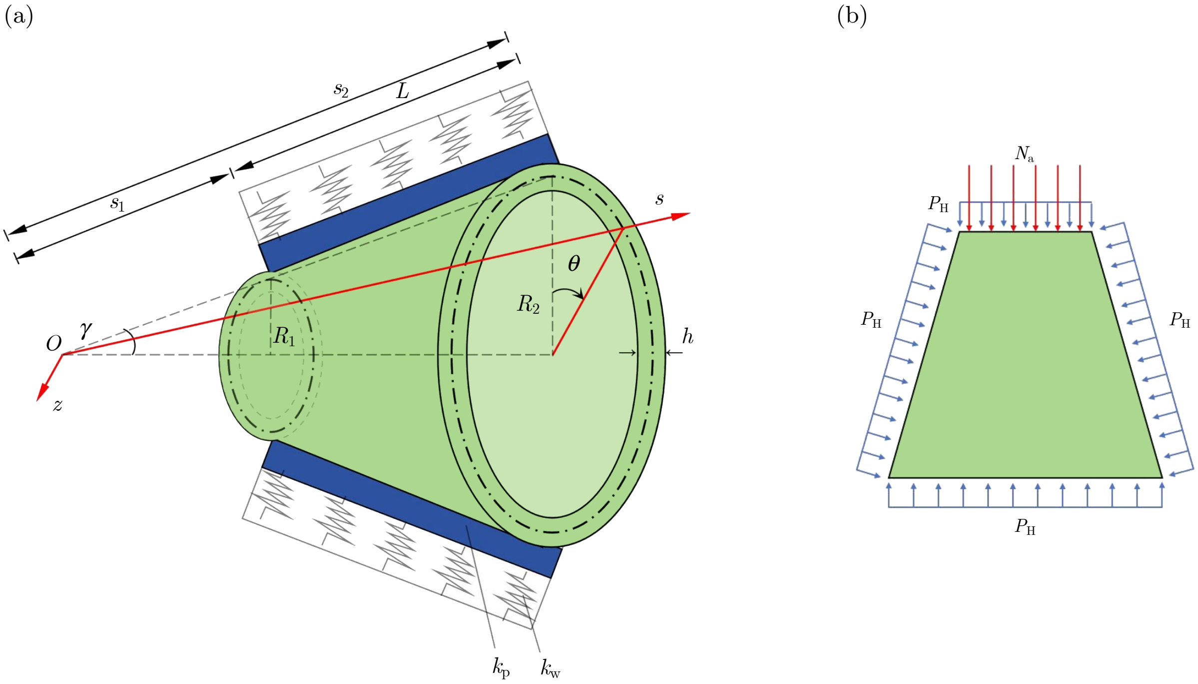

Fig. 1. S-FGM truncated conical shell surrounded by (a) an elastic medium and subjected to (b) hydraulic and axial pressures.

2. Theory analysis

Consider an S-FGM truncated conical thin shell composed of ceramic and metal, as depicted in Fig. 1. The shell is subjected to a static hydraulic pressure P_H along with a periodic axial pressure N_a. A curvilinear coordinate system (s, Θ, z) is introduced on the middle surface, where s denotes the meridional distance from the virtual apex, θ is the circumferential coordinate (positive clockwise viewed from the apex), and z is the inward normal coordinate. Let s_1 and s_2 be the distances from the virtual apex to the mid-surface of the smaller and larger bases, with corresponding radii R_1 and R_2, respectively. The geometric parameters L, h, and γ represent the length, thickness, and half-cone angle of the shell.

It is assumed the shell is supported by a Winkler–Pasternak foundation. By introducing the variable $\psi = \theta sin\gamma$, the reaction of the foundation to the shell is calculated as

$$p_\mathrm{f} = k_\mathrm{w} W - k_\mathrm{p}\left(\frac{\partial^2 W}{\partial s^2} + \frac{1}{s}\frac{\partial^2 W}{\partial s \partial \psi} + \frac{1}{s^2}\frac{\partial^2 W}{\partial \psi^2}\right), \tag{2.1}$$

in which p_f is the force per unit area, k_w and k_p are the parameters of the Winkler foundation normal stiffness and the Pasternak foundation shear stiffness, respectively. Additionally, W is the displacement along the thickness direction.

According to Hooke's law and the linear strain-displacement relationship of the shell, the normal stresses σ_s, σ_θ, and shear stress $\sigma_{z\theta}$ of the shell are given by Eq. (2.2):

$$\begin{pmatrix} \sigma_s \\ \sigma_\theta \\ \sigma_{s\theta} \end{pmatrix} = \frac{\widehat{E}(z)}{1 - \widehat{\nu}^2(z)} \begin{bmatrix} 1 & \widehat{\nu}(z) & 0 \\ \widehat{\nu}(z) & 1 & 0 \\ 0 & 0 & \dfrac{1 - \widehat{\nu}(z)}{2} \end{bmatrix} \times \begin{bmatrix} \varepsilon_s - z\dfrac{\partial^2 W}{\partial s^2} \\ \varepsilon_\theta - z\left(\dfrac{1}{s^2}\dfrac{\partial^2 W}{\partial \psi^2} + \dfrac{1}{s}\dfrac{\partial W}{\partial s}\right) \\ \varepsilon_{s\theta} - z\left(\dfrac{1}{s}\dfrac{\partial^2 W}{\partial s \partial \psi} - \dfrac{1}{s^2}\dfrac{\partial W}{\partial \psi}\right) \end{bmatrix}, \tag{2.2}$$

where ε_s, ε_θ, and $\varepsilon_{s\theta}$ imply the strains in the middle curved surface, W is the normal displacement, $\widehat{E}(z)$ and $\widehat{\nu}(z)$ represent the effective elastic modulus and Poisson's ratio.

The moments M_s, M_θ, and $M_{s\theta}$ are computed as follows:

$$(M_s, M_\theta, M_{s\theta}) = \int_{-h/2}^{h/2} (\sigma_s, \sigma_\theta, \sigma_{s\theta}) z dz. \tag{2.3}$$

The membrane forces N_s, N_θ, and $N_{s\theta}$ can be computed using the Airy function F as

$$(N_s, N_\theta, N_{s\theta}) = \left(\frac{1}{s^2}\frac{\partial^2 F}{\partial\psi^2} + \frac{1}{s}\frac{\partial F}{\partial s}, \quad \frac{\partial^2 F}{\partial s^2}, \quad -\frac{1}{s}\frac{\partial^2 F}{\partial s\partial\psi} + \frac{1}{s^2}\frac{\partial F}{\partial\psi}\right). \tag{2.4}$$

In this research, some internal pores are assumed to exist in the shell. As depicted in Fig. 2, the even and uneven distributions are taken into account.

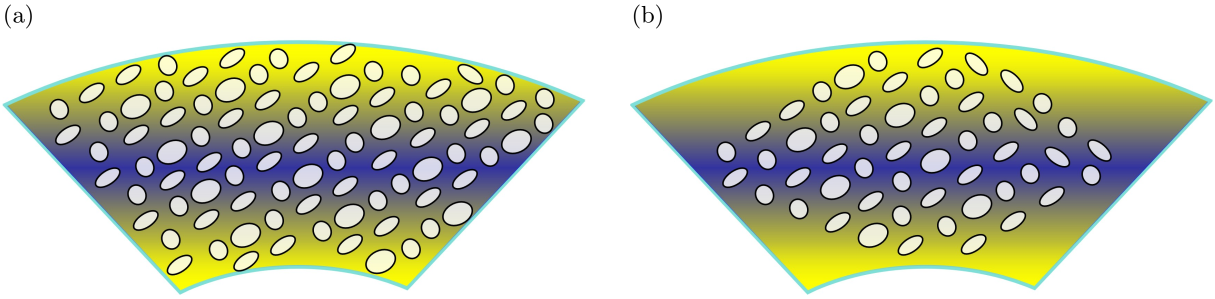

Fig. 2. Porosity distribution: (a) even distribution; (b) uneven distribution.

In the previous research on porous FGM structures, the porosity volume fraction $\overline{\alpha}$ is usually regarded as a tiny variable ($\overline{\alpha} \ll 1$). Hence, $\overline{\alpha}$ can be neglected, and the total volume of porous structures is computed as $\overline{V}_{\mathrm{c}} + \overline{V}_{\mathrm{m}} = 1$, where $\overline{V}_{\mathrm{c}}$ and $\overline{V}_{\mathrm{m}}$ are the total volume fractions of ceramic and metal, respectively. However, the assumption is inaccurate. To remove the assumption, the equations of computing the total volume and mass fractions of the shell are introduced as $\overline{V}_{\mathrm{c}} + \overline{V}_{\mathrm{m}} + \overline{\alpha} = 1$ and $W_{\mathrm{c}} + W_{\mathrm{m}} = 1$, where W_{c} and W_{m} imply the mass fractions of ceramic and metal. Thus, $\overline{V}_{\mathrm{c}}$ can be calculated by

$$\overline{V_{\mathrm{c}}} = (1 - \overline{\alpha})\frac{W_{\mathrm{c}}/\rho_{\mathrm{c}}}{W_{\mathrm{c}}/\rho_{\mathrm{c}} + W_{\mathrm{m}}/\rho_{\mathrm{m}}}, \tag{2.5}$$

where ρ_{c} and ρ_{m} imply the mass densities of ceramic and metal, respectively.

The ceramic volume fraction $V_{\mathrm{c}}(z)$ for S-FGM is supposed to be (Duc & Cong, 2015; Naj *et al.*, 2008):

$$V_{\mathrm{c}}(z) = \begin{cases} V_{\mathrm{c1}}^* \left(1 - \frac{1}{2}\left(1 - \dfrac{2z}{h}\right)^N\right), & (0 \le z \le h/2), \\ \frac{1}{2}V_{\mathrm{c1}}^* \left(1 + \dfrac{2z}{h}\right)^N, & (-h/2 \le z \le 0), \end{cases} \tag{2.6}$$

and that for typical FGMs is given by

$$V_{\mathrm{c}}(z) = V_{\mathrm{c2}}^* \left(1 + \frac{2z}{h}\right)^N, \tag{2.7}$$

where N is the volume fraction index.

Assuming that the total ceramic volume is equivalent for the two porosity distributions, the coefficients V^*_{c1} and V^*_{c2} can be determined by

$$\int\limits_{-h/2}^{0} \frac{1}{2}V^*_{\mathrm{c}_1}\left(1+\frac{2z}{h}\right)^N dz + \int\limits_{0}^{h/2} V^*_{\mathrm{c}_1}\left[1-\frac{1}{2}\left(1-\frac{2z}{h}\right)^N\right] dz = \overline{V}_{\mathrm{c}}h, \tag{2.8}$$

$$\int\limits_{-h/2}^{h/2} V^*_{\mathrm{c}_2}\left(1+\frac{2z}{h}\right)^N dz = \overline{V}_{\mathrm{c}}h. \tag{2.9}$$

Following the rule of mixtures, the effective values of the elastic modulus $\widehat{E}(z)$, mass density $\widehat{\rho}(z)$, and Poisson's ratio $\widehat{\nu}(z)$ are given by

$$\widehat{E}(z) = E_{\mathrm{c}}V_{\mathrm{c}}(z) + E_{\mathrm{m}}\big(1 - V_{\mathrm{c}}(z) - \alpha(z)\big), \tag{2.10}$$

$$\widehat{\rho}(z) = \rho_{\mathrm{c}}V_{\mathrm{c}}(z) + \rho_{\mathrm{m}}\big(1 - V_{\mathrm{c}}(z) - \alpha(z)\big), \tag{2.11}$$

$$\widehat{\nu}(z) = \nu_{\mathrm{c}}V_{\mathrm{c}}(z) + \nu_{\mathrm{m}}\big(1 - V_{\mathrm{c}}(z) - \alpha(z)\big), \tag{2.12}$$

where E_{c} and ν_{c} represent the elastic modulus and Poisson's ratio of the ceramic, respectively, while E_{m} and ν_{m} denote those of the metal. In the case of both even (ED) and uneven (UD) porosity distributions, the volume distribution $\alpha(z)$ is assumed to be

$$\alpha(z) = \overline{\alpha}, \qquad \text{(ED)}, \tag{2.13}$$

$$\alpha(z) = \alpha^*\left(1 - \frac{2|Z|}{h}\right), \qquad \text{(UD)}. \tag{2.14}$$

It is supposed that the total porosity volumes for the two distributions are equivalent. The coefficient α^* is calculated by

$$\int\limits_{-h/2}^{h/2} \alpha^*\left(1-\frac{2|z|}{h}\right) dz = \overline{\alpha}\,h. \tag{2.15}$$

Subjected to hydraulic pressure P_{H} and periodical axial pressure N_{a} at the smaller end of the shell, the initial membrane forces of the shell can be obtained as follows (Sofiyev, 2010):

$$\begin{aligned} N_s^0 &= -0.5P_{\mathrm{H}}s\tan\gamma - 0.5N_{\mathrm{a}}s_2^2\tan\gamma/s, \\ N_\theta^0 &= -P_{\mathrm{H}}s\tan\gamma, \qquad N_{s\theta}^0 = 0. \end{aligned} \tag{2.16}$$

Employing Hamilton's principle, after a long computation, the equations of dynamic equilibrium and the deformation compatibility of the shell can be deduced as follows (Ng *et al.*, 2001; Sofiyev & Schnack, 2012):

$$\begin{aligned} &\frac{\partial^2 M_s}{\partial s^2} + \frac{2}{s}\frac{\partial M_s}{\partial s} + \frac{2}{s}\frac{\partial^2 M_{s\theta}}{\partial s\partial\psi} - \frac{1}{s}\frac{\partial M_\theta}{\partial s} + \frac{2}{s^2}\frac{\partial M_{s\theta}}{\partial\psi} + \frac{1}{s^2}\frac{\partial^2 M_\theta}{\partial\psi^2} + \frac{N_\theta}{s}\cot\gamma \\ &\quad + \frac{N_\theta^0}{s}\left(\frac{1}{s}\frac{\partial^2 W}{\partial\psi^2} + \frac{\partial W}{\partial s}\right) + N_s^0\frac{\partial^2 W}{\partial s^2} + 2N_{s\theta}^0\frac{\partial}{\partial s}\left(\frac{1}{s}\frac{\partial W}{\partial\psi}\right) - \rho_{\mathrm{f}}h\frac{\partial^2 W}{\partial t^2} \\ &\quad - k_{\mathrm{w}}W + k_{\mathrm{p}}\left(\frac{\partial^2 W}{\partial s^2} + \frac{2}{s}\frac{\partial^2 W}{\partial s\partial\psi} + \frac{1}{s^2}\frac{\partial^2 W}{\partial\psi^2}\right) = 0, \end{aligned} \tag{2.17}$$

$$\frac{\cot\gamma}{s}\frac{\partial^2 W}{\partial s^2}-\frac{2}{s}\frac{\partial^2\varepsilon_{s\theta}}{\partial s\partial\psi}-\frac{2}{s^2}\frac{\partial\varepsilon_{s\theta}}{\partial\psi}+\frac{\partial^2\varepsilon_\theta}{\partial s^2}+\frac{1}{s^2}\frac{\partial^2\varepsilon_s}{\partial\psi^2}+\frac{2}{s}\frac{\partial\varepsilon_\theta}{\partial s}-\frac{1}{s}\frac{\partial\varepsilon_s}{\partial s}=0, \tag{2.18}$$

where $\rho_{\mathrm{f}}=\int\limits_{-0.5h}^{0.5h}\widehat{\rho}(z)dz$ is the mass inertia.

Introducing two variables $x=\ln(s/s_1)$ and $F_1=Fe^{-2x}$, then substituting Eqs. (2.2), (2.3), (2.4), and (2.16) into Eqs. (2.17) and (2.18), the governing equations of the dynamic stability for the shell can be rewritten as follows:

$$T_{11}(F_1)+T_{12}(W)+P_{\mathrm{H}}T_{13}(W)+N_{\mathrm{a}}T_{14}(W)-\rho_{\mathrm{f}}hs_1^4e^{4x}\frac{\partial^2 W}{\partial t^2}=0, \tag{2.19}$$

$$T_{21}(F_1)+T_{22}(W)=0, \tag{2.20}$$

in which the differential operators $T_{ij}(\ )$ are given in Appendix (A.1).

The two bases of the shell are supposed to be simply supported. The boundary conditions can be written as

$$s=s_1,\ s_2:\quad W=M_s=0. \tag{2.21}$$

The satisfaction of boundary conditions requires that the displacements W take the form:

$$W=\sum_m\sum_n w_{mn}(t)e^x\sin(\beta_1 x)\sin(\beta_2\psi), \tag{2.22}$$

where the coefficients β_1 and β_2 are defined by

$$\beta_1=\frac{m\pi}{x_0},\qquad \beta_2=\frac{n}{\sin\gamma},\qquad x_0=\ln(s_2/s_1), \tag{2.23}$$

in which m and n represent the meridional half and circumferential wave numbers, respectively.

Substituting Eq. (2.22) into Eq. (2.20), then employing the superposition principle, the Airy function F_1 can be obtained as

$$F_1=\sum_m\sum_n f_{mn}(t)(\mu_1\sin\beta_1 x+\mu_2\cos\beta_1 x+\mu_3e^{-x}\sin\beta_1 x+\mu_4e^{-x}\cos\beta_1 x)\sin\beta_2\psi, \tag{2.24}$$

in which $\mu_i(i=1-4)$ are the constant coefficients.

The axial periodic pressure N_{a} is assumed to be

$$N_{\mathrm{a}}(t)=N_0(\mu_{\mathrm{s}}+\mu_{\mathrm{d}}\cos\varphi t), \tag{2.25}$$

where μ_{s} and μ_{d} represent the static and dynamic coefficients of the periodical pressure, φ is the excitation frequency.

Substituting Eqs. (2.22), (2.24), and (2.25) into Eq. (2.19), then multiplying Eq. (2.19) by $\sin\beta_1 x\sin\beta_2\psi$ and using Galerkin's integral technique in the ranges $0\le\psi\le 2\pi\sin\gamma$ and $0\le x\le x_0$, the differential equations can be deduced as follows:

$$\mathbf{M}\ddot{\chi}+(\mathbf{K}_0+P_{\mathrm{H}}\mathbf{K}_{\mathrm{P}}+\mu_{\mathrm{s}}N_0\mathbf{K}_{\mathrm{G}})\chi+(\mu_{\mathrm{d}}N_0\mathbf{K}_{\mathrm{G}}\cos\varphi\mathrm{t})\chi=0, \tag{2.26}$$

in which $\mathbf{M}$, $\mathbf{K}_0$, $\mathbf{K}_{\mathrm{P}}$, and $\mathbf{K}_{\mathrm{G}}$ are the matrices of mass, stiffness, hydraulic pressure, and geometric stiffness. $\chi=\{w_{mn}(t)\}$ represents the displacement vector.

Let $\chi=\{A\}e^{iwt}$ and $N_0=0$. Equation (2.26) is reformed as

$$\left((\mathbf{K}_0+P_{\mathrm{H}}\mathbf{K}_{\mathrm{P}})-\omega^2\mathbf{M}\right)\chi=0. \tag{2.27}$$

Based on Eq. (2.27), the natural frequencies ω can be solved. It is noted that the frequency ω varies with hydraulic pressure P_{H}. When $\omega = 0$, the critical hydraulic pressure P_{Hcr} can be attained.

The dynamic stability of the shell can be described by the Mathieu-Hill type differential Eq.(2.26). To identify the points on the edges of unstable regions, the Bolotin method is adopted. The assumed solution of Eq. (2.26) can be expanded by using a series of trigonometric functions containing the excitation frequency φ as follows (Ng *et al.*, 2001):

$$\chi = \sum_{k=1.3\ldots} \left(f_k \sin \frac{k\varphi t}{2} + g_k \cos \frac{k\varphi t}{2} \right), \tag{2.28}$$

with period $2T$, where $T = 2\pi/\varphi$, or

$$\chi = \frac{g_0}{2} + \sum_{k=2.4\ldots} \left(f_k \sin \frac{k\varphi t}{2} + g_k \cos \frac{k\varphi t}{2} \right), \tag{2.29}$$

with period T, where $T = 2\pi/\varphi$, f_k and g_k are the constant coefficients. The principal unstable regions with $2T$ are usually wider than those with T and are of greater practical importance (Bich & Ninh, 2016). Therefore, the solutions with $2T$ are considered in this research. Substituting Eq. (2.28) into Eq. (2.26) and assembling the $\sin(k\varphi t/2)$ and $\cos(k\varphi t/2)$ terms, a group of linear homogeneous algebraic equations in terms of f_k and g_k can be deduced. In general, a solution sufficiently accurate may be found using the first-order approximation with $k = 1$. To obtain a non-trivial solution, the following conditions need to be satisfied:

$$\det \left| \left(\mathbf{K}_0 + P_{\mathrm{H}} \mathbf{K}_{\mathrm{P}} + \mu_{\mathrm{s}} N_0 \mathbf{K}_{\mathrm{G}} - \frac{1}{2} \mu_{\mathrm{d}} N_0 \mathbf{K}_{\mathrm{G}} - \frac{\varphi^2}{4} \mathbf{M} \right) \right| = 0, \tag{2.30}$$

$$\det \left| \left(\mathbf{K}_0 + P_{\mathrm{H}} \mathbf{K}_{\mathrm{P}} + \mu_{\mathrm{s}} N_0 \mathbf{K}_{\mathrm{G}} + \frac{1}{2} \mu_{\mathrm{d}} N_0 \mathbf{K}_{\mathrm{G}} - \frac{\varphi^2}{4} \mathbf{M} \right) \right| = 0. \tag{2.31}$$

If the values of the static hydraulic pressure P_{H} and axial loading $\mu_{\mathrm{s}} N_0$ are given, the two critical excitation frequencies at every dynamic pressure level $\beta = \mu_{\mathrm{d}}/\mu_{\mathrm{s}}$ can be found by solving Eqs. (2.30) and (2.31). By introducing the dimensionless external frequency $\phi = 2\pi\varphi(\rho_{\mathrm{m}}/E_{\mathrm{m}})^{0.5}$, the two curved lines in the $\phi - \beta$ plane with a common point at $\beta = 0$ form the boundary lines between the stable and unstable regions.

If $\gamma \to 0$, $s_1 \to \infty$, $s_1 \sin\gamma = R$, $\ln(s_1/s_2)\sin\gamma = R/L$, the results for a conical shell are converted into those for the corresponding cylindrical shell (Sofiyev & Schnack, 2012).

3. Results and discussion

3.1. Verification

To validate the effectiveness and accuracy of the present approach, the following three numerical examples of investigating the buckling and dynamic instability for typical FGM conical shells are presented:

Example 1. Table 1 compares the results of critical hydraulic pressure P_{Hcr} for a typical Si_3N_4/SUS304 FGM conical shell with those given by Sofiyev (2009). The elastic modulus, mass density, and Poisson's ratio for Si_3N_4 are $E_{\mathrm{c}} = 322.27\,\mathrm{GPa}$, $\rho_{\mathrm{c}} = 2370\,\mathrm{kg/m^3}$, and $\nu_{\mathrm{c}} = 0.24$, and those for SUS304 are $E_{\mathrm{m}} = 207.7877\,\mathrm{GPa}$, $\rho_{\mathrm{m}} = 8166\,\mathrm{kg/m^3}$, and $\nu_{\mathrm{m}} = 0.317756$. The adopted geometric parameters are $R_1 = 1.0\,\mathrm{m}$, $R_2 = 3.0\,\mathrm{m}$, $R_2/h = 300$, and $\gamma = 30°$. The meridional half-wave number is $m = 1$, while the circumferential wave numbers n are presented in Table 1. It is clear that the present results are almost the same as those presented by Sofiyev (2009).

Table 1. Comparison of critical hydraulic pressures $P_{\mathrm{Hcr}}(n)$ [MPa].

Method	$\mathrm{Si_3N_4}$	$N = 1.0$	$N = 2.0$	SUS304
Sofiyev (2009)	0.257(8)	0.200(8)	0.191(8)	0.155(7)
Present	0.253(8)	0.197(8)	0.187(8)	0.153(7)

Example 2. The dimensionless fundamental frequency Ω for a typical $\mathrm{Si_3N_4}$/Ni FGM conical shell encircled by Winkler–Pasternak elastic medium is shown in Table 2. The material properties for $\mathrm{Si_3N_4}$ are $E_{\mathrm{c}} = 322.27\,\mathrm{GPa}$, $\rho_{\mathrm{c}} = 2370\,\mathrm{kg/m^3}$, and $\nu_{\mathrm{c}} = 0.24$, and those for Ni are $E_{\mathrm{m}} = 205.098\,\mathrm{GPa}$, $\rho_{\mathrm{m}} = 8900\,\mathrm{kg/m^3}$, and $\nu_{\mathrm{m}} = 0.31$. The geometric dimensions are $R_2/h = 100$, $L = 2R_1$, and $\gamma = 30°$. The dimensionless fundamental frequency is defined as $\Omega = \omega R_2 \left((1-\nu_{\mathrm{c}}^2)\rho_{\mathrm{c}}/E_{\mathrm{c}}\right)^{0.5}$. The table illustrates that the present results are very similar to those of Sofiyev *et al.* (2012).

Table 2. Comparison of natural frequency parameter $\Omega(n)$.

k_{w} [N/m^3]	k_{p} [N/m]	Method	Ni	$N = 1.0$	$N = 2.0$	$\mathrm{Si_3N_4}$
0	0	Sofiyev *et al.* (2012)	0.0723(7)	0.0997(7)	0.0887(7)	0.1763(7)
		Present	0.0725(7)	0.1001(7)	0.0891(7)	0.1771(7)
5×10^6	0	Sofiyev *et al.* (2012)	0.0813(7)	0.1103(7)	0.0988(7)	0.1910(7)
		Present	0.0816(7)	0.1112(7)	0.1003(7)	0.1918(7)
5×10^6	2.5×10^5	Sofiyev *et al.* (2012)	0.0888(7)	0.1198(6)	0.1072(6)	0.2046(6)
		Present	0.0892(7)	0.1210(6)	0.1083(6)	0.2061(6)

Example 3. The dimensionless critical excitation frequency $\overline{\phi^*}$ at $\beta = 0$ and for a typical $\mathrm{Si_3N_4}$/Ni FGM cylindrical shell under axial dynamic pressure $N_0 = 0.5N_{\mathrm{cr}}$ are listed in Table 3. The material properties are $E_{\mathrm{c}} = 322.27\,\mathrm{GPa}$, $\rho_{\mathrm{c}} = 2370\,\mathrm{kg/m^3}$, and $\nu_{\mathrm{c}} = 0.24$ for $\mathrm{Si_3N_4}$, and those for Ni are $E_{\mathrm{m}} = 205.098\,\mathrm{GPa}$, $\rho_{\mathrm{m}} = 8900\,\mathrm{kg/m^3}$, and $\nu_{\mathrm{m}} = 0.31$. The critical axial pressure is $N_{\mathrm{cr}} = \frac{E_{\mathrm{m}}h^2}{R\left(3(1-\nu_{\mathrm{m}}^2)\right)^{0.5}}$, and the dimensionless critical excitation frequency is defined by $\overline{\phi^*} = 2\pi R\varphi(\rho_{\mathrm{c}}/A_{11})^{0.5}$. The transverse mode (m, n) is $(1, 1)$, and the material parameters for $\mathrm{Si_3N_4}$ and Ni are the same as those in Example 2. The geometric parameters are $R/h = 100$ and $L/R = 1.0$. It is revealed that the present results are very close to those in (Ng *et al.*, 2001).

Table 3. Comparison of dimensionless critical excitation frequency $\overline{\phi^*}$.

Method	$N = 0$	$N = 0.5$	$N = 1$	$N = 5$	$N = 10$
Ng *et al.* (2001)	10.3932	10.5262	10.5831	10.6736	10.6899
Present	10.4133	10.5507	10.6126	10.7031	10.7052

3.2. Parametric studies

This subsection investigates the influences of internal pores, material constitution, elastic medium, hydraulic pressure, and geometric parameters on the dynamic stability of a porous $\mathrm{Si_3N_4}$/SUS304 S-FGM conical shell. The material parameters are the same as in Example 1. The hydraulic pressure and the amplitude of dynamic loading are, respectively:

$$P_{\mathrm{H}} = 2.96\mu_{\mathrm{H}}\frac{E_{\mathrm{m}}h}{s_2(1-\nu_{\mathrm{m}}^2)^{0.75}}\left(\frac{h}{s_2\tan\gamma}\right)^{1.3}\left(1 - 0.78\left(\frac{h}{s_2\tan\gamma}\right)^{0.5} + 0.38\frac{h}{s_2\tan\gamma}\right)$$

and

$$N_0 = \frac{E_{\rm m} h^2}{R\left[3\left(1-\nu_{\rm m}^2\right)\right]^{0.5}}.$$

The dimensionless excitation frequency is defined as $\phi = 2\pi\varphi(\rho_{\rm m}/E_{\rm m})^{0.5}$. Unless otherwise stated, the following parameters are adopted: $W_{\rm c} = 0.2$, $\overline{\alpha} = 0.1$, $N = 1.0$, $\gamma = 30°$, $h = 0.01\,{\rm m}$, $R_1/h = 100$, $L/R_1 = 1.0$, $k_{\rm w} = 1.0 \times 10^7\,{\rm N/m^3}$, $k_{\rm p} = 2.5 \times 10^5\,{\rm N/m}$, $\mu_{\rm H} = 0.5$, $\mu_{\rm s} = 0.5$.

In each unstable region, the boundaries are defined by two lines that originate from a common point on the ϕ-axis. Although these lines appear straight, they are actually very slightly curved. To quantify the size of the unstable region, Ng *et al.* (2001) proposed the subtended angle Θ, as illustrated in Fig. 3. The angle Θ is calculated using the arctangent of the right-angled triangle $\angle AOB$. It provides an accurate measure of the slope of the boundaries of the unstable region, based on calculations involving a similar triangle $\angle A^*OB^*$. Evidently, a larger Θ indicates a wider unsafe frequency band, and ϕ^* denotes the critical excitation frequency at $\beta = 0$. Physically, stable regions correspond to decaying vibrations, while unstable regions imply parametric resonance with exponentially growing amplitudes that risk fatigue or failure.

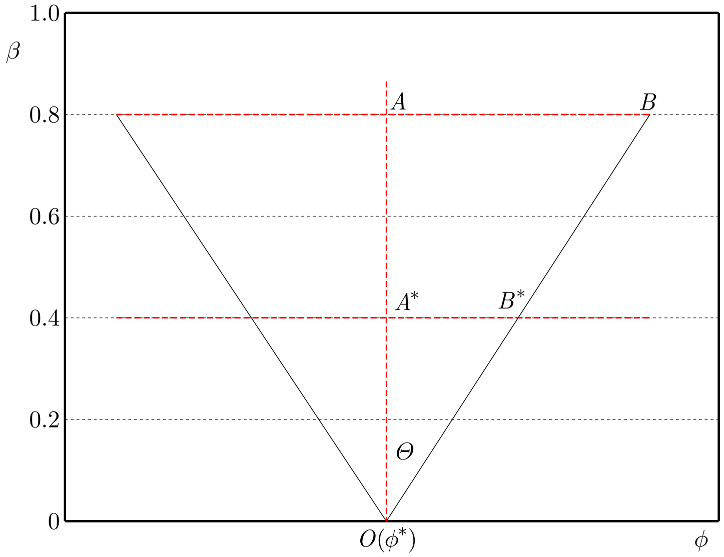

Fig. 3. Unstable region in the $\phi - \beta$ plane.

Figure 4 shows that increasing the wave number n can reduce the value of the critical excitation frequency ϕ^*. As the wave number n changes from 1 to 5, the critical frequency ϕ^* declines from 5.850 to 1.304, and the subtended angle Θ also declines from 31.38° to 8.32°. The change demonstrates that the stability for a lower mode (m, n) is higher than that for a higher mode (m, n).

Figure 5 reveals the influence of porosity distributions. It is found that the critical excitation frequency ϕ^* for UD is higher than that for ED. However, the subtended angle Θ is almost unchanged. This is because the pores for UD are more distributed in the middle area of the conical shell. The stiffness for UD is higher than that for ED.

The influence of the porosity volume fraction $\overline{\alpha}$ is revealed in Fig. 6. Since increasing $\overline{\alpha}$ leads to the lower effective stiffness, the critical excitation frequency ϕ decreases, and the unstable region is expanded. When $\overline{\alpha}$ increases from 0.0 to 0.3, the excitation frequency ϕ^* declines from 5.876 to 5.787. In contrast, the subtended angle Θ rises from 7.56° to 10.86°. Hence, internal pores should be diminished to improve the dynamic stability of the shell in making S-FGMs.

Figure 7 illustrates the influence of the ceramic mass fraction $W_{\rm c}$ on the dynamic stability. If the mass fraction $W_{\rm c}$ changes in the range of 0.1 to 0.3, the critical excitation frequency ϕ^* increases from 5.319 to 6.212. Since the elastic modulus of Si_3N_4 is larger than that

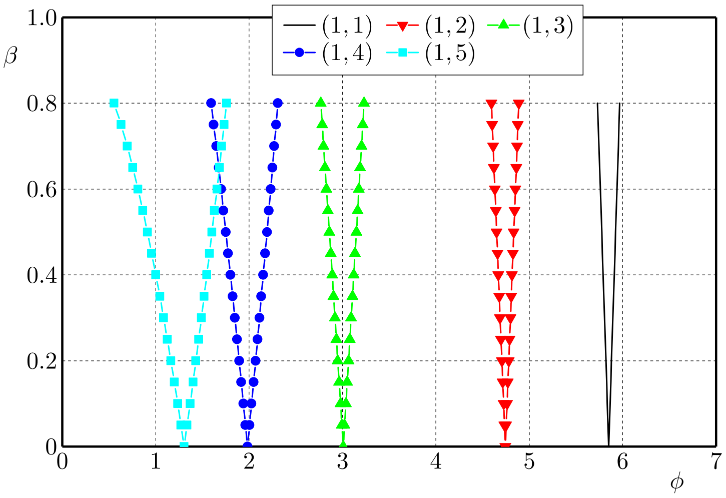

Fig. 4. Influence of transverse modes (m, n) on the dynamic stability of a porous S-FGM conical shell.

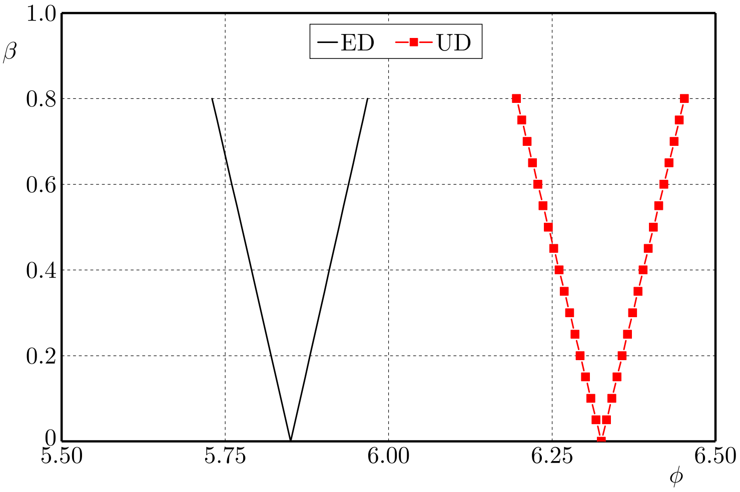

Fig. 5. Influence of porosity distribution on the dynamic stability of a porous S-FGM conical shell.

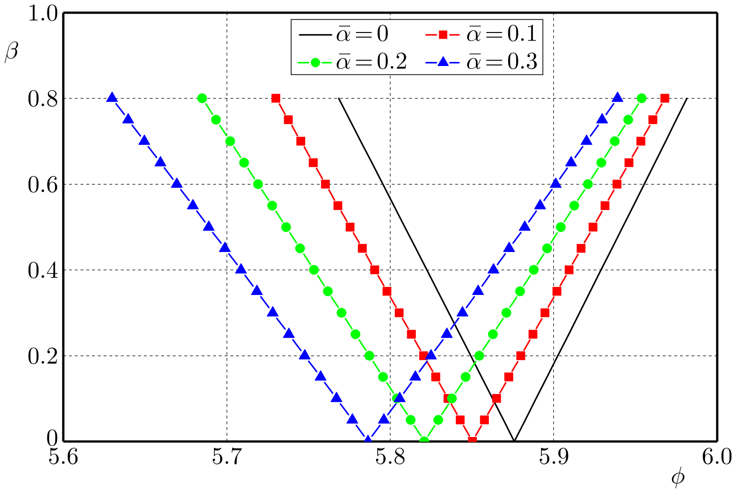

Fig. 6. Influence of porosity volume fraction on the dynamic stability of a porous S-FGM conical shell.

of SUS304, increasing W_c results in the rise of the effective stiffness. Also, the figure shows that the impact of the ceramic mass fraction W_c on the unstable region is insignificant and may be neglected.

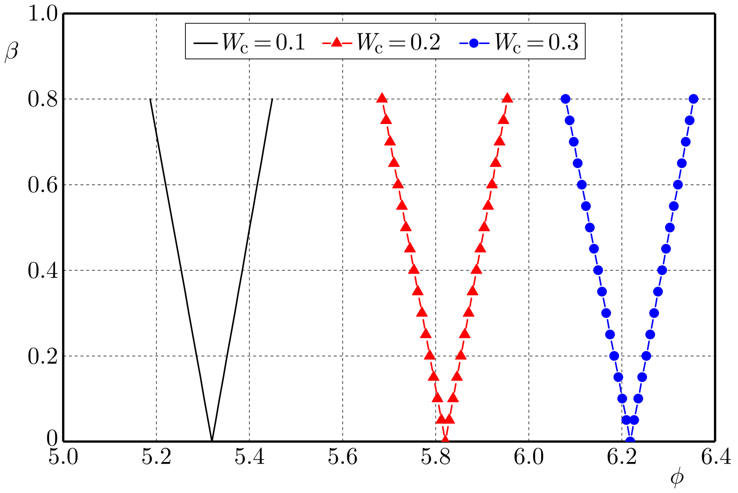

Fig. 7. Influence of ceramic mass fraction W_c on the dynamic stability for a porous S-FGM conical shell.

Figure 8 and Fig. 9 reveal the influences of the hydraulic and axial pressures, respectively. It can be observed that the influence of the hydraulic pressure on the dynamic stability may be neglected. Compared with the influence of the hydraulic pressure, that of the axial static

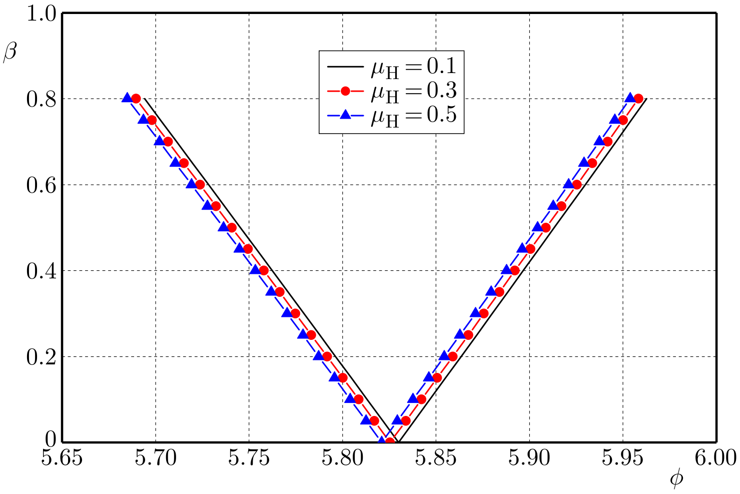

Fig. 8. Influence of hydraulic pressure on the dynamic stability for a porous S-FGM conical shell.

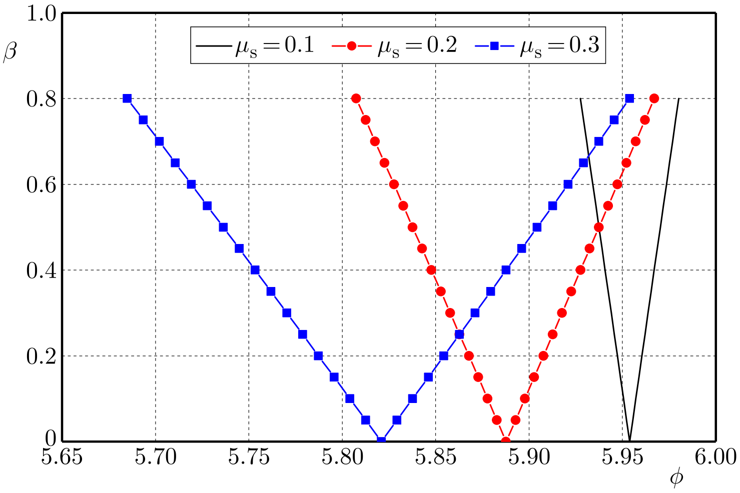

Fig. 9. Influence of the static axial pressure on the dynamic stability for a porous S-FGM conical shell.

loading is more significant. When the axial loading coefficient μ_s rises from 0.1 to 0.3, the critical excitation frequency ϕ^* declines from 5.954 to 5.821, and the subtended angle Θ increases from 1.88° to 9.48°. It is because the axial loading significantly weakens the effective stiffness, which leads to the decrease in the critical excitation frequency.

The influence of the fraction index N on the dynamic stability is illustrated in Fig. 10. From the figure, it can be observed that increasing the index N makes the critical excitation frequency ϕ^* decline. On the contrary, the subtended angle Θ declines with the increasing fraction index N. That is because the elastic modulus of Si_3N_4 is higher than that of SUS304, while its density is lower than that of Ni. Thus, the critical excitation frequency ϕ^* is decreased if the index N rises.

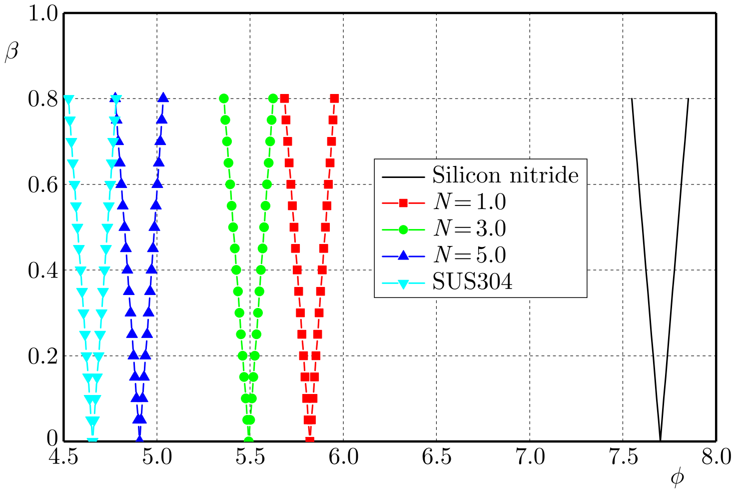

Fig. 10. Influence of the material fraction index N on the dynamic stability for a porous S-FGM conical shell.

Figure 11 reveals the influence of the elastic media, including the Winkler elastic medium ($k_w \neq 0$, $k_p = 0$), Pasternak elastic medium ($k_w = 0$, $k_p \neq 0$), and Winkler–Pasternak elastic medium ($k_w \neq 0$, $k_p \neq 0$). Since the effective stiffness can be enhanced by increasing the values of these parameters, it is seen that increasing these parameters makes the critical excitation frequency ϕ^* rise. However, the effect of the elastic medium parameters on the subtended angle Θ is very small and may be neglected.

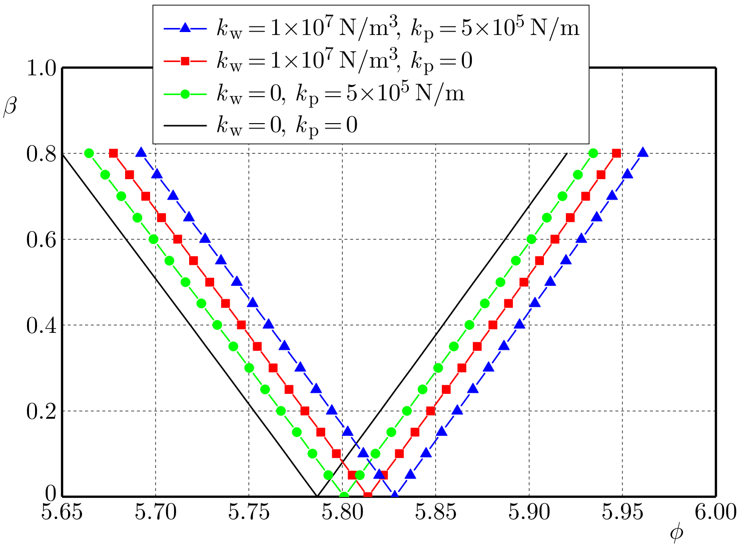

Fig. 11. Influence of elastic medium on the dynamic stability for a porous S-FGM conical shell.

The influences of the shell parameters, including half-vertex angle γ and the ratios R_1/h and L/R_1, on the dynamic stability are presented in Fig. 12, Fig. 13, and Fig. 14. In Fig. 12, it is illustrated that increasing the angle γ makes the critical excitation frequency ϕ^* decline. However,

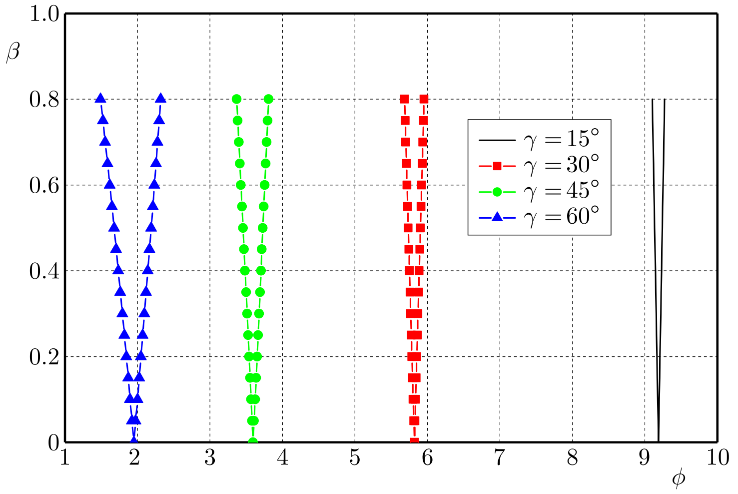

Fig. 12. Influence of the half-vertex angle γ on the dynamic stability for a porous S-FGM conical shell.

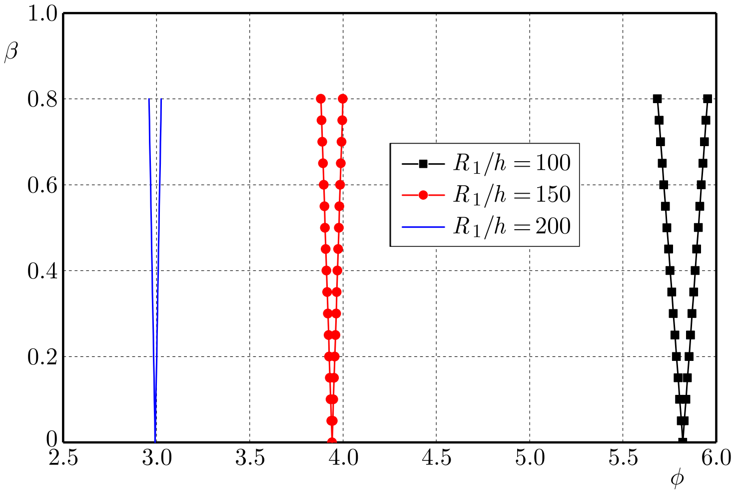

Fig. 13. Influence of the ratio R_1/h on the dynamic stability for a porous S-FGM conical shell.

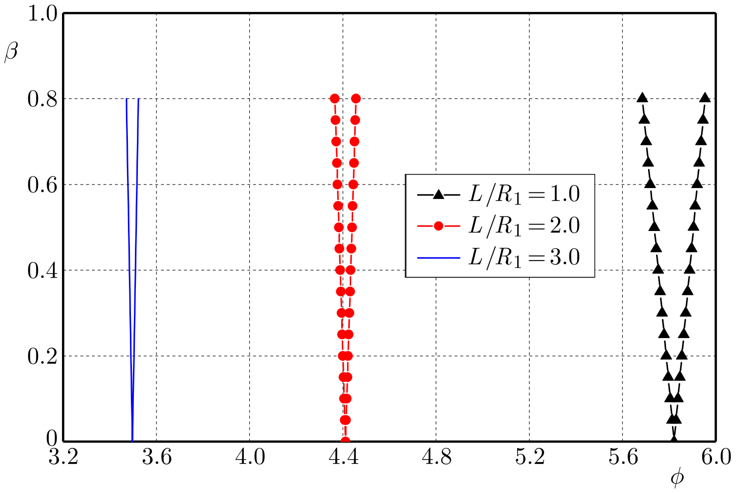

Fig. 14. Influence of the ratio L/R_1 on the dynamic stability for a porous S-FGM conical shell.

the subtended angle Θ increases as the half-vertex angle γ rises. The changes demonstrate that increasing γ can weaken the dynamic stability of the shell.

As shown in Fig. 13, the critical excitation frequency ϕ^* decreases with the rising ratio R_1/h. If the ratio R_1/h rises from 100 to 200, the frequency ϕ^* decreases from 5.820 to 3.941, whereas Θ increases from 9.53° to 39.43°. It is because the effective stiffness for a thick shell is larger than that for a thin shell. In addition, the impact of the ratio L/R_1 on the dynamic stability is revealed in Fig. 14. It is shown that the critical excitation frequency ϕ^* decreases from 5.821 to 3.497 as the L/R_1 changes from 1.0 to 3.0. However, the subtended angle Θ reduces from 2.93° to 1.83° when the ratio L/R_1 rises from 1.0 to 3.0. It is illustrated that a short conical shell is more stable than a slender shell.

4. Conclusion and future work

This study develops an improved and reliable material parameter calculation model for porous sigmoid functionally graded materials (S-FGMs), which breaks through the traditional assumption that the porosity volume fraction is negligible in the volume calculation of FGM structures. Within a general linear dynamic stability framework, the governing equations for porous S-FGM truncated conical shells surrounded by a Winkler–Pasternak elastic medium and subjected to the combined action of static hydraulic pressure and periodic axial pressure are rigorously derived based on thin shell theory. By combining the Galerkin integral method with the Bolotin method, the critical excitation frequency ϕ^* and subtended angle Θ of the shells are accurately solved. A systematic parametric study is then conducted to reveal the influence laws and intrinsic mechanisms of key parameters. It is noteworthy that while the subsequent quantitative results are obtained for a specific set of parameters, the analytical model and solution procedure established herein are universal and can be directly applied to a wider range of engineering problems involving similar porous functionally graded shell structures. The study reveals the shifts of dynamic stability boundaries in the parameter space. Within the examined parameter ranges, the key conclusions are drawn as follows:

(i) Internal pores significantly affect the location and width of the unstable regions. Increasing the porosity volume fraction $\overline{\alpha}$ shifts the critical excitation frequency ϕ^* towards lower values, while it broadens the unstable region by increasing the subtended angle Θ.

(ii) Increasing the ceramic mass fraction W_c shifts the dynamic stability boundary towards higher excitation frequencies, causing ϕ^* to rise significantly. However, the impact of W_c on the subtended angle Θ is negligible within the studied range.

(iii) The value of the critical excitation frequency ϕ^* can be decreased by increasing the half-vertex angle γ and the ratios R_1/h and L/R_1. In contrast to the ratios R_1/h and L/R_1, an increase in the half-vertex angle γ can enhance the value of the subtended angle Θ.

In general, based on the linear dynamic stability framework, this study uncovers the basic dynamic stability characteristics and the action mechanisms of key parameters of porous S-FGM truncated conical shells under combined loads. The established material parameter model, dynamic stability governing equations, and solution methodology provide a solid theoretical basis for the dynamic stability analysis of this novel gradient porous shell structure. Meanwhile, this research is restricted to linear analysis, simplified porosity models, single boundary and load conditions, as well as linear elastic constitutive assumptions, which clearly points out the direction for subsequent in-depth research. Future studies may focus on nonlinear dynamic stability analysis, improvement of the pore microscopic model, expansion of complex engineering conditions, optimization of the material constitutive model, and experimental verification, so as to further improve the dynamic stability analysis system of porous S-FGM truncated conical shells.

Appendix

In Eqs. (2.19) and (2.20), the differential operators $T_{ij}(\ )$ are defined as

$$
\begin{aligned}
T_{11}(F_1) = {} & A_2 e^{2x}\left(\frac{\partial^4 F_1}{\partial x^4} - 4\frac{\partial^3 F_1}{\partial x^3} + 4\frac{\partial^2 F_1}{\partial x^2} + 2\frac{\partial^2 F_1}{\partial \psi^2} + \frac{\partial^4 F_1}{\partial \psi^4}\right)\\
& + s_1 e^{3x}\cot\gamma\left(\frac{\partial^2 F_1}{\partial x^2} + 3\frac{\partial F_1}{\partial x} + 2F_1\right)\\
& + 2(A_1 - A_5)e^{2x}\left(\frac{\partial^4 F_1}{\partial x^2\partial \psi^2} - 2\frac{\partial^3 F_1}{\partial x\partial \psi^2} + \frac{\partial^2 F_1}{\partial \psi^2}\right),\\
T_{12}(W) = {} & -A_3\left(\frac{\partial^4 W}{\partial x^4} - 4\frac{\partial^3 W}{\partial x^3} + 4\frac{\partial^2 W}{\partial x^2} + 2\frac{\partial^2 W}{\partial \psi^2} + \frac{\partial^4 W}{\partial \psi^4}\right)\\
& - 2(A_4 + A_6)(\frac{\partial^4 W}{\partial x^2\partial \psi^2} - 2\frac{\partial^3 W}{\partial x\partial \psi^2} + \frac{\partial^2 W}{\partial \psi^2})\\
& - s_1^4 e^{4x} k_{\mathrm{w}} W + s_1^2 e^{2x} k_{\mathrm{p}}\left(\frac{\partial^2 W}{\partial x^2} + \frac{\partial^2 W}{\partial \psi^2}\right),\\
T_{13}(W) = {} & -\frac{1}{2}s_1^3 e^{3x}\tan\gamma\left(-\frac{\partial W}{\partial x} + \frac{\partial^2 W}{\partial x^2}\right) - s_1^3 e^{3x}\tan\gamma\frac{\partial^2 W}{\partial \psi^2} - s_1^3 e^{3x}\tan\gamma\frac{\partial W}{\partial x},\\
T_{14}(W) = {} & -\frac{1}{2}s_1 s_2^2 e^{x}\tan\gamma\left(-\frac{\partial W}{\partial x} + \frac{\partial^2 W}{\partial x^2}\right),\\
T_{21}(F_1) = {} & B_1 e^{2x}\left(\frac{\partial^4 F_1}{\partial x^4} - 4\frac{\partial^3 F_1}{\partial x^3} + 4\frac{\partial^2 F_1}{\partial x^2} + 2\frac{\partial^2 F_1}{\partial \psi^2} + \frac{\partial^4 F_1}{\partial \psi^4}\right)\\
& + 2(B_2 + B_5)e^{4x}\left(\frac{\partial^4 F_1}{\partial x^2\partial \psi^2} + 2\frac{\partial^3 F_1}{\partial x\partial \psi^2} + \frac{\partial^2 F_1}{\partial \psi^2}\right),\\
T_{22}(W) = {} & -B_4 e^{-4x}\left(\frac{\partial^4 W}{\partial x^4} - 4\frac{\partial^3 W}{\partial x^3} + 4\frac{\partial^2 W}{\partial x^2} + 2\frac{\partial^2 W}{\partial \psi^2} + \frac{\partial^4 W}{\partial \psi^4}\right)\\
& + 2(B_6 - B_3)\left(\frac{\partial^4 W}{\partial x^2\partial \psi^2} - 2\frac{\partial^3 W}{\partial x\partial \psi^2} + \frac{\partial^2 W}{\partial \psi^2}\right) + s_1 e^{x}\cot\gamma\left(\frac{\partial^2 W}{\partial x^2} - \frac{\partial W}{\partial x}\right),
\end{aligned}
\tag{A.1}
$$

where coefficients A_i and B_i are defined by

$$
\begin{aligned}
& A_1 = c_{11}B_1 + c_{12}B_2, && A_2 = c_{11}B_2 + c_{21}B_1,\\
& A_3 = c_{11}B_3 + c_{21}B_4 + c_{12}, && A_4 = c_{11}B_4 + c_{21}B_3 + c_{22},\\
& A_5 = c_{61}B_5, && A_6 = c_{61}B_6 + c_{62},\\
& B_1 = c_{10}D, && B_2 = -c_{20}D,\\
& B_3 = (c_{20}c_{21} - c_{11}c_{10})D, && B_4 = (c_{20}c_{11} - c_{21}c_{10})D,\\
& B_5 = 1/c_{60}, && B_6 = c_{61}/c_{60},\\
& D = 1/(c_{10}c_{10} - c_{20}c_{20}).
\end{aligned}
\tag{A.2}
$$

In Appendix (A.2), coefficients c_{ik} are defined as follows:

$$c_{1k} = \int_{-0.5h}^{0.5h} z^k \frac{E(z)}{1-\nu^2(z)} dz, \qquad c_{2k} = \int_{-0.5h}^{0.5h} z^k \frac{\nu(z)E(z)}{1-\nu^2(z)} dz,$$
$$c_{6k} = \int_{-0.5h}^{0.5h} z^k \frac{E(z)}{2(1+\nu(z))} dz. \tag{A.3}$$

Acknowledgments

The present research is funded by the financial support of the Natural Science Foundation of Guangxi (grant no. 2025GXNSFAA069217) and (grant no. 2021GXNSFAA220087) and the National Natural Science Foundation of China (grant no. 12162010). The authors are grateful for their support.

References

1. Ali, A.Y., & Hasan, H.M. (2019). Nonlinear dynamic stability of an imperfect shear deformable orthotropic functionally graded material toroidal shell segments under the longitudinal constant velocity. *Proceedings of the Institution of Mechanical Engineers, Part C: Journal of Mechanical Engineering Science*, *233*(19–20), 6827–6850. https://doi.org/10.1177/0954406219867991
2. Allahkarami, F., Saryazdi, M.G., & Tohidi, H. (2020). Dynamic buckling analysis of bi-directional functionally graded porous truncated conical shell with different boundary conditions. *Composite Structures*, *252*, Article 112680. https://doi.org/10.1016/j.compstruct.2020.112680
3. Bich, D.H., & Ninh, D.G. (2016). Post-buckling of sigmoid-functionally graded material toroidal shell segment surrounded by an elastic foundation under thermo-mechanical loads. *Composite Structures*, *138*, 253–263. https://doi.org/10.1016/j.compstruct.2015.11.044
4. Chi, S.-H., & Chung, Y.-L. (2006). Mechanical behavior of functionally graded material plates under transverse load—Part I: Analysis. *International Journal of Solids and Structures*, *43*(13), 3657–3674. https://doi.org/10.1016/j.ijsolstr.2005.04.011
5. Duc, N.D., & Cong, P.H. (2015). Nonlinear dynamic response of imperfect symmetric thin sigmoid-functionally graded material plate with metal-ceramic-metal layers on elastic foundation. *Journal of Vibration and Control*, *21*(4), 637–646. https://doi.org/10.1177/1077546313489717
6. Duc, N.D., Kim, S.E., & Chan, D.Q. (2018). Thermal buckling analysis of FGM sandwich truncated conical shells reinforced by FGM stiffeners resting on elastic foundations using FSDT. *Journal of Thermal Stresses*, *41*(3), 331–365. https://doi.org/10.1080/01495739.2017.1398623
7. Fan, L.J., Sahmani, S., & Safaei, B. (2021). Couple stress-based dynamic stability analysis of functionally graded composite truncated conical microshells with magnetostrictive facesheets embedded within nonlinear viscoelastic foundations. *Engineering with Computers*, *37*(2), 1635–1655. https://doi.org/10.1007/s00366-020-01182-w
8. Foroutan, K., & Torabi, F. (2026). Nonlinear chaotic and periodic responses of obliquely stiffened sigmoid FG cylindrical shells under principal torsional parametric, subharmonic, and 1:2 internal resonances. *Thin-Walled Structures*, *221*, Article 114463. https://doi.org/10.1016/j.tws.2025.114463
9. Fu, T., Wu, X., Xiao, Z., & Chen, Z. (2021). Dynamic instability analysis of porous FGM conical shells subjected to parametric excitation in thermal environment within FSDT. *Thin-Walled Structures*, *158*, Article 107202. https://doi.org/10.1016/j.tws.2020.107202
10. Hoa, L.K., Phi, B.G., Chan, D.Q., & Hieu, D.V. (2022). Buckling analysis of FG porous truncated conical shells resting on elastic foundations in the framework of the shear deformation theory. *Advances in Applied Mathematics and Mechanics*, *14*(1), 218–247. https://doi.org/10.4208/aamm.OA-2020-0202

11. Mallek, H., Mellouli, H., Ben Said, L., Wali, M., Dammak, F., & Alhadri, M. (2025). Porosity effects on nonlinear static performances of functionally graded shells considering thickness stretching. *Facta Universitatis, Series: Mechanical Engineering*, *23*(4), 827–860. https://doi.org/10.22190/FUME240920015M

12. Naj, R., Sabzikar Boroujerdy, M., & Eslami, M.R. (2008). Thermal and mechanical instability of functionally graded truncated conical shells. *Thin-Walled Structures*, *46*(1), 65–78. https://doi.org/10.1016/j.tws.2007.07.011

13. Nemati, A.R., & Mahmoodabadi, M.J. (2020). Effect of micromechanical models on stability of functionally graded conical panels resting on Winkler–Pasternak foundation in various thermal environments. *Archive of Applied Mechanics*, *90*(5), 883–915. https://doi.org/10.1007/s00419-019-01646-6

14. Ng, T.Y., Lam, K.Y., Liew, K.M., & Reddy, J.N. (2001). Dynamic stability analysis of functionally graded cylindrical shells under periodic axial loading. *International Journal of Solids and Structures*, *38*(8), 1295–1309. https://doi.org/10.1016/S0020-7683(00)00090-1

15. Pal, S., Rout, M., Deb Singha, T., & Karmakar, A. (2025). Thermoelastic free vibration of rotating pretwisted porous p-FGM, e-FGM, and s-FGM conical shells in nonlinear temperature distribution. *Journal of Vibration and Control*, *31*(7–8), 1258–1277. https://doi.org/10.1177/10775463241240625

16. Sofiyev, A.H. (2009). The vibration and stability behavior of freely supported FGM conical shells subjected to external pressure. *Composite Structures*, *89*(3), 356–366. https://doi.org/10.1016/j.compstruct.2008.08.010

17. Sofiyev, A.H. (2010). The buckling of FGM truncated conical shells subjected to combined axial tension and hydrostatic pressure. *Composite Structures*, *92*(2), 488–498. https://doi.org/10.1016/j.compstruct.2009.08.033

18. Sofiyev, A.H. (2016). Parametric vibration of FGM conical shells under periodic lateral pressure within the shear deformation theory. *Composites Part B: Engineering*, *89*, 282–294. https://doi.org/10.1016/j.compositesb.2015.11.017

19. Sofiyev, A.H., Alizada, A.N., Akin, Ö., Valiyev, A., Avcar, M., & Adiguzel, S. (2012). On the stability of FGM shells subjected to combined loads with different edge conditions and resting on elastic foundations. *Acta Mechanica*, *223*(1), 189–204. https://doi.org/10.1007/s00707-011-0548-1

20. Sofiyev, A.H., & Schnack, E. (2012). The vibration analysis of FGM truncated conical shells resting on two-parameter elastic foundations. *Mechanics of Advanced Materials and Structures*, *19*(4), 241–249. https://doi.org/10.1080/15376494.2011.642934

21. Wu, H., Yang, J., & Kitipornchai, S. (2020). Mechanical analysis of functionally graded porous structures: A review. *International Journal of Structural Stability and Dynamics*, *20*(13), Article 2041015. https://doi.org/10.1142/S0219455420410151

22. Yuan, Y., Zhao, X., Zhao, Y., Sahmani, S., & Safaei, B. (2021). Dynamic stability of nonlocal strain gradient FGM truncated conical microshells integrated with magnetostrictive facesheets resting on a nonlinear viscoelastic foundation. *Thin-Walled Structures*, *159*, Article 107249. https://doi.org/10.1016/j.tws.2020.107249

23. Zhang, J., & Li, S. (2010). Dynamic buckling of FGM truncated conical shells subjected to non-uniform normal impact load. *Composite Structures*, *92*(12), 2979–2983. https://doi.org/10.1016/j.compstruct.2010.05.009

24. Zhu, J., Lai, Z., Yin, Z., Jeon, J., & Lee, S. (2001). Fabrication of ZrO_2–NiCr functionally graded material by powder metallurgy. *Materials Chemistry and Physics*, *68*(1–3), 130–135. https://doi.org/10.1016/S0254-0584(00)00355-2

Manuscript received November 5, 2025; accepted for publication June 13, 2026;

Contents

Shen C., Zhao S., Tan K., Li L., Li F., Wang T., *Research on the penetration resistance performance of a ceramic ball/nylon elastomer composite structure* 101

Yousfi N., Maktouf R., Akrout A., Walha L., Haddar M., *Nonlinear damping identification using an extended stabilized layers method* 115

Brykczyński M.B., Harlecki A., *Driving torque for a steer-by-wire system hand wheel actuator based on the reference driving torque from an electric power steering system* 131

Naebi M.S., Raeisifard H., Mohammadi N., *An adaptive semi-empirical framework for rolling resistance prediction incorporating tire mass and dynamic geometric parameters* 145

Huang X.-l., Liu H., Han Y., Wei Y., Wu W., *Dynamic instability analysis of porous sigmoid functionally graded truncated conical shells subjected to combined pressures* 165